

VERIFICATION OF RECOIL SEPARATOR PROPERTIES THROUGH DIRECT  
REACTION MEASUREMENTS

A Dissertation

Submitted to the Graduate School  
of the University of Notre Dame  
in Partial Fulfillment of the Requirements  
for the Degree of

Doctor of Philosophy

by  
Michael Thaddeus Moran

---

Manoël Couder, Co-Director

---

Michael C. F. Wiescher, Co-Director

Graduate Program in Physics

Notre Dame, Indiana

November 2018

# VERIFICATION OF RECOIL SEPARATOR PROPERTIES THROUGH DIRECT REACTION MEASUREMENTS

Abstract

by

Michael Thaddeus Moran

The St. George recoil separator is designed to measure  $(\alpha, \gamma)$  cross sections of astrophysical interest in inverse kinematics. The design of the separator allows for a large energy ( $\pm 7.5\% \Delta E/E$ ) and angular ( $\pm 40$  mrad) acceptance that must be verified across a wide range of electric and magnetic rigidities before primary experimental work can begin. The beam rejection properties of the separator system must be determined to ensure that the direct incident beam is adequately rejected such that the produced recoils can be confidently measured. The procedures used during the commissioning work to experimentally verify these properties will be discussed.

Utilization of the separator for measuring cross sections of astrophysical interest that were not considered during the design phase is an additional benefit of the commissioning work and expands the potential domain of study for the separator. The first such experiment to measure two strong resonances in the  $^{27}\text{Al}(\text{p}, \alpha)^{24}\text{Mg}$  cross section has been completed. This reaction study is additionally a test of the separator's energy and angular acceptances *in situ* as a precursor to studying  $(\alpha, \gamma)$  reactions. The results of this measurement in relation to the properties of St. George will be discussed. An analysis package and pipeline were developed to support the study of the reaction in question and any future experiments using St. George.

To Link, the fluff monster that can both frustrate and calm me

To Laura, the woman who can do anything

## CONTENTS

FIGURES . . . . .	vi
TABLES . . . . .	vii
ACKNOWLEDGMENTS . . . . .	viii
CHAPTER 1: INTRODUCTION . . . . .	1
1.1 Stellar Burning . . . . .	2
1.1.1 Low-Mass Hydrogen Burning . . . . .	2
1.1.2 Helium Burning . . . . .	5
1.1.3 Additional Burning Processes . . . . .	6
1.2 Capture Reactions . . . . .	7
1.2.1 Cross Section and <i>S</i> -factor . . . . .	8
1.2.2 Reaction Rate . . . . .	10
1.2.3 Resonances . . . . .	11
1.2.4 Angular Properties . . . . .	13
1.3 Recoil Separation . . . . .	15
1.3.1 Motivation . . . . .	15
1.3.1.1 Inverse Kinematics . . . . .	16
1.3.1.2 Radiative Capture . . . . .	18
1.3.2 Beam Optics . . . . .	19
1.3.2.1 Mass Dispersion . . . . .	20
1.3.2.2 Beam Suppression . . . . .	21
1.3.3 Recoil Separator Facilities . . . . .	22
1.3.3.1 CalTech Separator . . . . .	23
1.3.3.2 ARES . . . . .	24
1.3.3.3 DRAGON . . . . .	24
1.3.3.4 ERNA . . . . .	25
1.3.3.5 DRS . . . . .	25
1.3.3.6 St. George . . . . .	26
1.3.4 Requirements . . . . .	26

CHAPTER 2: EXPERIMENTAL SETUP . . . . .	28
2.1 The St. Ana Accelerator and Transport Line . . . . .	28
2.2 The St. George Recoil Separator . . . . .	31
2.2.1 Subsections of St. George . . . . .	32
2.2.2 Diagnostic Equipment . . . . .	35
2.3 Detector System and Data Acquisition . . . . .	37
2.4 Target Chamber . . . . .	38
CHAPTER 3: COMMISSIONING ST. GEORGE . . . . .	41
3.1 Theoretical and Experimental Considerations . . . . .	43
3.2 Separator Properties . . . . .	47
3.2.1 Magnetic Fringe Fields and Effective Field Lengths . . . . .	48
3.3 Energy and Angular Acceptance . . . . .	53
3.3.1 Beam Tuning and Properties . . . . .	54
3.3.1.1 Before St. George . . . . .	55
3.3.1.2 Within St. George . . . . .	61
3.3.1.3 Collimator and Target Position . . . . .	64
3.3.1.4 Additional Considerations . . . . .	64
3.3.2 Energy Acceptance . . . . .	65
3.3.3 Angular Acceptance . . . . .	68
3.4 Considerations . . . . .	71
CHAPTER 4: EXPERIMENTAL PROCEDURE . . . . .	73
4.1 Altered Tune . . . . .	74
4.1.1 Separator Properties . . . . .	75
4.1.2 Beam Reduction . . . . .	77
4.2 Run Procedure . . . . .	78
4.2.1 Beam Preparation . . . . .	78
4.2.2 Measuring Beam Suppression . . . . .	80
4.2.3 Target Effects . . . . .	81
4.2.4 Final Optimization . . . . .	81
4.2.5 Experimental Run . . . . .	83
CHAPTER 5: ANALYSIS . . . . .	87
5.1 Target Properties . . . . .	88
5.2 Beam Properties . . . . .	89
5.3 Detector Properties . . . . .	90
5.3.1 Simulating the Energy Spectrum . . . . .	90
5.4 Additional Parameters . . . . .	92
5.5 Final Acceptance Measurements . . . . .	94

CHAPTER 6: DISCUSSION . . . . .	97
6.1 Acceptance . . . . .	97
6.2 Advantages and Disadvantages . . . . .	104
6.3 Uncertainties . . . . .	104
6.3.1 Statistical . . . . .	105
6.3.1.1 Target Thickness . . . . .	105
6.3.1.2 Beam Energy . . . . .	106
6.3.1.3 Beam Current . . . . .	106
6.3.1.4 Time . . . . .	108
6.3.1.5 Detector Counts . . . . .	108
6.3.1.6 SRIM Tabulated Values . . . . .	108
6.3.1.7 Final Bands . . . . .	109
6.3.2 Systematic . . . . .	110
6.3.2.1 Analytical Sources . . . . .	111
6.3.2.2 Experimental Sources . . . . .	111
6.4 Uniformity of Acceptances . . . . .	113
6.5 Charge State Distribution . . . . .	114
6.6 The $(p, \alpha_1)$ Channel . . . . .	115
CHAPTER 7: CONCLUSIONS . . . . .	117
7.1 Next Steps . . . . .	118
7.2 Closing Thoughts . . . . .	119
APPENDIX A: RUN INFORMATION . . . . .	122
APPENDIX B: ALPHA CALIBRATION ENERGIES . . . . .	124
APPENDIX C: DEFLECTOR SETTINGS . . . . .	126
APPENDIX D: FRINGE FIELD PARAMETERS . . . . .	128
APPENDIX E: ANALYSIS PACKAGE . . . . .	129
E.1 Python for Nuclear Experiments . . . . .	130
E.2 St. George Analysis Package . . . . .	131
E.3 Justification . . . . .	131
BIBLIOGRAPHY . . . . .	134

## FIGURES

1.1	Schematic of burning cycles . . . . .	4
1.2	Cross section for the $^{27}\text{Al}(\text{p}, \alpha)^{24}\text{Mg}$ reaction . . . . .	9
1.3	Energy diagram for the $^{27}\text{Al}(\text{p}, \alpha)^{24}\text{Mg}$ reaction . . . . .	12
2.1	Schematic of the 5U accelerator . . . . .	29
2.2	Layout of the St. George recoil separator . . . . .	31
2.3	Schematic of the St. George Wien filter . . . . .	34
2.4	Locations of diagnostic equipment . . . . .	36
3.1	Horizontal and vertical rays through St. George . . . . .	44
3.2	Normalized field with Enge fit . . . . .	50
3.3	Comparison between fringe fields . . . . .	52
3.4	Designed $B\rho - E\rho$ rigidity phase space for St. George . . . . .	54
3.5	Sketch of beam divergence due to focusing strength . . . . .	56
3.6	Sketch of quadrupole steering of misaligned beam . . . . .	59
4.1	Horizontal and vertical rays through St. George for $\alpha$ particles . . . . .	79
4.2	Horizontal $\alpha$ particle distribution . . . . .	85
4.3	Detector positions . . . . .	86
5.1	Simulated detector $\alpha$ energy spectrum . . . . .	93
6.1	Final acceptances . . . . .	98
6.2	Example cross section . . . . .	100

## TABLES

1.1	RESONANCE PARAMETERS . . . . .	14
4.1	POLE TIP FIELDS FOR $(\alpha, \gamma)$ AND $(p, \alpha)$ STUDIES . . . . .	75
6.1	ACCEPTANCE WITH UNCERTAINTY . . . . .	99
6.2	ACCEPTANCE BOUNDS WITH HELD VARIABLES, 67 % . . . . .	102
6.3	ACCEPTANCE BOUNDS WITH HELD VARIABLES, 95 % . . . . .	103
6.4	BEAM CURRENT UNCERTAINTY . . . . .	107
6.5	RUN TIME UNCERTAINTY . . . . .	109
6.6	KINEMATICS FOR $(p, \alpha_1)$ . . . . .	115
A.1	RUN ENERGY DETAILS . . . . .	123
B.1	ALPHA PARTICLE ENERGIES FOR THE $^{241}\text{Am}/^{148}\text{Gd}$ MIXED SOURCE . . . . .	125
C.1	DEFLECTOR SETTINGS FOR TEST BEAMS . . . . .	127
D.1	ENGE COEFFICIENTS FOR $Q_{10}$ COMPARED TO COSY DEFAULTS	128

## ACKNOWLEDGMENTS

I would like to thank my advisors, Manoel Couder and Michael Wiescher, for helping me as I explored and discovered my path in science and in life. The major achievements in my graduate career would not have been possible without their guidance each day and their understanding as I struggled through the low points in my journey. I would also like to thank the remainder of my committee, Drs. Daniel Bardayan, Mark Caprio, and John LoSecco, for guiding me through the candidacy and defense process, and being understanding with my completion-from afar and the scheduling madness that entailed.

The entirety of this project would be impossible without the excellent support I had throughout the Nuclear Science Lab and the Department of Physics. In particular, Daniel Robertson and Edward Stech were invaluable for learning standard operating procedures throughout the lab, especially with the accelerators, targets, and detector systems, and how to be a graduate student within the NSL. Thank you to Jerry Schur for helping me with every network problem that I happened to forget the solution to at precisely the wrong time. Thank you to the amazing work done both within and without the machine shop from Dave Futa, Jerry Lingle, Bradley Mulder, and Matt Sanford. There have been more times than I could count where this project would not have moved forward without you. Thank you to the excellent support from Susan Baxmeyer and Shari Herman, who never failed to cheer me up when I saw them in the office and who helped me navigate through the parts of graduate school life that I had no idea of what to do otherwise. Thank you to Janet Weikel for helping me in countless ways and always being a happy face as I entered

and left the NSL.

Thank you to the greater St. George group, past and present— Manoel Couder, Jerry Hinnefeld, Zach Meisel, Gwen Gilardy, Patricia Huestis, Edward Lamere, Luis Morales, Shane Moylan, and Chris Seymour—for being the support for when tuning went poorly and the source of jubilation when things went well. To those future graduate students and postdocs within the group, I thank you for taking this project on your own shoulders, and I hope this is a decent starting point for your own work.

Thank you to Will Bauder, Stephanie Lyons Blyth, Matt Bowers, Hyu Soon Jung, Wenting Liu, Alex Long, Karen Ostdiek, Karl Smith, Kiana Setoodhar, and Ethan Uberseder, my former group mates, co-graduate students, office mates, and guiding older scientists, for helping me as I struggled to figure out who I was as a scientist and for helping me when the work of physics became too much. Thank you to the other graduate students and postdocs within the NSL and the Department of Physics who, one way or another, not only helped make my time in graduate school bearable but also enjoyable. Your names are far too numerous to list here.

Thank you to Christina Marentette, my high school physics teacher and one of the largest influences on my life trajectory. I would not be where I am now without your guidance and example. Thank you to my crew members on the Mars Desert Research Station rotation 89—Brian Shiro, Carla Haroz, Darrel Robertson, Luis Saraiva, and Kiri Wagstaff—for being such good examples of what I could be when I “grew up”. A special thank you to Kiri, for reintroducing me to python and setting me on my course to my life beyond physics.

Thank you to the people I met through curling, both local and remote, that gave me an outlet that turned into what will be a life-long passion. Thank you especially to the founding South Bend Regional Curling Club members—skip Dean Palmer, second Jared Coughlin, lead Blair Vandenburg, and alternate Ralph Lantz—who were an amazing happenstance at the end of my time in South Bend. Competing in

a national championship is something that I will never forget.

Thank you to the friends I've made in that strange interim between leaving graduate school and finishing graduate school: the fellows and mentors at the Insight Data Science program, my co-workers and teammates at Gartner, and the additional people I've met during my time in NYC. Having an additional cohort of people interested in my progress helped keep that progress from stalling, and being understanding of the time and effort required without creating an undue burden was more help than they'll ever know.

To those close friends that I've made in graduate school, thank you for everything. You've each impacted my life in so many different ways that listing everything out would triple the length of this dissertation. You are better than I could have imagined as the people going through this process with me.

Thank you to my friends from Michigan State: Nichole Hoerner, Gregory Klein, and Ashleigh Winkelmann. Our continued friendship over the years has made me realize how lucky I am to have stumbled into your lives.

Thank you to Pokie and Mike Olsen for allowing a young graduate student into your home and for reawakening my love of board games. I can barely remember a time before I had to struggle to pay for a 6-cost development, and I didn't fully appreciate how amazing it was until you left. Thank you to Michael Planer for being one of my first friends and teaching me the wonders of having a whole bunch of extra T-shirts around. Thank you to Will Bauder (and his wife, Laura) for introducing me to so many things and showing me first-hand that you can become happy after leaving graduate school. Thank you to Charlie Mueller for being an amazing friend and a hilarious companion, everywhere between Red River Gorge to that stretch of Cleveland Road. Thank you to Chris Wotta for always being up for talking at length about programming and for bonding over our mutual Michigan-ness. Thank you again to Jared Coughlin for thinking that I'd be interested in being on his curling

team and for being a climbing buddy. Thank you to Joseph Hagmann for being that guiding light that directly and indirectly helped me and my wife through some of the best and worst times of our time in South Bend. We could not have done this without you. Thank you to Kate Rueff for helping me survive graduate school in more ways than one. You—and of course, your dog Maxwell—have done so much for me, and I don't think I could ever come close to repaying you. Thank you MacKenzie Warren for being the sounding board of my thoughts and feelings from our time together as roommates through the present day. You've shown me that people can survive graduate school and come out better from it.

Thank you to Clark and Jacee Casarella and Alicia and Edward Lamere for being our best friends. There's honestly no way to split the four of you up in these acknowledgements, nor would I want to. I could not imagine my time in graduate school without any of you. There are too many memories, joyous and bitter-sweet and wonderful, and too many emotions involved with writing this. Though the distance may physically separate us as we are, scattered across states and time zones, there's nothing that could keep us apart. Just simply, thank you for everything.

My family has been a huge party of who am I today. I am lucky to have been surrounded by amazing people growing up: my siblings Caitlin, Colleen, and Patrick; my cousins Brandon, Christopher, Lindsey, Meredith, Billy, Missy, Sage, Katie, Kristen, and Kelly; my aunts and uncles Michelle, Angelo, Reneé, Debbie, Buddy, Kathie, Chris, Trish, and Teddy; and my grandparents Francis, Thaddeus, Theresa, and William. I am also extremely fortunate to have had my family grown during my time in grad school: my cousin Grace; my sister-in-law Hannah; and my brother-in-law Peter with his wife Jane and their kids Coulter and Eloise; and my entire new extended-extended families. I'd especially like to thank my parents-in-law Katie and Bruno for welcoming me into their home and their lives early in my graduate career. Your additional support helped in both the good times and bad, and having a second

set of loving and caring parents helped in more ways than I can say. I want to thank my parents, Brigitte and Mike, for raising me to question the world around me and never be comfortable with where I was. You supported me while I tinkered with Legos in the basement, through my academic and athletic pursuits, and were always available to help me through my years in graduate school. More than anything, I could not have imagined attempting this had it not been for your nurturing and support all of the years of my life.

Thank you to Link for being both a hassle and a joy at the end of my graduate career. You reawakened my love of Chicken McNuggets, kept me (too) warm while I lay on the couch or in bed, annoyed me as you scarfed down discarded chicken wings, worried me as you went to and from the vet, comforted me when I was sad, and relished in my joy with me. You are the goodest boy.

Finally, I would like to thank my wife, Laura Amelia. There is a deep feeling of happiness that I never felt before that you have brought into my life, that you continue to bring into my life every single day. From the first day I met you to me writing these very words, there is not a moment spent with you that I would want to change. Everything that we have done together—the trips to the Grand Teton National Park; the move to NYC; getting a dog; making the long-haul drives criss-crossing the country; surprising me with a trip to Cedar Pointe; consoling and driving me to Detroit at the lowest point of my time in grad school; helping me when I was down; smiling when I was up; caring for me and loving me through everything—absolutely everything that has happened in our lives together is a memory that I would not want to lose, because those memories are with you. While this segment of our lives together is now over, our journey together through this wondrous world is only just beginning. I love you with all of my being and everything that I have to offer to you. I love you so much, Laura. Thank you.

## CHAPTER 1

### INTRODUCTION

The elements making up the universe were formed during a variety of processes, beginning with Big Bang Nucleosynthesis (BBN) that formed the lightest elements. Those elements common to life on Earth were primarily formed through burning processes inside of stars, grouped together under the title of stellar nucleosynthesis. Depending on the conditions within the stellar environment, which are characterized by macroscopic qualities about the star (temperature, pressure, mass, etc.) and the elemental composition of the stellar interior where the burning process takes place, the reactions accessible to the nuclei within the star differ. The creation and destruction of different elements and isotopes may be inhibited or enhanced by these differing conditions, and the study of these processes at the nuclear level has spawned the field of *nuclear astrophysics* in order to understand the inner workings of these stars. Nuclear astrophysics can be described as the specific and directed study of those nuclear reactions that have an effect on the properties or life cycle of celestial bodies. These reactions may take place during the life cycle of a star, during a cataclysmic event within the universe such as a black hole merger or gamma ray burst, or at the beginning of the universe itself. Additionally, the decay of various isotopes can also play a major role within this domain, either as part of a sequence of reactions or independently. The entire field of nuclear astrophysics was conceived in the seminal papers [10] and [11], which have been used as a basis for much of the work in the following decades.

For astrophysical reactions, the properties of the environment can play a major

role in how quickly the reaction proceeds or if it is even energetically allowed. Cross sections for reactions involving charged particles rapidly decrease at lower energies, requiring increasingly sophisticated methods to characterize the energy dependence of the cross section. Due to the rapidly decreasing cross sections at low energies, work has typically focused on strong resonances in this low-energy regime.

## 1.1 Stellar Burning

Stars in hydrostatic equilibrium can produce energy through a number of different reaction channels based on the mass, temperature, and isotopic enrichment of the stellar interior where the burning process takes place. The net result of stellar burning is the fusion of lighter isotopes into heavier isotopes and the release of energy. A single star may undergo multiple distinct burning stages during its lifecycle, with each subsequent burning stage occurring at progressively hotter temperatures until a point at which the energy produced cannot maintain hydrostatic equilibrium.

The isotopic abundances in the stellar interior at a given point in time are based on the initial abundances within the interstellar medium when the cloud condensed into the star, and the reaction channels that are available in the stellar interior during the lifespan of the star.

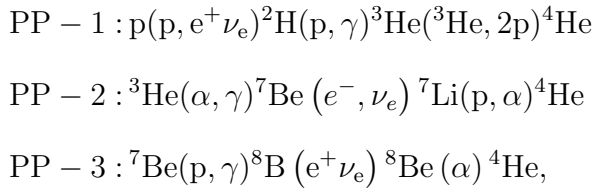
### 1.1.1 Low-Mass Hydrogen Burning

The fusion of four  $^1\text{H}$  nuclei into a single  $^4\text{He}$  nucleus is called *hydrogen burning*, and can take place through a few reaction sequences within different temperature ranges. The overall outcome of the reaction chain given by



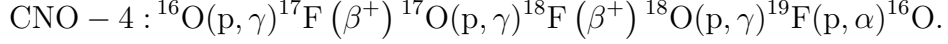
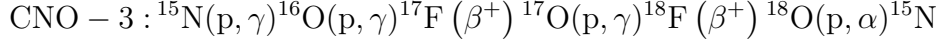
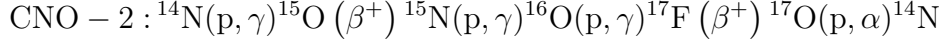
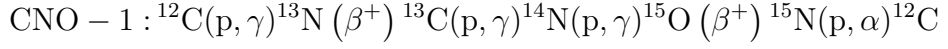
is the conversion of  $^1\text{H}$  into  $^4\text{He}$  and the release of approximately 26.7 MeV in energy from that fusion. The underlying reaction processes within stars under steady state conditions are grouped under *hydrostatic hydrogen burning*. Common environments for such burning processes are core hydrogen burning in stars similar to our sun in mass and metallicity, and in hydrogen burning shells within asymptotic giant branch (AGB) stars. The differences in the isotopic composition and temperature of the stellar interior can allow for different processes to take place.

Stars similar to our sun fuse hydrogen through the proton-proton (*pp*) chains, which are described by the reaction sequences



where the PP-2 and PP-3 chains are branches off from the PP-1 and PP-2 chains, respectively, at the point after the initial nuclei is created within the chain. Typical temperatures for this burning process are on the order of  $T_6 \approx 8 - 55$ , which the core temperature of our sun ( $T_6 = 15.6$ ) falls squarely within [22].

The Carbon-Nitrogen-Oxygen (CNO) cycle is an additional pathway for stable hydrogen burning accessible when the stellar interior has been enriched with heavier nuclei. The relative abundances of the catalytic elements C, N, O, and F will change based on the relative reaction rates. The CNO cycles are described by the cyclic reaction sequences



A schematic of these cycles can be seen on the left side of Fig. 1.1.

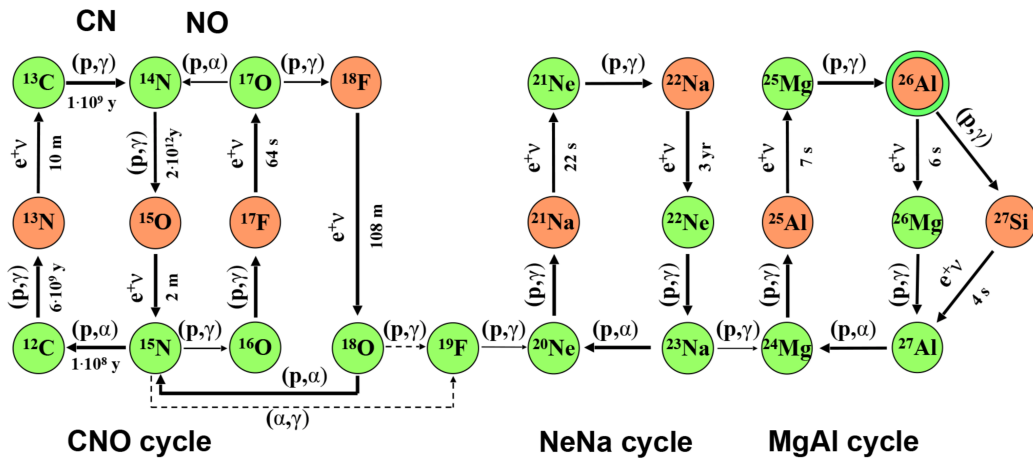


Figure 1.1. Schematic of hydrogen burning cycles in the  $12 \leq A \leq 27$  mass range, including the CNO cycle. These catalytic cycles play a large role in various abundance measurements and burning processes in red giant stars.

The reaction in question is indicated. Figure adapted from [8].

For the CNO cycles, the temperature of the interior of the star and the individual reaction rates in question determine which cycle dominates as well as which catalytic isotope will, in steady state conditions, have the highest fractional abundance. These

differing abundances based on the properties of the star can have large consequences on the burning phases at higher mass and temperature due to the isotopic enrichment available.

As the burning progresses, an inert core primarily consisting of  $^4\text{He}$  is produced. Due to the lower temperatures in the core at this stage in stellar evolution, no He burning takes place. This inert core may ignite during the red giant stage of stellar evolution, at which point the He within the outer shell of this inert core ignites and helium burning becomes an open channel for stellar energy production.

### 1.1.2 Helium Burning

The primary nucleosynthesis products of helium burning are  $^{12}\text{C}$  and  $^{16}\text{O}$ , produced through the *triple- $\alpha$  process* given by  $^4\text{He}(\alpha\alpha, \gamma)^{12}\text{C}$  and  $^{12}\text{C}(\alpha, \gamma)^{16}\text{O}$ , respectively [1]. The relative abundance ratio C/O between these two isotopes greatly affects the subsequent evolution of the star at the end of the He burning phase. He burning progresses first through the triple- $\alpha$  process until such a time that enough  $^{12}\text{C}$  has built up within the He core, at which point the production of  $^{16}\text{O}$  can begin [1].

He burning may take place in varied stellar environments. Following the end of H burning within main sequence stars, the stellar interior compresses since not enough energy is being produced. This compression increases the pressure and temperature near the stellar core to the point that He burning becomes energetically favorable [12]. The star expands, transitioning from a main sequence star to a red giant star, and maintains hydrostatic equilibrium due to the increased outward pressure produced by He burning.

Asymptotic Giant Branch (AGB) stars are a phase of stellar evolution following the turnoff from the main sequence after initial H burning completes [12]. The stellar interior contains two distinct burning regions: H and He. These regions alternate in which is active as the reaction sequences progress within each region [1]. During the

early AGB phase, the H burning shell is nearly inert until the point when mixing occurs between the H- and He-rich regions near the center of the star [12]. The star then enters the thermal pulse AGB phase, defined by a reactivated H burning region and periodic He shell flashes caused by the rapid introduction of He from the H burning shell onto the top layer of the He burning shell. The flash drives the H burning shell outward, cooling it and reducing the burning rate, which in turn ends the shell flash. As the He burning subsides, the H burning shell can reactivate, restarting the cycle [12]. Temperatures required for this cyclic process are in the  $T_6 = 20 - 60$  temperature range, where temperatures at the higher end create a more-efficient environment for the CNO reactions [8].

During these shell flashes, additional He burning reactions activate. Two such reactions,  $^{13}\text{C}(\alpha, \text{n})^{16}\text{O}$  and  $^{22}\text{Ne}(\alpha, \text{n})^{25}\text{Mg}$ , are the neutron sources for the strong and weak *s*-process, respectively [1]. The strong *s*-process is responsible for approximately half of the cosmic abundances for isotopes with mass  $A \geq 90$ , while the weak *s*-process contributes to the isotopic abundances for isotopes with mass within the range  $60 \leq A \leq 90$  [1].

### 1.1.3 Additional Burning Processes

While the previously-discussed reaction sequences play a large role in the energy production of stars, additional burning sequences are available for more massive and hotter stars. These burning cycles can be thought of in similar terms to the CNO cycles, where baseline processes convert  $4^1\text{H} \rightarrow 4^4\text{He}$  and additional reactions provide a “breakout” channel to higher burning processes. The reaction  $^{27}\text{Al}(\text{p}, \alpha)^{24}\text{Mg}$  is the final step in the MgAl burning cycle (shown in Figure 1.1) that provides for the cycling of the catalytic nuclei. These burning cycles activate at elevated temperatures in the range of  $T_6 = 60 - 100$  within massive AGB stars [8].

The  $^{27}\text{Al}(\text{p}, \alpha)^{24}\text{Mg}$  reaction is relatively well-understood due to the availability

of target and beam material (see, for example, [34]). The known characteristics of the reaction across a range of center of mass energies make it a useful test reaction for new experimental facilities. The remainder of the discussion will focus on  $^{27}\text{Al}(\text{p}, \alpha)^{24}\text{Mg}$  as an example.

## 1.2 Capture Reactions

Most astrophysical reactions in the low mass regime can be considered as capture reactions, where a lighter particle with mass  $m_a$  combines or *fuses* with a heavier particle with mass  $m_A$ , forming a compound nucleus with mass  $m_C = m_a + m_A$  in an excited state. This compound nucleus will de-excite through particle emission, in the simplest case resulting in two particles  $b$  and  $B$ . The overall reaction can be written as

$$A(a, b)B,$$

where  $A$  and  $B$  denote our heavy particles and  $a$  and  $b$  denote our lighter particles. When discussing reactions, we commonly consider the lighter particle to be impinging on the heavier particle in the entrance channel  $a+A$ . The compound nucleus  $C$  is not explicitly denoted in this equation. The reaction  $^{27}\text{Al}(\text{p}, \alpha)^{24}\text{Mg}$  can be considered as this type of compound reaction, where a compound nucleus  $^{28}\text{Si}$  is created by the direct capture of the proton by  $^{27}\text{Al}$ , followed by the emission of the  $\alpha$  particle, leaving behind  $^{24}\text{Mg}$ . If the light particle  $b$  is a  $\gamma$  ray, the reaction is a *radiative capture reaction*, written as  $A(a, \gamma)B$ . Both types of reactions can be studied and understood in similar ways.

The amount of energy either released in the reaction or required for the reaction to take place is called the reaction  $Q$ -value. The  $Q$ -value is defined as the energy

difference between the entrance and exit channels, or

$$Q = (m_A + m_a - m_B - m_b)c^2,$$

where  $m_i$  is the mass of the denoted particle. Positive  $Q$ -values are exothermic reactions, where the particles produced in the exit channel carry away the excess energy, while negative  $Q$ -values are endothermic reactions, where a minimum amount of energy in the entrance channel is required in order for the reaction to take place.

For reactions that go through a compound nucleus, the energy states accessible in the reaction are based on the beam energy and the reaction  $Q$ -value. The excitation energy in the compound nucleus, as commonly expressed in nuclear experiments where the particle  $A$  is at rest, is given as

$$E_x = Q + E_{\text{CM}} = Q + E_a \frac{m_A}{m_a + m_A},$$

where  $E_{\text{CM}}$  is the center of mass energy. Unless explicitly denoted as a different energy, in the following description  $E = E_{\text{CM}}$ .

### 1.2.1 Cross Section and $S$ -factor

The probability that a reaction will occur is the reaction's *cross section*. The cross section can be defined as the ratio between the number of reactions that actually took place and the total numbers of incident target particles within some time frame, or

$$\sigma = \frac{N_{\text{reactions}}/t}{N_{\text{beam}}/t N_{\text{target}}/A},$$

where  $A$  is the overlapping area between the target and the incident beam of particles [22]. The above equation is implicitly energy dependent, as the number of reactions may change with changing beam energy. Additionally, the reaction prod-

ucts may be emitted through different solid angles at different rates. In these cases, the differential cross section  $d\sigma/d\Omega$  is measured. The differential cross section can be integrated over the complete solid angle to obtain the total cross section

$$\sigma = \int \left( \frac{d\sigma}{d\Omega} \right) d\Omega.$$

The cross section is an important quantity to constrain astrophysical reactions. The cross section for the  $^{27}\text{Al}(p, \alpha)^{24}\text{Mg}$  reaction near the energy range of interest for this experiment is shown in Fig. 1.2, where the structure will be described later.

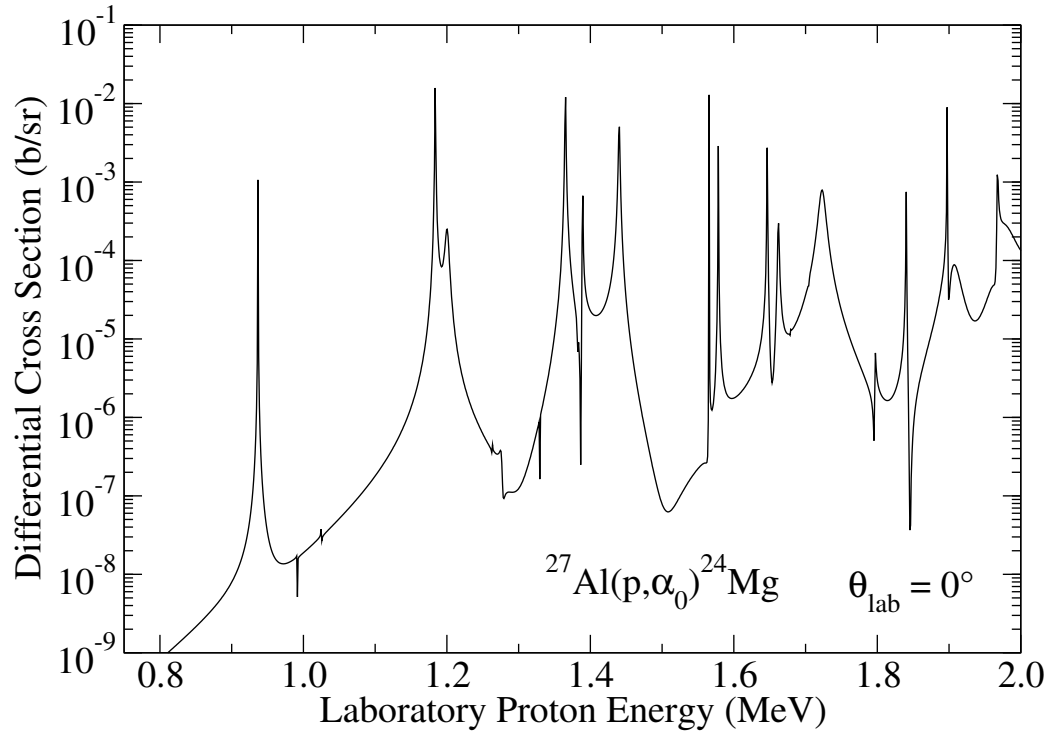


Figure 1.2. Cross section for the  $^{27}\text{Al}(p, \alpha)^{24}\text{Mg}$  reaction around the energy range of interest for the experiment. Shown is the differential cross section at  $\theta_{\text{lab}} = 0^\circ$ , as St. George is designed to study reactions at  $0^\circ$ . From [17], produced by AZURE2 [4]

The cross section for charged particle reactions drops off precipitously by orders of magnitude as the energy decreases due to repulsion from the Coulomb barrier. To aide in visualization of the cross section, we can remove the trivial contribution to the cross section of the Coulomb repulsion, where our resulting energy-dependent component is called the *astrophysical S-factor*. The *S*-factor is defined in reference to the energy-dependent cross section  $\sigma(E)$  as

$$\sigma(E) \equiv \frac{1}{E} e^{-2\pi\eta} S(E),$$

where  $\eta = Z_0 Z_1 e^2 \sqrt{\mu_{01}/2E\hbar^2}$  is the Sommerfeld parameter and  $Z_i$  is the charge state of the particles in question. The term  $\mu_{01}$  is the reduced mass of the system, given as  $\mu_{01} = m_0 m_1 / (m_0 + m_1)$ . The full Gamow factor  $\exp(-2\pi\eta)$  is the probability that an s-wave nuclei penetrates the Coulomb barrier and represents the strong decrease in the cross section at lower energies. This formulation removes the s-wave contribution and the known low-energy dependence of nuclear cross sections on  $E$ , resulting in a much more slowly varying function.

### 1.2.2 Reaction Rate

Under astrophysical conditions, instead of focusing on the probability of a single reaction taking place, it is common to discuss the number of reactions that take place in a given volume as a function of the interior temperature of the burning process. We can define a quantity called the *reaction rate* that describes the number of reactions within a given volume per unit time in terms of the energy-dependent cross section  $\sigma(E)$  as

$$N_A \langle \sigma \nu \rangle_{01} = N_A \left( \frac{8}{\pi \mu_{01}} \right)^{1/2} \frac{1}{(kT)^{3/2}} \int_0^\infty E \sigma(E) e^{-E/kT} dE, \quad (1.1)$$

where the term  $\exp(-E/kT)$  originates from the Maxwell-Boltzmann distribution [22]. Based on the knowledge of the temperature of the stellar interior, the reaction rate

can be calculated for any reaction, given the cross section.

For those stellar interiors, there are some center of mass energies that are most important for the determination of the reaction rate. The reaction rate is most sensitive to the cross section at energies where the product of the two exponential terms,  $\exp(-E/kT)$  and  $\exp(-2\pi\eta)$ , is near their maximum. This distribution can be approximated by a gaussian peak, with the central energy called the *Gamow energy*, given by

$$E_{\text{Gamow}} = \left[ \left( \frac{\pi}{\hbar} \right)^2 (Z_0 Z_1 e^2)^2 \left( \frac{\mu_{01}}{2} \right) (kT)^2 \right]^{1/3},$$

and the width of the peak describing the *Gamow window* given by

$$\Delta_{\text{Gamow}} = \frac{4}{\sqrt{3}} \sqrt{E_{\text{Gamow}} kT}$$

under this approximation [22]. The Gamow window is useful in guiding measurements to the most important energy range to study a given reaction. When there are no resonances within this energy range, the extrapolation of the *S*-factor to these lower energies is much easier, as the energy dependence of the cross section can be well estimated.

### 1.2.3 Resonances

Neglecting nuclear structure effects, the above description encompasses what is necessary to determine how the nuclear reaction progresses in stellar interiors. This simplistic interpretation, however, cannot be applied to most reactions due to the effect of the energy levels within the compound nucleus that is formed in the reaction. For the  $^{27}\text{Al}(p, \alpha)^{24}\text{Mg}$  reaction, the compound nucleus  $^{28}\text{Si}$  has a number of energy levels that can affect the yield of the reaction, with two of those levels shown schematically in Fig. 1.3.

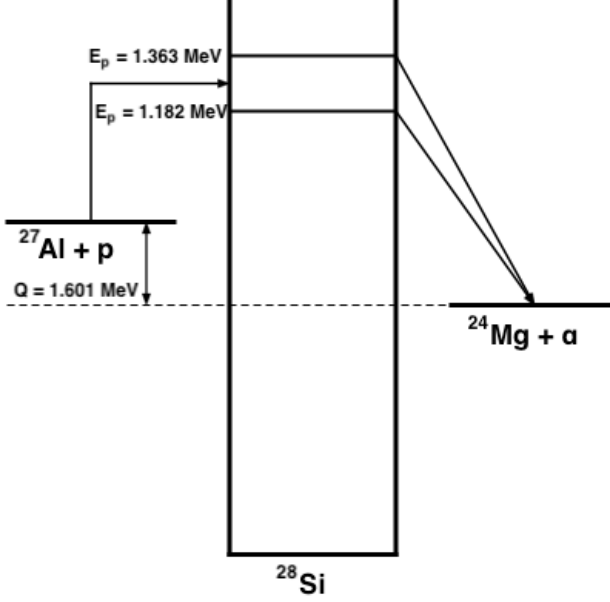


Figure 1.3. Energy diagram for the  $^{27}\text{Al}(p, \alpha)^{24}\text{Mg}$  reaction, showing two resonances accessible for study at zero degrees.

In cases where the center of mass energy of the system is close to one of these energy levels, the reaction is said to be *on resonance* or a resonant reaction. Resonances can be observed in the cross section (see Fig. 1.2) where there is a large increase in the cross section over a narrow energy range. Resonances can dominate the astrophysical reaction rate due to their higher cross section even in cases where the resonance falls outside of the Gamow window. In cases where resonances dominate, the reaction rate can be simplified to only consider the contributions from the resonances as

$$N_A \langle \sigma \nu \rangle = N_A \left( \frac{2\pi}{\mu_{01} kT} \right)^{3/2} \hbar^2 e^{-E_r/kT} \omega \gamma,$$

where  $E_r$  is the resonance energy and  $\omega \gamma$  is the resonance strength [22]. In cases where multiple isolated resonances contribute to the reaction rate, the resonance-dependent

term is instead a summation over the resonances, or

$$N_A \langle \sigma \nu \rangle = N_A \left( \frac{2\pi}{\mu_{01} kT} \right)^{3/2} \hbar^2 \sum_i e^{-E_{r,i}/kT} \omega \gamma_i.$$

Since resonances have a profound effect on astrophysical reaction rates, their study and characterization are often an important focus of measurements.

#### 1.2.4 Angular Properties

The angular dependence of the cross section depends sensitively on the spin-parities of the resonances, i.e. the energy levels within the compound nuclear state. The spin and parity of the nuclear states available for resonant reactions are determined by the quantum mechanical selection rules from the spin, parity, and angular momentum of the target and projectile nuclei, given as

$$|\ell_p - J_{p\text{-}} - J_{27\text{Al}}| \leq J_{28\text{Si}} \leq |\ell_p + J_{p\text{-}} + J_{27\text{Al}}|$$

and

$$\pi_{28\text{Si}} = \pi_p \pi_{27\text{Al}} (-1)^{\ell_p},$$

where the properties of the compound nuclear state in  $^{28}\text{Si}$  are  $J_{28\text{Si}}$  and  $\pi_{28\text{Si}}$ , and  $\ell_p$  is the orbital angular momentum of the incident proton. Given that the ground state of  $^{27}\text{Al}$  is  $5/2^+$  and the spin-parity of protons is  $1/2^+$ , we have an entrance channel spin of  $j_s = 2$  or  $3$ , where  $j_s = j_p \oplus j_{27\text{Al}}$ .

For the remainder of the discussion, we will focus on the two resonances that are studied as part of this dissertation, with the properties shown in Table 1.1.

Our allowed values for  $\ell_p$  are 0, 2, and 4 due to parity, where  $\ell_p = 0$  only contributes in the  $j_s = 2$  case. The entrance channel thus is a mixture of different components, based on the allowed angular momenta. In the exit channel

$^{24}\text{Mg} + \alpha$ , we can perform similar calculations. Since both the ground state of  $^{24}\text{Mg}$  and the spin-parity of  $\alpha$  are  $0+$ , we are restricted to natural parity states within  $^{28}\text{Si}$  ( $J^\pi = 0+, 1-, 2+, \dots$ ), which includes our resonances. Since our resonances are  $J^\pi = 2+$ , the only allowed orbital angular momentum for the  $\alpha$  particle is  $\ell_\alpha = 2$ , which means that there is no mixing in the exit channel.

TABLE 1.1  
RESONANCE PARAMETERS

Property, Units	Low	High
$E_x$ , MeV [40]	12.726	12.902
$E_p$ , MeV	1.182	1.363
$J^\pi$ [34]		$2^+$
$W(\theta)$ [2]		1
$Q$ , MeV		1.601

Since we are observing our reaction products within a small solid angle, we need to consider the angular correlation of the produced  $\alpha$  particles to the incident proton beam. We can relate the differential cross section to the angular correlation  $W(\theta)$  between the two outgoing particles  $b$  and  $B$  (in our case the  $\alpha$  and the heavy recoil) with

$$\left( \frac{d\sigma}{d\Omega} \right)_\theta = \frac{1}{4\pi} \sigma W(\theta),$$

where  $\theta$  is the angle between the two outgoing particles and  $\sigma$  is the cross section

at the energy of interest [22]. The two resonances in question have been shown to be isotropic, so  $W(\theta) = 1$  [2]. For those resonances that are not isotropic, the measurement of particle yields at multiple angles can be used to determine the angular correlation of the produced particles and can inform the assignment of state spins and parities (see for example [18]).

### 1.3 Recoil Separation

The experimental process in which the reaction products produced by a direct beam can be filtered out from that direct beam in order to be detected is called *recoil separation* or alternatively *recoil mass separation*. A recoil separator is the system, consisting of a sequence of electromagnetic elements, designed to perform this task.

#### 1.3.1 Motivation

Recoil mass separation was conceived as an alternate way to measure the cross sections of radiative capture reactions. These reactions had previously been studied by detecting the produced  $\gamma$  rays, which are potentially subject to high background count rates near the energy of interest and low detection efficiency for the produced  $\gamma$  rays. The heavy reaction product can instead be detected by a detector situated behind the target, assuming that the target is thin enough to allow the produced recoils to leave the target. In this thin target case, the incident beam will likely pass through the target as well, making it a source of background at the detector plane. In the cases of interest for nuclear astrophysics, this background count rate could be a factor of  $\times 10^{15}$  or larger than the particles of interest and could damage the or at least saturate the detector.

The produced recoils may be filtered out from the incident beam by electromagnetic elements situated between the target and the detector. For example, if we are looking at radiative alpha capture reactions  $A(\alpha, \gamma)B$ , the interaction between the

heavy incident beam with mass  $A$  and linear momentum  $p$  and the  $\alpha$  particles within the target produces a heavy compound nucleus with mass  $A + 4$  and momentum  $p$ . Ignoring the effect of the emitted  $\gamma$  ray on the momentum and assuming that there is no spread in the momentum, the use of electrostatic elements can separate the recoils from the beam based on their different magnetic and electric rigidities. The magnetic rigidity is defined as

$$B\rho = \frac{p}{q} = \frac{\sqrt{2mT}}{q} \text{ [Tm]}, \quad (1.2)$$

where  $p$ ,  $q$ ,  $m$ , and  $T$  are the momentum, charge state, mass, and kinetic energy of the desired particle, respectively. The magnetic rigidity defines the trajectory of the particle's movement within a homogeneous magnetic field of strength  $B$  along a circular path with radius  $\rho$ . Similarly, the electric rigidity is defined as

$$E\rho = \frac{pv}{q} = \frac{2T}{q} \text{ [MV]} \quad (1.3)$$

with the same variable definitions as before, and defines the circular trajectory a particle takes within an electric field of strength  $E$ .

With a single momentum and velocity (or kinetic energy) selected for, the recoil particles of interest can be uniquely identified by the optical system. The design of recoil separators make use of this relatively simple idea as the basis of their design. Despite this, there have been relatively few recoil separators that have been brought into service due to the complexities of their design and operation that are not adequately taken into account in this description.

### 1.3.1.1 Inverse Kinematics

Reactions may be studied in two “configurations”, as defined by which particles are the target and the projectile: forward and reverse kinematics. We will discuss

each of these options in turn.

In forward kinematics, a beam composed of relatively lighter nuclei is directed onto a target made up of relatively heavy nuclei, with the produced heavy recoil staying primarily within the target and the light ejectile being the particle to be detected by the detector system. We will write this reaction as  $A(a,b)B$ , where  $A$  and  $B$  are the heavy particles. For radiative capture reactions, the light ejectile  $b$  is a  $\gamma$  ray which must be detected by a photon detector which either has low resolution or a relatively low efficiency and is subject to background. In cases where the emitted  $\gamma$  has energy similar to exceedingly strong background lines, the detection of the produced  $\gamma$  can be almost impossible. As many reactions of astrophysical interest are radiative capture (( $p,\gamma$ ) or ( $\alpha,\gamma$ )), these complications can prevent the study of some important reactions. Contaminant nuclei within the target can have the same effect, where a reaction channel with the contaminant nuclei has the same  $\gamma$  energy as the desired reaction, preventing the direct detection of the desired reaction.

Studying a reaction in reverse kinematics can help avoid some of these problems. In reverse kinematics, a heavy projectile is impinged on a target made up of lighter nuclei, and the heavy recoil is detected by the detection system, or  $a(A,B)b$ . For radiative capture reactions, the produced  $\gamma$  may also be detected in coincidence with the primary detection system to further reduce background, if desired, with an accompanying loss in efficiency. Since the heavy recoil is detected, a high-efficiency particle detector, such as a solid state detector, can be used. Since reactions of astrophysical interest in the energy regions of astrophysical interest are commonly lower in cross section, the ability to detect the infrequently-produced heavy recoils with high efficiency can make the study of that particular reaction experimentally feasible. For reactions of astrophysical interest, often the target of choice is a  $^1\text{H}$  or  $^4\text{He}$  gas cell or jet. While these targets have their own complications, they can also be made isotopically pure, reducing additional background from contaminants within

the target.

A primary source of background for reactions studied in reverse kinematics is beam-induced background. The emitted recoils are emitted within a small solid angle cone oriented along the incident beam direction, co-linearly with the unreacted beam that passes through the thin, light nuclei target. In order to detect those produced recoils, the recoils must be separated or filtered out from the unreacted beams, which can be accomplished through an electromagnetic separator such as a recoil mass separator.

### 1.3.1.2 Radiative Capture

When studying radiative capture reactions  $A(a, \gamma)B$ , the emitted  $\gamma$  arises from the decay of the excited state within the compound nucleus  $B$  as it is emitted. Radiative capture reactions produce a compound nucleus in an excited state that has the same linear momentum as the beam in the lab frame, given as

$$p_{\text{recoil}}^* = \sqrt{2m_a E_a},$$

where  $*$  denotes that the recoil is in an excited state. When this state de-excites, it produces a  $\gamma$  ray, either due to a single transition to the ground state or a cascade of  $\gamma$ s through intermediate states. As  $B$  is produced in an excited state, the  $\gamma$  may be emitted in any direction, which affects the final momentum of the recoil.

If the  $\gamma$  is emitted along the  $z$ -axis (the incident beam direction), the momentum of the final recoil is given by

$$p_{\text{recoil}} = \sqrt{2m_a E_a} \pm p_\gamma,$$

where  $p_\gamma = E_\gamma/c$ . In this case, no angular change is imparted to the recoil, so it can be assumed to still be traveling along the beam axis. At the opposite end, if the  $\gamma$  is

emitted perpendicular to the beam axis, there is a maximal angular change, where the lab angle of the recoil is given by

$$\theta_{\text{recoil}} = \tan^{-1} \left( \frac{p_\gamma}{\sqrt{2m_a E_a}} \right).$$

There is a small change to the total momentum of the recoil from the imparted transverse momentum from the emitted  $\gamma$ . In cases where the  $\gamma$  is emitted somewhere between these two extremes, there will be a smaller angular change imparted than the transverse case and a smaller momentum change than in the longitudinal case.

In this case, the emitted recoils are confined within a forward cone with some opening angle and with some momentum spread. The various properties of the separator will be based on these kinematic properties for the reactions of interest. For those reactions that have smaller acceptance cones or energy spreads than what the separator was design for, studying those reactions becomes easier. The final design for the recoil separator will take into account both the central value of the recoil momentum distribution as well as the limits for the angular and momentum distribution. We can consider the momentum and energy distributions as essentially interchangeable, since the mass of the desired recoil is known.

### 1.3.2 Beam Optics

The understanding of how recoil separators work is grounded in the theory of beam optics which describe the effect of electric and magnetic fields on moving charged particles. These moving particles are focused and directed by the electromagnetic elements, and their action on particles can be modeled and optimized to transport particles with various properties down a beam line to a desired location.

### 1.3.2.1 Mass Dispersion

A recoil separator is designed to have a mass dispersion such that at least one point within the separator causes the incident beam with a different mass to be rejected. This location is commonly before the detector plane to avoid the potentially high count rates from the high intensity incident beam.

Mass dispersion can be described by the coefficients within the designed transport matrix at the point where the mass dispersion should be located within the separator. A matrix element term ( $a|b$ ) can be understood to be the effect on  $a$  at the focal plane given the value of  $b$  at the target location. We can determine the distance in the dispersive  $x$  plane between the incident beam and the desired heavy recoils to first order as

$$x = (x|x)x_0 + (x|\theta)\theta_0 + (x|\delta_E)\delta_E + (x|\delta_M)\delta_M,$$

where  $\delta_E = \Delta E/E_0$  and  $\delta_M = \Delta M/M_0$  are the energy and mass dispersions, respectively [16]. The matrix elements can be understood as their effect on the final position of the particle in question in relation to its position at the target location, where the coefficient in question either represents a focusing or a divergence along the horizontal axis. Each coefficient is the amount of focus or divergence given the particle trajectory at the target location and is based on all of the intervening magnetic and electrostatic elements along the beamline.

The coefficient ( $x|x$ ) is the magnification of the beam spot, so independent of any other effects, the spot at the mass separation plane is larger or smaller based on the magnitude of the coefficient. Similarly, the coefficient ( $x|\theta$ ) describes the angular dependence of the horizontal beam spot. The coefficient ( $x|\delta_E$ ) is the energy dispersion, so the change in beam spot size due to the difference in energy from the central tuned energy for the separator. Finally, the coefficient ( $x|\delta_M$ ) is the mass dispersion, which describes the change in horizontal position based on the difference

in mass from the central tuned particle.

At the mass separation plane, the spot size of the beam should be independent of the energy and angular properties at the target location. In this ideal case, the angular and energy acceptance would be limited by the physical constraints of the separator and not its electromagnetic settings. To achieve this goal, the coefficients  $(x|x)$ ,  $(x|\theta)$ , and  $(x|\delta_E)$  should be zero or as close to zero as possible. In reality, these coefficients may be small but non-zero, resulting in a limit to the angular and energy acceptance of the separator. At the same time, the mass separation properties of St. George are controlled by the coefficient  $(x|\delta_M)$ , so this value is required to be non-zero and preferably large in magnitude in order to separate out the incident beam particles from the produced reaction particles, rejecting the former and sending the latter through the rest of the separator toward the detector system.

To higher orders, the design of the transport matrix and through that the decision on what electromagnetic elements and their properties for the physical recoil separator need to be designed by some computational codes. Within the physical separator, at least two of the available dispersive elements magnetic dipole, electric dipole, or Wien filter must be used to achieve a dispersion at a focal plane of mass/charge [16]. In order to leave that dispersion at the focal plane, either magnetic and electric dipoles or a magnetic dipole and Wien filter must be used. While a single element of each type is the minimum requirement, physical separators commonly have multiple elements due to the physical nature of the beam envelope within the beam line and the restrictions of the physical laboratory space.

### 1.3.2.2 Beam Suppression

Recoil separators must achieve a certain level of beam-induced background suppression, henceforth *beam suppression*, in order to observe the relatively uncommon produced recoils from the reaction. This beam suppression can be achieved by the

separator and detector system combined, with a majority of the beam suppression obtained by the separator. We will define beam suppression as

$$S = \frac{N_{b,\text{incident}}}{N_{b,\text{detector}}},$$

or the number of incident beam particles that will lead to a single beam particle detection at the detector system. Beam suppression is linked to the reaction in question, the rigidities of the beam and recoil, the energies of interest, and the detector system used. Values of  $S$  for existing separator systems will be cited, with larger values more successful at rejecting beam and more able to measure cross sections with lower yields.

### 1.3.3 Recoil Separator Facilities

The use of recoil separators to study radiative capture reactions has been explored recently at a number of facilities. The design of St. George is based on the knowledge gained from the design, construction, and operation of these previous recoil separator systems. The entire system, inclusive of the beam source, target, and detector, must be discussed as a whole when evaluating the capabilities of a given separator.

Recoil separators have been used for a variety of physics programs, such as heavy element searches, recoil-gamma spectroscopy, spin distributions, accelerator mass spectrometry, and nuclear astrophysics [16]. Since the St. George recoil mass separator was designed to be used primarily for reaction studies focused on nuclear astrophysics, our discussion will focus on those separators also aligned with this goal.

The primary distinction between recoil separator design comes from the choice of elements to provide the recoil separation and transport through the entirety of the separator. These elements may be magnetic dipoles, which bend the beam and provide a  $p/q$  selection, electrostatic analyzers that provide an  $E/q$  selection, or a

cross electric-magnetic field setup called a Wien filter that selects for a single velocity  $v = E/B$ . Additionally, focusing elements such as magnetic quadrupoles (or higher order pole configurations) are required to aide in transport of the desired particles that enter into the separator to the end within some acceptable bound. The individual choices of these elements and their position within the separator need to be carefully considered in order for the separator to be used to study the required reactions.

#### 1.3.3.1 CalTech Separator

The design and use of recoil separators for nuclear astrophysics research was pioneered by Smith *et al.* [41]. This separator was a proof-of-concept design to determine the feasibility of performing reaction studies with this technique. The design of recoil mass separators specifically designed to study reactions of astrophysical interest is similar to the design and operating characteristics of similar recoil separators designed and built around the same time, and many of the decisions made for optimal characteristics of the separator system have been replicated by more modern separator systems.

The primary considerations for the design of the CalTech separator were based on the study of radiative capture reactions in inverse kinematics using radioactive isotope beams with near-complete rejection of the incident beam before the detector system. The separator achieved the mass separation by using a Wien filter to provide initial velocity selection, an electrostatic deflector created by extending the Wien filter's electrostatic plates beyond the magnetic field limits to provide energy selection, and a magnetic dipole to provide momentum selection [41]. Additional experimental choices used for this separator system, such as the use of an offset Si detector at the target location to monitor beam current indirectly or the use of a  $\gamma$  detector in coincidence with the final detector system to provide additional beam suppression, have been replicated in subsequent systems. During initial experiments, beam suppression on

the order of  $10^{10}$  was observed [41].

### 1.3.3.2 ARES

The Astrophysics REcoil Separator (ARES) was built at Louvain-la-Neuve to study  $(p, \gamma)$  and  $(\alpha, \gamma)$  reactions using radioactive incident beams provided by the CYCLONE44 cyclotron [3]. Self-supporting solid targets, containing the required H or He, were used for the reaction studies. The system was designed with a single magnetic dipole for charge selection and a Wien filter for velocity selection, along with multiple magnetic quadrupoles (one triplet and two doublets) to maintain the transportation of the produced recoil particles to the detector system. The condensed and limited size of the separator is based on the constraints of the experimental hall [14]. The detector system consists of a single  $\Delta E - E$  gas telescope which discriminated the reaction products from the remaining incident beam particles. The initial test of the separator used a stable incident beam to compare to results obtained by other methods within the lab, and the focus of the initial work was on low-lying resonances of astrophysical interest.

### 1.3.3.3 DRAGON

The DRAGON recoil separator at TRIUMF-ISAC was built for the same reasons as ARES, but differs in the actual construction and usage of the separator. The separator uses two large magnetic dipoles and two large electrostatic dipoles for its momentum and energy selection [19]. The primary target is an extended gas target, which is used with the incident radioactive beams for nuclear astrophysics studies near the valley of stability.

DRAGON has been successful at measuring reactions with radioactive and stable beams, such as  ${}^{20}\text{Ne}(p, \gamma){}^{21}\text{Na}$ ,  ${}^{21}\text{Ne}(p, \gamma){}^{22}\text{Na}$ , and  ${}^{24}\text{Mg}(p, \gamma){}^{25}\text{Al}$  [19]. Due to using primarily radioactive beams, reaction studies at DRAGON focus on low energy reso-

nances due to the extremely low cross sections and beam intensities involved. Beam suppression on the order of  $10^8 - 10^{13}$  was observed, depending on the reaction in question [19].

#### 1.3.3.4 ERNA

The European Recoil separator for Nuclear Astrophysics (ERNA) at Bochum was designed to study the  $^{12}\text{C}(\alpha, \gamma)^{16}\text{O}$  reaction in inverse kinematics at energies near the Gamow window [37]. This reaction has a large spread in both angle and energy, making the transport of the produced recoils to the detector plane more difficult.

ERNA uses two Wien filters and a single magnetic dipole to provide the velocity and momentum separation. The primary target is an extended gas target with offset Si detectors to measure the elastic scattering yield to monitor the beam current [27]. ERNA has been used to measure  $^{12}\text{C}(\alpha, \gamma)^{16}\text{O}$ ,  $^3\text{He}(\alpha, \gamma)^7\text{Be}$ , and other astrophysically important reactions at low center-of-mass energies important for nuclear astrophysics. For the  $^3\text{He}(\alpha, \gamma)^7\text{Be}$  reaction, beam suppression in the range  $10^{10} - 10^{12}$  was observed [27].

#### 1.3.3.5 DRS

The Daresbury Recoil Separator [6] was not originally designed to study radiative capture reactions, but after being moved to Oak Ridge National Laboratory, was successfully used to study numerous reactions, such as  $^{17}\text{F}(\text{p}, \gamma)^{18}\text{Ne}$  [13]. The separator contained two Wien filters, a single dipole magnet, three quadrupole triplets, and two magnetic hexapoles to provide higher-order corrections to the transport matrix. For reaction studies, well-known reactions using stable beams were performed in order to determine the separator properties and the detector response for the expected recoils at the focal plane. Due to the low particle currents for radioactive beams, studies were focused on resonance energies for the reactions.

### 1.3.3.6 St. George

The separator consists of six dipole magnets, eleven quadrupole magnets, and a Wien filter. The separator was designed to accept recoils with a maximum energy and angular spread of  $\Delta E/E = \pm 7.5\%$  and  $\Delta\theta = \pm 40$  mrad, respectively, and to provide a mass separation of  $m/\Delta m = 100$  and beam suppression of a factor  $\geq 10^{15}$ . Combined with the HIPPO (High-Pressure Point-like target) supersonic gas jet target, St. George will be primarily used to study low energy  $(\alpha, \gamma)$  reactions using stable beams [25]. The use of high-intensity stable beams allows for measurements of the cross section outside of regions where resonances dominate.

### 1.3.4 Requirements

Each recoil separator needs to be properly understood before the experimental results produced using it can be trusted. The primary properties of the separator, namely the energy and angular acceptances and the beam suppression, must be verified using a variety of techniques and test beams in order to determine the expected performance of the separator. These tests should be performed in the energy range of interest with beams consisting of nuclei with similar properties, such as the mass and charge state, as those that will be produced during experimental campaigns. Once the properties of the separator are well understood, quantified, and hopefully consistent with the design parameters, the experimental results obtained from the separator can be adequately related to the astrophysical process that includes the reaction in question. Since some of these measurements require high precision, characterizing the recoil separator is a long and involved task.

To that effect, the commissioning and experimental results produced with St. George during the initial phases of its use for studying reactions of astrophysical interest will be presented within. The commissioning work discussed covers the energy acceptance up to the final detector plane, and the angular acceptance and the beam

suppression up to the focal plane after the Wien filter. The first reaction study using the partially commissioned St. George will be discussed. The initial experiment is a study of the  $^{27}\text{Al}(\text{p}, \alpha)^{24}\text{Mg}$  reaction at two prominent resonances. Finally, the plan for improving the use of St. George for non-standard reactions, namely those that are not  $(\alpha, \gamma)$  reactions, will be laid out.

## CHAPTER 2

### EXPERIMENTAL SETUP

All experimental work was performed at the Nuclear Science Laboratory (NSL) at the University of Notre Dame, using the St. Ana 5U-4 accelerator and St. George. Commissioning work for the separator began in 2014 and is currently on-going (see Section 3.3). The experiment discussed herein consisted of three separate runs, each one week long, in December 2016 and February 2017. The first run tested a proposed close location for the detection system, the second run characterized the additional magnets required for a far location for the detection system, and the third run was the primary data collection run.

The accelerator provided a high intensity proton beam to St. George for the first and third runs, and a high intensity  ${}^4\text{He}^+$  beam for the second characterization run. A 16-strip Si detector was installed at the two different focal planes to detect the produced  $\alpha$ -particles from the  ${}^{27}\text{Al}(\text{p}, \alpha){}^{24}\text{Mg}$  reaction. Incident beam rejection was on the order of  $1.5 \times 10^{12}$  for the runs at the resonance peak.

#### 2.1 The St. Ana Accelerator and Transport Line

St. ANA (Stable beam Accelerator for Nuclear Astrophysics) is a 5 MV vertical, single-ended pelletron accelerator at the NSL, providing high-intensity stable beams to a number of experimental setups within a dedicated target room. The original designation of the accelerator by the manufacturer, National Electrostatics Corporation, was the 5U-4, denoting the five individual acceleration sections and the four charging chains, causing the accelerator to commonly be referred to as the *5U*. Both names

will be used interchangeably throughout this work. The 5U is shown schematically in Fig. 2.1

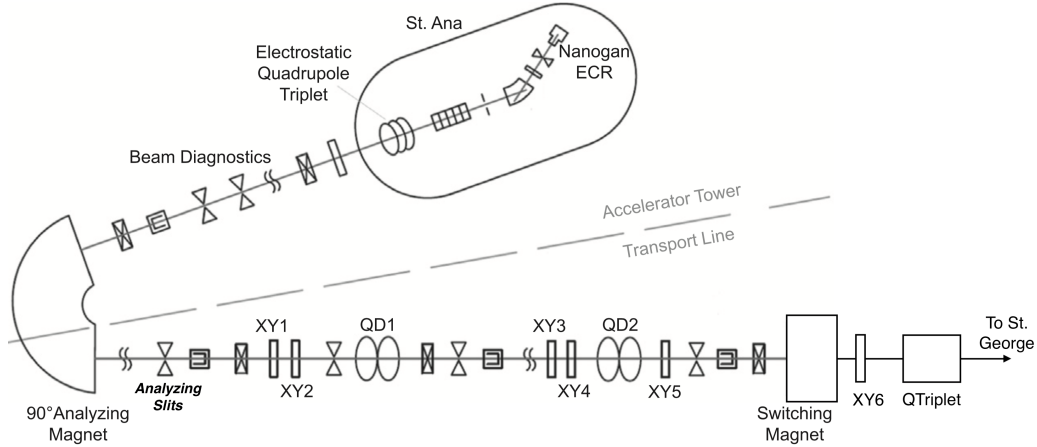


Figure 2.1. Schematic of the 5U accelerator and transport beamline. The steering elements  $XY\#$  and focusing quadrupole doublets  $QD\#$  are used to direct and focus the beam to St. George. The transport line is used to prepare the beam for experiments and is not adjusted after that preparation. Adapted from [31].

The 5U accelerates a high-intensity ion beam produced by the Nanogan Pantechnik ECR source to the desired energy by energizing the terminal shell to high voltage. The acceleration tube, extending from the bottom of the shell to the bottom of the accelerator, steps that voltage down through a series of resistors and plates, creating an electric field gradient along the tube that accelerates the positively charged ion beam down and out of the accelerator. The beam is then bent around a  $90^\circ$ dipole magnet, called the analyzing magnet, and through a pair of vertical slits, called the analyzing slits, that provide energy identification of the beam. In addition, the current on the slits can be used as a feedback control system to regulate the voltage on

the terminal shell when the accelerator is being run in “slit control mode,” providing a highly stable beam with a small energy spread. A recently performed  $^{27}\text{Al}(\text{p}, \gamma)^{28}\text{Si}$  resonance scan [20] was used to determine the beam energy spread of  $\sigma_{\text{beam}} \approx 0.3$  keV near a beam energy of  $E_{\text{beam}} = 1320$  keV. The 5U also contains focusing, directional, and diagnostic elements used to help tune the accelerator to provide a stable and well-behaved beam.

The transport beamline directs the analyzed beam to the desired experimental area through use of focusing and directional elements: two magnetic quadrupole doublets maintain a focused beam along the beamline; the magnetic dipole switching magnet directs the beam down one of the available experimental beamlines; and magnetic steerers shift and turn the beam within the beamline. The steerers act to maintain the beam along the magnetic optical axis of the quadrupoles and maximize the amount of beam being transported down the beamline from the accelerator. Sets of diagnostic equipment are also installed at various locations along the beamline to help monitor and restrict the beam, and the entire system is kept at a high ( $\approx 8 \times 10^{-8}$  torr) vacuum through use of multiple turbo-molecular pumps located along the beamline.

The final section of the transport line is between the switching magnet and the entrance to St. George. This section of beamline prepares the beam to have the required characteristics at the target location and contains a single magnetic steerer (horizontal and vertical) and a magnetic quadrupole triplet along with diagnostic equipment. The final magnetic steerer is used to finalize the alignment of the beam, and the magnetic quadrupole triplet creates a small, well-focused beam at the target location.

## 2.2 The St. George Recoil Separator

The St. George is a recoil mass separator at the NSL [15] and one of the experimental beamlines accessible to the 5U. The layout of St. George is shown in Fig. 2.2. The design and operation is based on previous recoil separators (see Sec. 1.3.3). The separator consists of six dipole magnets, eleven quadrupole magnets, and a Wien filter. The separator was designed to accept recoils with a maximum energy and angular spread of  $\Delta E/E = \pm 7.5\%$  and  $\Delta\theta = \pm 40$  mrad, respectively, and to provide a mass separation of  $m/\Delta m = 100$  and beam suppression of a factor  $\geq 10^{15}$ . The design was guided by the desire to efficiently measure  $(\alpha, \gamma)$  reactions with a beam mass up to  $A = 40$  with high beam intensities and to fit the separator within the physical limitations of the target room at the NSL [15].

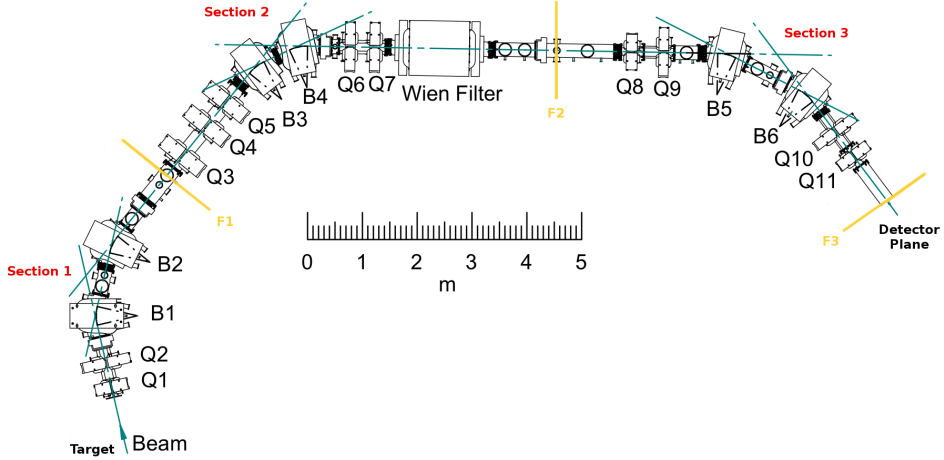


Figure 2.2. Layout of the St. George recoil separator. Quadrupoles are identified by  $Q$ , dipoles by  $B$ , and focal planes by  $F$ . Section labels are placed near the dipole doublet within that section, and boundaries are the intervening focal planes. Adapted from Reference [15].

The separator is designed to transport recoils within a rigidity phase space relevant for measuring  $(\alpha, \gamma)$  reaction cross sections. The transportation of these ions is achieved by setting the magnetic and electrostatic elements within the separator, based on the rigidity of the ions. The design parameters restrict the magnetic (Eq. 1.2) and electric (Eq. 1.3) rigidities within the ranges  $0.1 \leq B\rho \leq 0.45$  Tm and  $E\rho \leq 5.7$  MV [15]

### 2.2.1 Subsections of St. George

The separator is divided into three sections, based on their purpose: the charge selection stage; the mass selection stage; and the clean-up stage. The stages are separated by the focal planes. Each of these stages will be discussed in turn.

The entire separator is tuned for a single  $B\rho - E\rho$  rigidity, defined by the central energy of the recoils and its mass and charge state (see Eqs. 1.2 and 1.3). For commissioning purposes, a direct incident beam was used as a “test beam” to tune the separator without having to perform a reaction. The tuned particles will travel down the central magnetic axis of the separator. Particles that differ in energy or angle from these central particles will travel through a different path (see Fig. 3.1).

The first section is the so-called *charge selection* stage, consisting of the first quadrupole doublet ( $Q_1Q_2$ ) and the first dipole doublet ( $B_1B_2$ ). The doublet  $Q_1Q_2$  focuses the recoils through the dipole pole gap, and the doublet  $B_1B_2$  provides the first rejection of beam due to the difference in magnetic rigidity from the desired recoils. After the first focal plane  $F_1$ , a single recoil charge state will be transported through the remainder of the separator. Horizontal slits may be placed at this focal plane to aide in the rejection of incident beam particles that have undergone a charge exchange event. Slits were not used during the commissioning work or during the primary experiment. At the end of this section, both beam and recoil particles are present within the separator.

The next section is the so-called *mass selection* stage, which contains the magnetic quadrupole triplet ( $Q_3Q_4Q_5$ ), the second magnetic dipole doublet ( $B_3B_4$ ), the second magnetic quadrupole doublet ( $Q_6Q_7$ ), and the Wien Filter (WF). This section's primary purpose is to reject the incident beam and create an achromatic focus at the second focal plane  $F_2$ . This focus is horizontally narrow at the focal plane to aide in the rejection of the beam. At this focal plane, a set of horizontal slits, called the mass slits, are placed to reject the remainder of the incident beam. The focused recoil particles will pass through the center gap between the slits. The mass resolution of the separator depends on the particle distributions of the beam and recoil being focused and spatially separated at this position, and that the tail of the beam distribution minimally overlaps with the recoil distribution.

The Wien filter operates by having crossed electric and magnetic fields, oriented such that individually they would bend a particle beam in opposite horizontal directions, as shown in Figure 2.3. From the beam's perspective, the electric field bends the beam to the right while the magnetic field bends the beam to the left. The fields are provided by a pair of electrostatic plates within the vacuum chamber and a magnetic dipole outside of the chamber. A Wien filter is set to allow for a single velocity to pass through the center of the element undeflected, according to  $v = E/B$ .

For St. George, the Wien filter provides the final mass selection for our recoils, allowing the beam particles to be filtered out from the recoil particles, since the mass difference between the two ( $\Delta m = 4$  when performing  $(\alpha, \gamma)$  reactions) translates into a velocity difference, as the momentum had been selected for earlier.

The simplified description above is not entirely accurate, since our beam and recoils exist within a phase space envelope confined by ranges of allowed positions, angles, and energies. Since we inherently have an energy distribution of our recoils deriving from the convolution of the beam energy uncertainty with the target losses of the beam and recoils and the energy change arising from the  $\gamma$  ray emission, we

do not have a mono-energetic recoil distribution passing through the center of the WF. When taken as a whole, the elements up to and including the WF create the proper beam and recoil properties to reject the incident beam based on their mass difference.

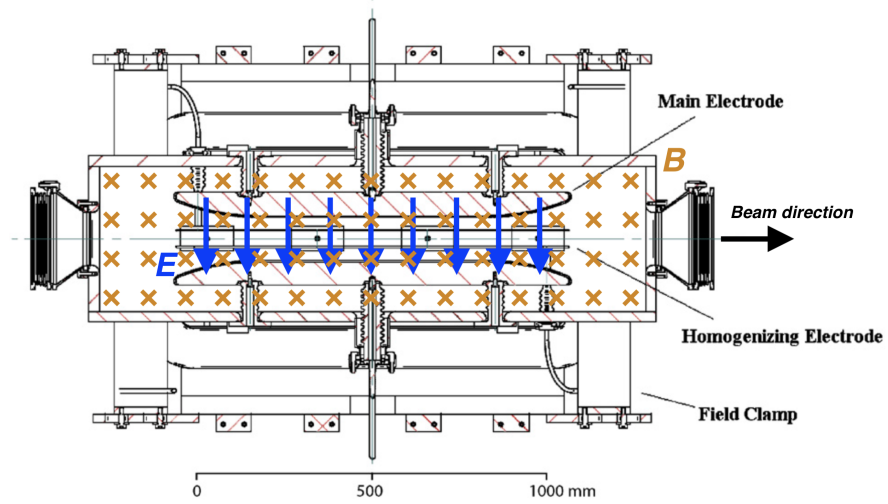


Figure 2.3. Schematic of the focusing and bending properties of the Wien filter installed in St. George. The crossed electric ( $E$ ) and magnetic ( $B$ ) fields allow particles with a single velocity to pass through undeflected.

Adapted from [15].

At this point, our beam envelope can be thought of as just our *recoil* envelope, where the particles still being transported through St. George are just those recoils produced in the reaction at the target location. In reality, the envelope still contains some beam particles, either through scattering off of the interior of the beam pipe, diagnostic elements, or the residual vacuum, or through charge changing events with the residual vacuum. Due to these factors, we cannot place the final detection system

right after the Wien filter and instead need additional elements to further reduce the background.

This final section of St. George is the so-called *clean-up* stage, where the phase space of the recoils passing through the mass slits are matched with the phase space of the detection system, providing the last rejection of the incident beam particles. This section consists of, in order, a quadrupole doublet ( $Q_8Q_9$ ), the last dipole doublet ( $B_5B_6$ ), and a final quadrupole doublet ( $Q_{10}Q_{11}$ ). These magnets transport the recoil particles that passed through the mass slits at  $F_2$  through the detection system installed at the detector focal plane  $F_3$ . Since the detection system has a defined physical acceptance size, these magnets must reduce the physical extent of the recoil envelope within this space.

### 2.2.2 Diagnostic Equipment

To aide tuning the beam, additional diagnostic equipment has been developed and installed at various points along the separator. This diagnostic equipment can be divided between three basic types: Faraday cups, slits, and quartz viewers. These first two equipment types are present within other beamlines and the primary transport beamline, while the third was adapted for St. George based on principles encountered when working with other beamlines. The positions of this equipment is denoted in Figure 2.4.

Faraday cups are beam stops that also provide the user with the beam current being captured by the cup. The cup consists of three main parts: the shield, the suppression, and the cup itself. This structure is attached to a linear motion drive, letting the cup be positioned in or out of the beam, and isolated from the beamline. The shield primarily protects the suppression from being hit by incident beam but, due to its isolation, is also a point to read out the current and determine the physical extent of the beam at that point. Ideally, all of the beam would enter the cup portion,

allowing the Faraday cup to determine the complete beam current at that location. Using the cup in this way as a tuning aide is possible since the cup locations were selected based on the beam optics properties, as those locations correspond to waist points of the beam. The suppression is necessary since electrons are emitted with energies in the rough range of 20 – 100 eV when the beam strikes the physical cup. By biasing the suppressor to  $-300$  eV, those electrons are directed back toward the cup, giving an accurate reading of the beam current actually hitting the cup.

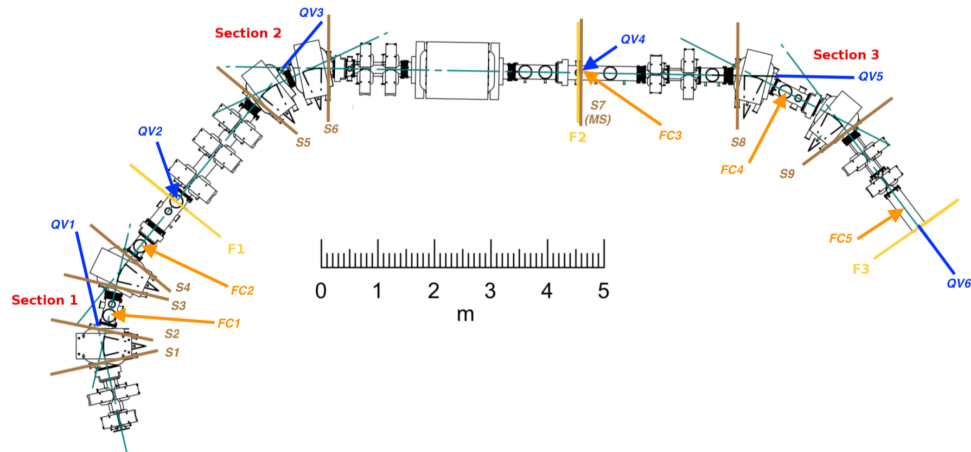


Figure 2.4. Locations of various diagnostic equipment within St. George. The slits (denoted  $S$ ) are installed at entrance and exit ports of dipoles and at the Wien filter focal plane. The isolated Faraday cups (denoted  $FC$ ) are located near focal planes and saddle points of the particle envelope within the separator. The quartz camera viewers (denoted  $QV$ ) are located at the exit ports of the dipoles and within the beam line at focal planes. Adapted from [15].

Slits are an additional way to determine the passing beam current but also provide information about the spatial size of the beam. These slits are Ta plates attached

to a linear motion, allowing the position to be controlled and determined from the exterior of the beamline. Each slit is isolated from the beamline, allowing the current hitting the slit to be read out at the console or to some other diagnostic program. The limiting factors for using these slits as a diagnostic device is their sensitivity, since unlike Faraday cups the slits used within St. George are not suppressed. The slits are then used as rough spatial diagnostics within the separator itself.

The quartz viewers used within St. George are divided between two types: an exterior quartz located at various exit ports, and an interior quartz that must be removed from the beamline. The locations of these camera systems are at the  $0^\circ$  exit ports of dipoles  $B_1$ ,  $B_3$ , and  $B_5$ , the end of the detector chamber, and at focal planes  $F_1$  and  $F_2$ . The quartz are used for beam alignment and tuning the magnetic and electric elements of St. George, as explained in Section 3.3. When beam strikes the quartz material, the quartz fluoresces and the camera mounted immediately behind records the image and transmits it to the control console. Since this fluorescence is dependent on the beam intensity, minimum currents of 200 nA are used to ensure that the beam shape can be accurately identified. Additionally, high intensity beams can melt the quartz material if left impinging on the system for extended periods of time, so maximum currents in the range of  $1.5 - 2.5 \mu\text{A}$  were used, depending on the actual beam particle selected.

### 2.3 Detector System and Data Acquisition

The full St. George detector system consists of a pair of micro channel plate based time-measurement detectors and a single 16-strip Si detector for energy deposition. Combined, this detection system provides particle identification by way of the *Time-of-Flight vs. Total Energy* method. As residual beam particles can make it to the detector plane, either through scattering or charge exchange events, particle identification is required to provide final discrimination and beam suppression (see, for

example, [23, 3, 19, 27] and others). As this experiment did not require the use of the full detection system, only the Si detector will be discussed further.

The Si detector is a Canberra PIPS (Passivated Implanted Planar Silicon) model PF-16CT-58\*58-300EB, which has a detector area of  $58 \times 58$  mm and is divided into 16 individual strips. The 16 strips allow for spatial resolution in one dimension, commonly taken to be the horizontal direction. For the experiment discussed herein, the detector was installed at focal plane  $F_2$ . Care was taken to ensure that the quartz viewer at that same location did not interfere with the operation of the detector.

The electronics for the experiment are relatively simple, needing only the energy signals from each of the 16 strips. A Mesytec MSCF-16 shaping filter amplifier provided amplification and signal shaping following the preamplifier, and a Caen V785 32-channel multi-event peak sensing ADC transformed those signals for the data acquisition system. Power to the detector was provided by Mesytec MHV-4 high precision bias supply unit, and was biased up to +40 V. Leakage current from the detector during the run was  $\approx 1.4 \mu\text{A}$ , but this high value was later shown to be due to the cable shielding internal to the beamline contacting the shielding installed to protect the detector when fully retracted. During the energy calibration runs where no detector shielding was present, the leakage current was  $\approx 0.3 \mu\text{A}$ . The electronics used are the same as for a standard St. George experiment, allowing for an additional test of a subsystem of the full acquisition system. Data was recorded using the VM-USB crate connected to the St. George DAQ computer.

## 2.4 Target Chamber

A commissioning target chamber was designed and built specifically for running the commissioning experiments and solid target studies. The chamber makes use of two of the turbo-molecular pumps from the Hippo target to provide a high ( $\approx 7 \times 10^{-8}$  torr) vacuum at the beginning of the separator and around the target

location. The commissioning chamber consists of a pair of electrostatic plates within a rotating chamber, a target ladder, and a Faraday cup. The rotating chamber allows the combined target ladder and electrostatic plates to rotate through a range of  $\approx 160^\circ$  (limited by the physical space around the target location) while maintaining a high vacuum, thus the target location does not need to be vented in order to change the angle of the target ladder and plates.

The electrostatic plates can be powered up to a maximum of 10 kV each from two single-phase high voltage power supplies and are operated remotely using an Arduino-based controller. The properties of the plates (length, width, separation, etc.) were determined such that the produced electric field would be as homogeneous as possible within the limited space and provide a beam deflection of up to 40 mrad from the target location, within the physical limits of the chamber. Experimentally, deflections of 45 mrad have been achieved, allowing a full angular phase space sweep to be performed. Switching the polarity of the deflector plates must be done at the power supplies. Since the test beam particles have a set electric rigidity  $E\rho$ , the maximum deflection of the particles may be limited by the upper voltage of the power supply. When not in use, the current striking the deflector plates could be monitored at the control console to use as an additional beam diagnostic.

The target ladder contains a 6.35 mm diameter collimator and a 2.06 mm collimator, separated by 11.1 mm. The large collimator is primarily used for mounting self-supporting solid targets, while the smaller collimator is primarily used for beam alignment and focusing purposes. The ladder is mounted on a high precision, manually controlled linear motion drive. The ladder may be fully removed from the beamline, and the central axis is aligned with the physical location of the jet target within Hippo. A thin Al foil was mounted for the experiment described herein.

The Faraday cup following the target chamber is an isolated FN-style cup. The back of the cup can be actuated open to allow beam to pass into the separator. The

Faraday cup allowed for beam with a maximum deflection of  $\approx 45$  mrad to enter St. George, as measured using the deflector plates. This larger angular acceptance at the beginning of the separator ensured that the diagnostic equipment did not have a detrimental affect on the experiment and based the final acceptance at  $F_2$  to be based on the specific tune of the separator. During some tests, the deflector plates were seen to intercept some of the beam when deflecting to 45 mrad, but since this value is again larger than the designed acceptance of St. George, this was deemed to not be detrimental.

## CHAPTER 3

### COMMISSIONING ST. GEORGE

The St. George recoil separator was designed to study a set of  $(\alpha, \gamma)$  reactions of astrophysical importance. To study these reactions, an energy acceptance of  $\Delta E/E = \pm 7.5\%$  and an angular acceptance of  $\Delta\theta = \pm 40$  mrad were necessarily based on the kinematic properties of those reactions [15]. When the separator is set such that it achieves the optimal ion optics for the system, the separator exhibits full acceptance of the recoils of interest while maximizing the beam rejection; these settings must be experimentally determined. These settings are the currents and voltages required to operate the electromagnetic elements, which may differ from those directly determined from the ion optics design. Measuring the acceptance achieved through various tunes and techniques is one way to determine if the desired transport properties have or have not been achieved experimentally. Recently, the energy acceptance was studied separately from the angular acceptance to provide a relation between the predicted and experimentally determined field values [31]. The angular acceptance was then studied through a variety of methods, both in conjunction and without a corresponding energy acceptance requirement. Measuring the acceptance of a separator is paramount to using it for experimental measurements.

Two primary commissioning campaigns, determining the angular and energy acceptances for a given desired global setting of the separator, have been undertaken. The two global settings are: (i) the designed parameters for St. George for transporting heavy recoil products produced by  $(\alpha, \gamma)$  reactions in inverse kinematics through the entire separator, and (ii) the modified parameters for transporting  $\alpha$  particles pro-

duced by  $(p, \alpha)$  reactions in forward kinematics to focal plane  $F_2$ . From each global setting, the separator elements can be scaled based on the desired particle’s magnetic (Eq. 1.2) and electric (Eq. 1.3) rigidities. The experimental settings for the separator achieving the required transport properties (acceptance and rejection) must be determined over a wide range of rigidities in order to ensure that the scaled settings still maintain the desired properties. Scaling the settings over a large range must make assumptions about *how* those elements scale which may or may not be representative of the experimental situation. Thus, determining the acceptance and rejection for a variety of particle rigidities that adequately cover the allowed rigidities and those expected for astrophysical reactions is a requirement for the full commissioning of the separator system. For the modified tune settings to measure  $(p, \alpha)$  cross sections, the required field settings were determined by using a direct  $\alpha$  beam at the expected energies. This situation is a special case due to the relatively small rigidity phase space covered by the experimental plan and the availability of a direct beam of the desired species, which most likely is not the case for many astrophysically-important reactions.

For the designed inverse kinematics separator settings, various beams spanning a large region within the desired rigidity phase space were used. Test beams included light beams ( $^1\text{H}$  and  $^4\text{He}$ ) due to their ease of production and heavier beams ( $^{16}\text{O}$  and  $^{20}\text{Ne}$ ) to simulate transporting heavy reaction products through the separator. The available test beams and their properties were based on the capabilities of the  $^{5}\text{U}$  and its ion source, including but not limited to the species in question, the charge state, energy, and intensity of the beam, and the overall stability of the system. Here stability is diagnosed by the beam current at the diagnostic equipment: a current with constant mean and small variance over time is considered a “stable” beam. This stability is based on the entirety of the experimental system, from the initial beam produced at the ion source to the power supplies used for the various tuning

elements along the beam line. The commissioning work was divided between focusing on the energy or angular acceptance relatively independent of the other. For some of the angular acceptance measurements, a small energy spread was included to better recreate the conditions under which St. George will be used.

### 3.1 Theoretical and Experimental Considerations

St. George was modeled using COSY Infinity (henceforth *COSY*), a beam optics and transport language developed at Michigan State University [28]. The initial ion optics solution for the separator was calculated by Drs. Couder and Berg at the University of Notre Dame to maximize the angular and energy acceptance for a point-like target located prior to the separator. Optimization of the individual elements' properties allowed the separator to achieve the previously-stated energy and angular acceptances, create an achromatic focus at the mass slits (focal plane  $F_2$ ), and transport all recoils to the final detector focal plane  $F_3$  (see Section 2.2). Each magnetic element is represented by a single command within the code, defining the type and properties of the desired element. The three types of elements used within St. George—dipoles, quadrupoles, and the Wien filter—require different sets of values to be defined. The recoil envelope, consisting of a number of sample recoil properties used as representative rays, for the final designed configuration is shown in Fig. 3.1. For the example shown, the quadrupole pole tip fields are given in Table 4.1, where negative values represent a quadrupole focusing in the  $y$ -direction. The pole tip fields for  $(\alpha, \gamma)$  experiments are for the test particles shown, while those for  $(p, \alpha)$  experiments are specific to this work. The actual fields used will depend on the rigidity of the desired particle to transport through the separator and can be scaled from these values.

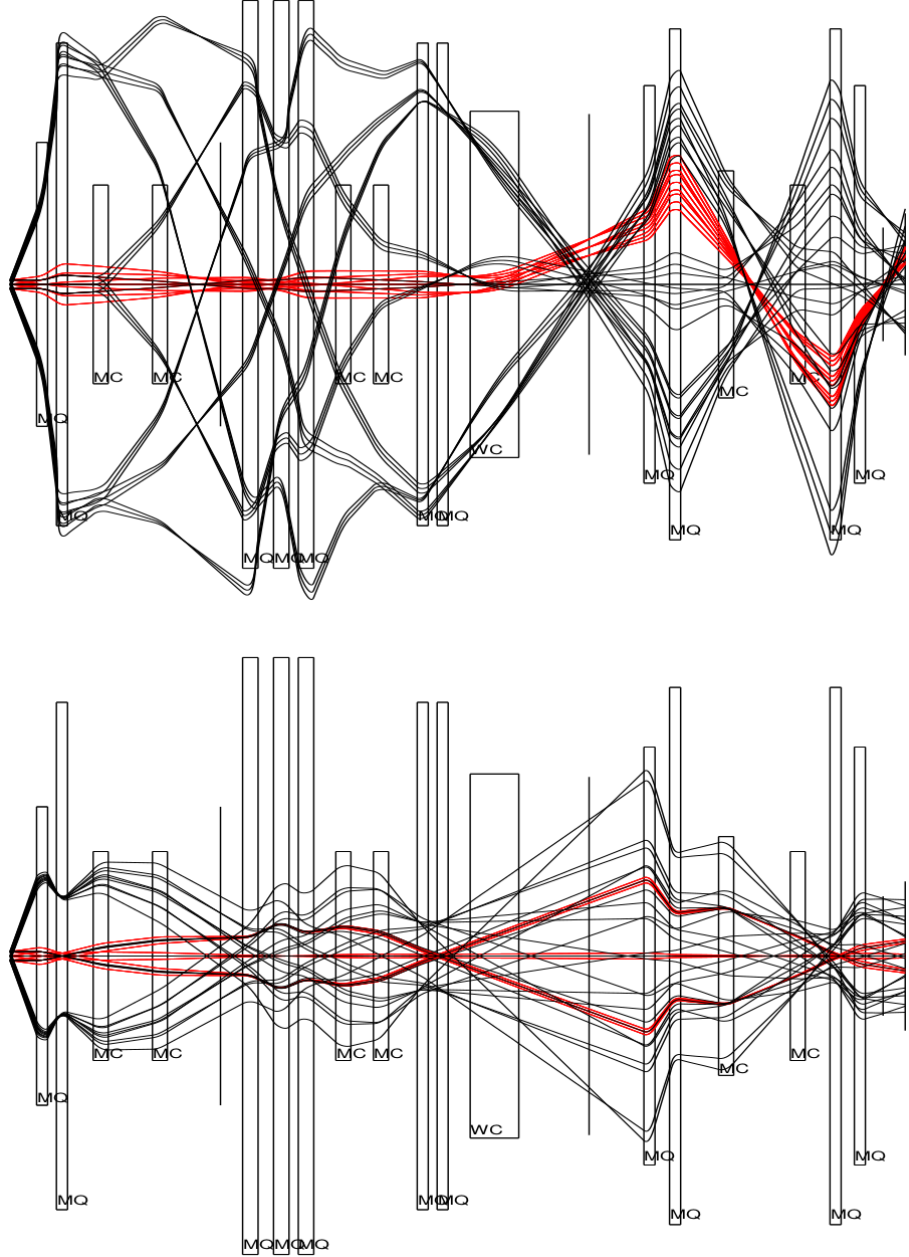


Figure 3.1. Horizontal (upper plot) and vertical (lower plot) rays through St. George. Recoil  $^{41}\text{Sc}$  rays are shown in black and beam  $^{40}\text{Ca}$  rays are shown in red. The beam rigidities are  $B\rho = 0.331 \text{ Tm}$  and  $E\rho = 2.907 \text{ MV}$ , and the recoil rigidities are  $B\rho = 0.331 \text{ Tm}$  and  $E\rho = 2.836 \text{ MV}$ . Both the beam and recoil are in the  $11^+$  charge state. Differing charge states would lead to a greater separation in the two beam profiles. The COSY calculation assumes that the recoil particles are spread within an acceptance range of  $\Delta E/E \approx 7.5\%$  and  $\Delta\theta = 40 \text{ mrad}$ . The transverse scale is highly exaggerated to show detail.

The initial ion optics solution creates a transport map for particles passing through the entire separator that can be analyzed independently of the ray traces and provide the mathematical backing to the particles' trajectories within St. George. The transport map is dependent on the quantities

$$\begin{aligned}
r_1 &= x & r_2 &= a = p_x/p_0 \\
r_3 &= y & r_4 &= b = p_y/p_0 \\
r_5 &= l = -(t - t_0)v_0\gamma/(1 + \gamma) & r_6 &= \delta_K = (K - K_0)/K_0 \\
r_7 &= \delta_m = (m - m_0)/m_0 & r_8 &= \delta_z = (z - z_0)/z_0,
\end{aligned} \tag{3.1}$$

where  $a$  and  $b$  are treated similarly to angles as a first approximation within each plane,  $\delta_K$  is the relative energy difference from the desired energy  $K_0$ ,  $\delta_m$  is the relative mass difference from the desired mass  $m_0$ , and  $\delta_z$  is the relative charge from the desired charge state  $z_0$  [28]. These values are related to the parameters in the transport map (see Sec. 1.3.2), but defined for use within the code. The desired quantities are the values used to calculate the magnetic (Eq. 1.2) and electric (Eq. 1.3) rigidity, and thus set the fields of the elements within St. George, of the particle to be transported through the entirety of the separator. The time of flight difference  $l$  is not considered in analyzing the separator. Within the transport map, aberrations up to fourth order were calculated, with terms up to third order found to affect the design [15].

The original ion optics calculation describes the fringe fields of the optical elements using the default parameters provided by COSY. A change in the shape of the fringe field can change the trajectory of the particles within the separator, as the total field that the particle interacts with changes in magnitude. Since the fringe fields used to find the ion optics solution and those created by the actual magnetic elements within St. George may be different, the required field strength may also be different.

Field maps for each of the magnetic elements were measured by the production company in order to understand the dependence of the field strength and fringe fields at differing excitations of the magnet. The pole tip fields for a given particle rigidity, determined by the current set point for that magnet, must be found experimentally. The procedures for each of the three different types of elements necessarily differ based on what diagnostic equipment is available.

The magnetic settings for the dipole magnets, determined by the rigidity of the particles, can be determined by observing the trajectory of the particles within the separator. This trajectory can be directly observed using diagnostic equipment aligned with the optical axis. The final setting of the dipole magnets must be found by observing the effect of the focusing quadrupole magnets following the dipole. If the beam is aligned with the magnetic optical axis of the quadrupoles, the off-axis steering effects will be minimized. This fine adjustment to the dipole fields is within a small window of current settings for the dipole near the coarse value found through direct observation of the beam.

Setting the Wien filter can be done in a similar manner. The electric field strength is determined from the known energy of the particle, the known charge state, and the desired bending radius of the filter. This bending radius is the radius of the particle's trajectory if only the electric or magnetic field were operating. Thus, the electric field strength can be set to an exact value, requiring the magnetic field to be set to match the properties of the electric field. The strength of the magnetic field is set such that the bending radii of the two fields are the same and so that the particle beam continues along the optical axis in the same manner as described previously with the standard dipoles. The Wien filter was designed with magnetic field clamps at the entrance and exit of the filter to match the magnetic fringe field to the electric fringe field. These clamps must be adjusted to their proper positions before the magnetic field can be set.

The magnetic quadrupoles require a more complex procedure in order to set their fields to the desired values. This complication arises from the inability to directly observe the trajectory of the focused particles within the separator at all possible angles and energies concurrently, and at multiple points within the separator itself. If these trajectories match the trajectories expected from the beam optics calculation, then the acceptance and rejection properties of the separator would be the desired values. Due to the inability to do this, the quadrupole tuning procedure must be adapted to work with the diagnostic equipment available. The full procedure is outlined in 3.3.1.2.

### 3.2 Separator Properties

The elements, power supplies, and supports were provided by Bruker Biospin and installed in 2011. The separator design requirements for the strengths of the optical elements were based on the maximum beam energy of the older KN single-ended Van de Graaff accelerator and the possible charge states produced by its internal ion source. The 5U and ion source have similar properties to this system. The power supplies for the magnets provide highly stable direct currents for each magnet individually, with  $dI/I \approx 10^{-4}$  for the quadrupoles and  $dI/I \approx 10^{-5}$  for the dipoles. The upper current limit is different for each magnet. The separator uses a robust water cooling system able to maintain the required  $80 \pm 2$  °F magnet temperature for the entire system. The system is able to maintain the temperature even when all magnets are at their maximum currents for extended periods of time.

The Wien filter electrode power supplies are set separately based on their voltage, with voltage stability  $dV/V \approx 10^{-5}$  in the range commonly used for experiments. The upper limits for these power supplies are  $\pm 110$  kV, with voltages below  $\approx 70$  kV used during previous work. In order to reach electric potentials near the top of the range, the voltages need to be slowly ramped up to “condition” the plates at the higher

voltage. This conditioning is required due to minor imperfections on the surface of the electrostatic plates, differences in the residual vacuum within the vacuum chamber, and buildup of C deposits on the plates and interior walls. Directly setting the plates to higher voltages without conditioning the plates would lead to large and frequent discharges of the electrostatic plates, preventing the Wien filter from being used in stable running conditions. For voltages above  $\approx 50$  kV, the plates were conditioned at settings at least 10 kV above the desired set point to provide a stable running condition. For lower potentials, no conditioning is necessary unless the vacuum chamber was recently vented (exposed to atmospheric pressure gases).

The properties of each of the electromagnetic elements (entrance and exit apertures, length, maximum field strength, good field region, etc.) were determined within the ion optics solution to transport the desired recoils, and built to match those specifications. Higher order corrections to the particle trajectory were achieved by shaping the entrance and exit faces of the dipoles instead of using higher order multipole magnets [15]. Additionally, the shape of the Wien filter electrostatic plates were designed such that the electric and magnetic fields, including the fringe fields, were closely matched.

### 3.2.1 Magnetic Fringe Fields and Effective Field Lengths

Detailed two-dimensional magnetic field maps for multiple excitations of each magnet were provided by Bruker. The field maps allow a check on the good field region for each magnet and provide a description of the fringe fields. Field strengths at each location (distance along the beam axis and at a radial distance from the beam axis) are measured in mT. From this data, the shape of the fringe field and the effective field length of the magnetic elements can be determined. The effective field length, defined as

$$L = \frac{1}{B_0} \int_{-\infty}^{\infty} B(z) dz, \quad (3.2)$$

where  $B_0$  is the field strength at the center of the magnet,  $L$  is the field length if the field were described with a pure “hard edge” or Heaviside function at the entrance and exit, i.e. no fringe fields. As these values are essential to setting the necessary values for the quadrupoles, the analysis of the field maps focused on these elements.

A single edge fringe field is described by the Enge function given by

$$E(z) \equiv \frac{1}{1 + \exp \left[ \sum_{i=0}^{N-1} a_i \left( \frac{-z}{D} \right)^i \right]}, \quad (3.3)$$

where  $a_i$  are the desired expansion coefficients,  $D$  is the aperture diameter, and  $z$  is the longitudinal distance [5]. The formulation above is used within COSY to describe user-defined fringe fields. For a short magnet, which the St. George quadrupoles can be considered to be, the entrance and exit fringe fields are not completely independent of each other, since the fringe fields extend into the central region of the magnet. Instead of fitting each fringe field separately, we can instead fit the entirety of the magnetic field profile using a combined “short” quadrupole function, in terms of the Enge function, given by

$$k(z) = k_0 [E(L/2 + z) + E(L/2 - z) - 1], \quad (3.4)$$

where  $k_0$  is a scaling parameter for the central field and  $L$  is the effective field length [5]. This formulation assumes a symmetric field profile, as both the entrance and exit fringe fields are modeled with the same Enge function.

Using the field maps provided by Bruker, we can determine the Enge coefficients and the effective field lengths for our magnets. For all calculations, since the field near the center of the magnet is relatively weak, the fields within 2 cm in the radial direction of the central axis were not used for determining either the effective field length or the Enge coefficients. Additionally, the effective field length and the shape

of the fringe field were assumed to not differ with different magnet excitations, so all available data were used for each magnet at the same time. An example using the penultimate quadrupole  $Q_{10}$  of the normalized fields used and the resulting fit is shown in Fig. 3.2.

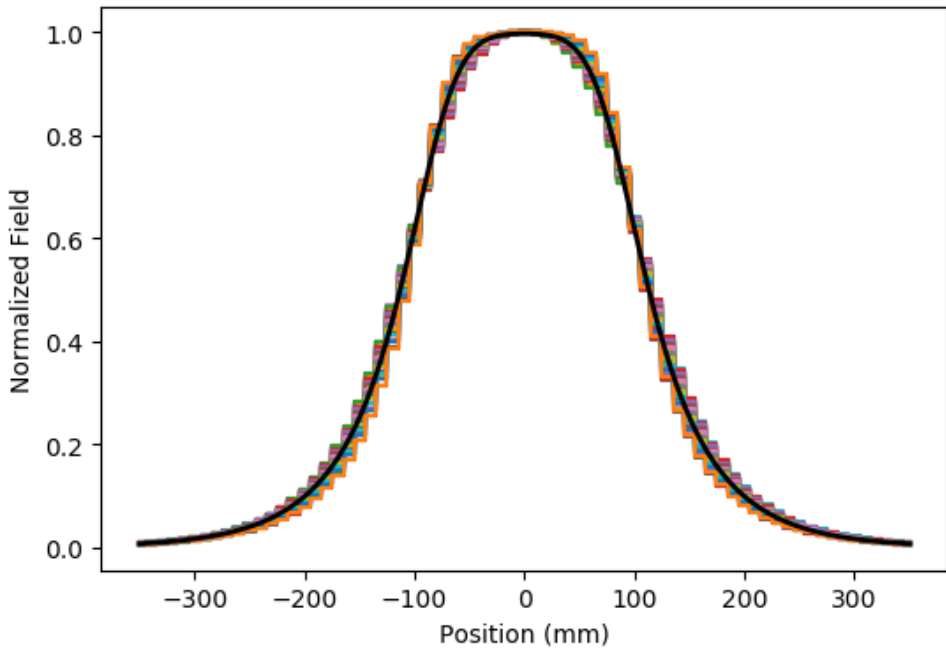


Figure 3.2. Normalized field and the resultant fit to the fringe field for the example quadrupole  $Q_{10}$ . The parameters of the fit are given in Table D.1.

The effective field lengths were calculated directly from the field maps by integrating along the  $z$ -direction for each radial distance provided. Since the maximum field strength for a given magnet current varies depending on the distance from the center, the individual “traces” of the magnetic field along the  $z$ -axis were normalized. This normalization is shown in Eq. 3.2 as the constant factor outside of the integral. The

integration was performed using the Simpson’s Rule routine provided by the SciPy Python package [24]. An average of these lengths was used. Differences between the calculated effective field length and those used within the initial ion optics solution were within 2 %.

Using the same normalized field “traces” along the  $z$ -axis, the Enge coefficients describing the shape of the fringe field may be determined. The field profiles at each radial distance were fit simultaneously. Using the default Enge coefficients as the initial parameter guesses, the summed mean squared error between the data and Eq. 3.4 was minimized using the Nelder-Mead downhill simplex minimization (see [33]) provided by SciPy [24]. The process was repeated for each quadrupole separately. The difference in the shape of the fringe field can be seen in Fig. 3.3.

In some cases, the field maps were not recorded far enough away from the center of the magnet for the fitting routine to converge, primarily due to the field not adequately reaching zero. In those cases, “dummy” points of zero field were pre- and post-pended to the individual “traces” at distances greater than 5 m from the center of the magnet to aide in convergence.

The default COSY coefficients for the fringe field were compared against the data and shown to not adequately describe the field maps. The summed mean squared error when using the short quadrupole formalization and the default COSY parameters was significantly larger than that found through the minimization routine, and the difference was shown to be statistically significant. A visual comparison between the two models for  $Q_{10}$  is shown in Fig. 3.3.

These new terms describing the effective field length and the fringe field can be used to provide a more realistic beam optics solution for St. George. Within the COSY description of the separator, the magnetic fields for the quadrupoles were defined with the updated fringe field parameters. The beam optics solution was refit by minimizing a cost function defined in terms of our desired transfer matrix

properties at our focal planes, such as the mass and energy dispersion at the post-Wien filter focal plane  $F_2$ , the beam spot size at the final detector plane  $F_3$ , and other properties. From this recalculated solution, new pole tip fields for the focusing quadrupoles are determined which can provide a more accurate estimate of the actual experimental field required for the experiment.

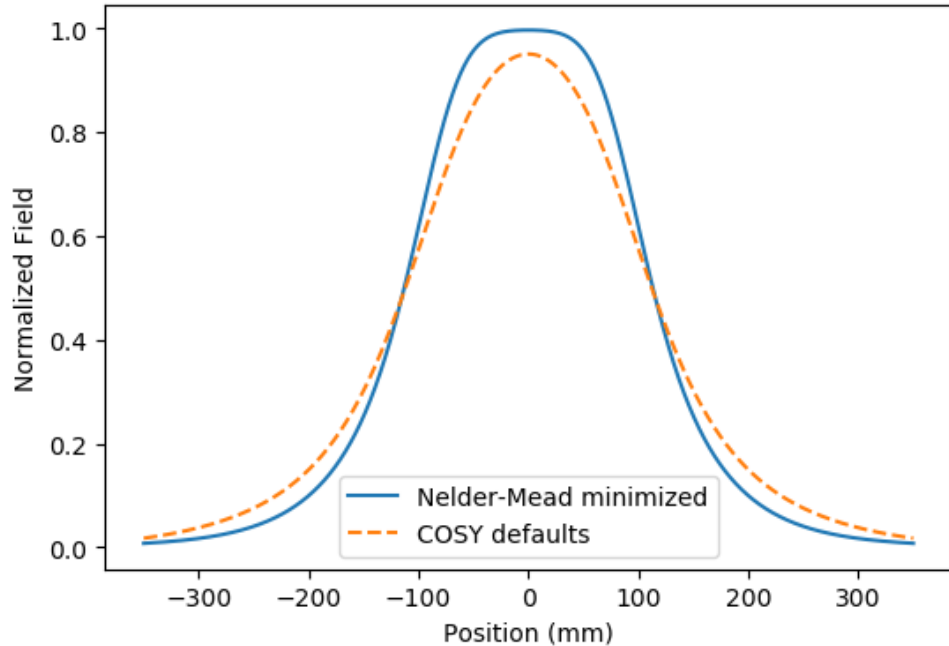


Figure 3.3. Comparison between fringe fields for the example quadrupole  $Q_{10}$ . The COSY default parameterization for the fringe field is the dashed orange line, and the fitted fringe field is the solid blue line. Due to the different parameters used for the fringe field, the shape is qualitatively different, which will affect the actual setting of the magnetic element. Refitting the magnetic field in St. George within the COSY program can be used to guide this procedure.

### 3.3 Energy and Angular Acceptance

The energy and angular acceptances of St. George were determined experimentally through a series of experimental campaigns using multiple rigidities. The energy acceptance without a corresponding angular acceptance was shown to exceed the designed acceptance at zero degrees, with a measured energy acceptance of  $\Delta E/E = \pm 8\%$  for ten different beam rigidities covering the phase space region for recoils created by reactions of astrophysical importance [31]. The angular acceptance has been shown to meet the desired  $\Delta\theta = \pm 40$  mrad in limited cases with an energy spread of  $\Delta E/E = \pm 3\%$ . The full total acceptance where the angle and energy are allowed to deviate up to their maximum design limits has not yet been measured for the entirety of St. George, with work ongoing.

Within the following discussion, the term “test beam” will be used in reference to an incident beam produced by the 5U with a desired rigidity. These test beams are defined by the selected beam particle, energy, and charge state, which determines the magnetic and electric rigidity. Test beams with different rigidities were chosen to adequately cover the possible rigidity phase space during the commissioning experiments (see Fig. 3.4). These beams were chosen to provide particles with the desired rigidity and with beam currents in the range of  $0.5 - 3 \mu\text{A}$  in order for the diagnostic equipment to properly measure the beam. Additionally, those beams that commonly had highly stable 5U and ion source running conditions over extended times were selected to reduce beam preparation steps.

Acceptance measurements first probed the energy acceptance within the designed  $B\rho - E\rho$  phase space. The rigidity phase space limits, along with measured acceptances and ranges for proposed future experiments is shown in Figure 3.4. The regions of astrophysical interest are accessible by various test beams that can be produced by the 5U, allowing the phase space to be adequately studied.

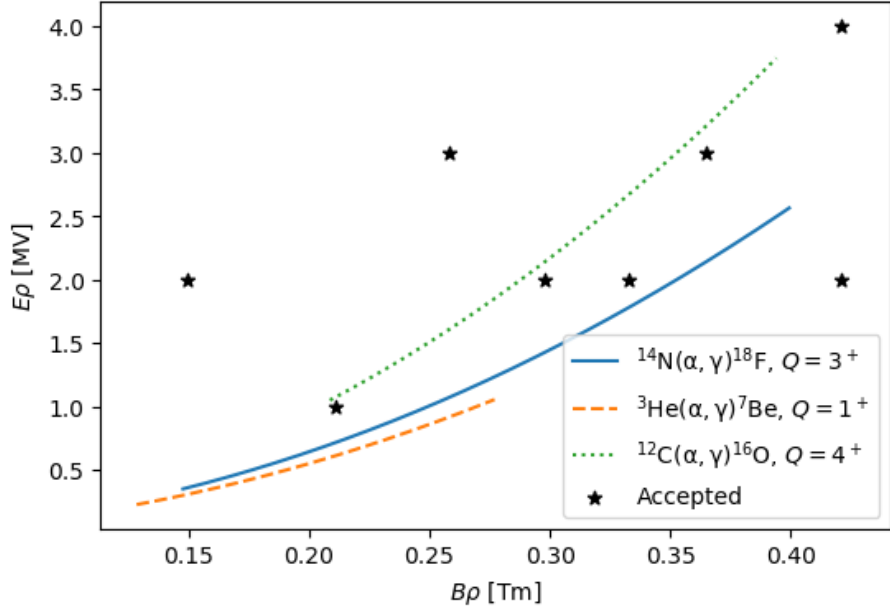


Figure 3.4. Designed  $B\rho - E\rho$  rigidity phase space for St. George. Stars represent rigidities that have been shown to have the full  $\Delta E/E = 8\%$  energy acceptance. Reactions shown are probable first experiments using St. George that use beam energies accessible with the 5U:  $^{14}\text{N}$  at  $E_{\text{beam}} \approx 0.7 - 5.0$  MeV (solid blue line),  $^3\text{He}$  at  $E_{\text{beam}} \approx 0.25 - 1.2$  MeV (dashed orange line), and  $^{12}\text{C}$  at  $E_{\text{beam}} \approx 3.0 - 10.0$  MeV (dotted green line). These energy ranges cover some of the astrophysically important ranges for the given reactions. Adapted from [31].

### 3.3.1 Beam Tuning and Properties

The commissioning runs followed a similar procedure for beam preparation using the 5U and the transport line. The beam rigidities were chosen to cover a region within the phase space limits of the separator that cover recoils produced through reactions of astrophysical interest. Both light ( $^1\text{H}$  and  $^4\text{He}$ ) and heavier ( $^{16}\text{O}$  and  $^{20}\text{Ne}$ ) beams were used to probe different regions of that phase space. Angular acceptance runs to date have only used lighter beams. The energy uncertainty of the beam is approximately 0.3 keV, and a conservative value of 0.5 keV will be used to account for the lack of a direct measurement with the exact experimental setup used herein.

Beam preparation can be divided into two segments: preparing the incident test beam with no energy difference and no angular difference ( $\Delta E = 0\%$  and  $\Delta\theta = 0$  mrad) to enter into St. George along the central magnetic optical axis, and transporting that beam along the central magnetic optical axis within St. George. The following procedures were used for all acceptance measurements, with differences being minor. The diagnostic equipment described in Section 2.2.2 was essential to performing the beam preparation steps and their use is highlighted below.

### 3.3.1.1 Before St. George

Test beam preparation before St. George is required to prepare the beam for the experimental requirements of the commissioning runs: the beam

1. must enter along the magnetic optical axis;
2. must have a narrow waist point with a circular cross section at the target location;
3. must have a focus that is not highly divergent; and
4. must be stable with low energy uncertainty and relatively high current.

These requirements are fulfilled through the operation of both the 5U and the transport beam line, with the last two requirements primarily beneficial from an experimental standpoint. The beam divergence is the maximum angle of the particle trajectory caused by the focusing elements along the transport line, and is related to the magnetic fields used to focus the beam and the properties of the beam, such as beam extent and rigidity. A graphical description of these dependencies is shown in Fig. 3.5.

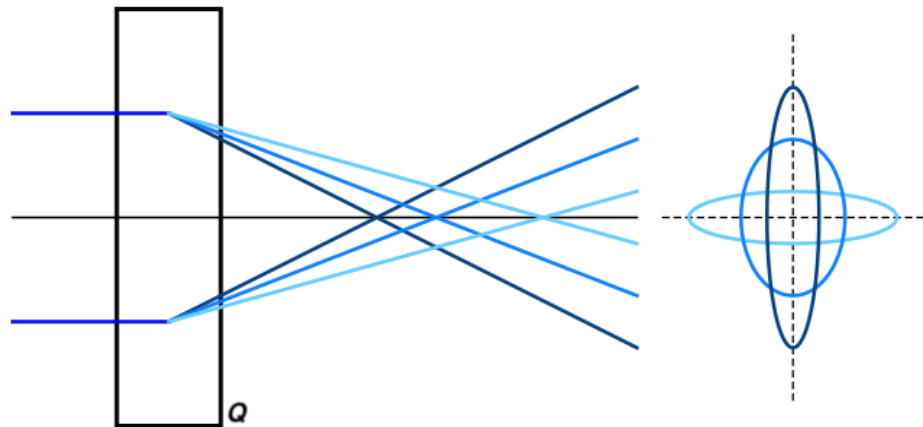


Figure 3.5. Sketch of the beam divergence caused by the focusing strength of a quadrupole magnet. Increasing darkness corresponds to increasing strength of the magnetic field. When focusing in a single direction, the apparent beam spot (shown on the right) must diverge in the other direction. The requirements of the tune will determine what beam shape some distance from the quadrupole is required.

The chosen beam intensity is dependent on which diagnostic equipment will be used. The isolated Faraday cups cannot read current below 50  $e\text{nA}$  when read through the logarithmic amplifier at the console, and the current can't be above 20-30  $e\mu\text{A}$  as the cups are not currently water cooled and a high intensity and focused beam may melt some of the components. This upper current limit was not approached during the tests, since the cups were used in tandem with the quartz viewers. The quartz viewers are limited to beam currents of a maximum of 3-5  $e\mu\text{A}$ , as higher currents risk heating up the quartz to a high enough temperature to cause them to shatter or melt. Since four of the quartzes are also barriers between the high ( $10^{-8}$  torr) vacuum within St. George and atmosphere, this limit must be carefully avoided. In practice, currents between 500 nA and 4  $\mu\text{A}$  were used, based on the exact properties of the ion source for that particular run, the beam species, and the locations of slits on the primary transport line used to reduce the beam current.

The procedure for aligning the test beam to the magnetic optical axis is described

below. Major subsections of the procedure will begin with a short title in bold to guide the reader. The elements on the main transport line that may be necessary to adjust are the switching magnet with the  $X_6$  steerer, and the  $Y_5$  and  $Y_6$  steerers (locations shown in Figure 2.1). The steerers are labeled as such based on their position along the main transport line. Steerers  $X_6$  and  $Y_6$  are part of the same physical steerer but can be operated independently. Additionally, the quadrupole triplet directly before the target location will be necessary for final tuning.

**Aligning the beam to St. George's optical axis:** The desired test beam is transported down the St. George transport line and monitored with the Faraday cup at the target location, called the *target cup* for beam current stability. Diagnostic equipment before the target location are used as an aide to transport the beam and ensure that it has the desired properties. If necessary, the beam current is reduced. The quadrupole triplet is not used at this point, since the beam may not be entering the element along its magnetic optical axis.

The beam is sent into St. George. With no field in  $Q_1$ ,  $Q_2$ , and  $B_1$ , the beam hits the quartz viewer at the  $0^\circ$  exit port of the magnetic vacuum chamber, called the  *$B_1$  quartz*. If the beam does not strike the quartz, then the final set of steering elements needs to be adjusted to send the beam into the quartz.

**Checking for steering:** Quadrupoles  $Q_1$  and  $Q_2$  are adjusted independently of each other, and the resulting motion of the beam on the quartz is recorded. If the beam is aligned with the central magnetic optical axis, the quadrupole will only focus the beam and not shift its position on the quartz, i.e. the spread in the beam will change but not its central position. The two quadrupoles must be adjusted independently of each other as any induced steering from a beam misalignment in one may be counteracted by a misalignment in the other quadrupole. If the beam is steered by either quadrupole, the steering elements preceding the offending quadrupole are adjusted to reduce that steering. Commonly, the elements that steer in the same di-

rection as the focusing direction of the quadrupole (i.e.  $Y_5$  and  $Y_6$  for  $Q_1$ , the switching magnet and  $X_6$  for  $Q_2$ ) will provide the largest improvement to the steering. Minor corrections to all preceding steering elements may be required as the non-steering solution is approached.

A quadrupole steers a beam when the beam enters the magnetic element misaligned with the optical magnetic axis. Assuming that the element is brought from zero to defined strength, the focal length of the quadrupole changes from  $\infty$  to a length  $f$ . The effect on the beam is that those regions of the beam away from the optical axis are brought to pass through this focal point. When a beam is aligned with the magnetic optical axis, there is an equal amount of the beam on either side of this optical axis, so the beam spot will narrow along the focusing axis of the quadrupole. The beam will also extend along the other axis. If the beam is not aligned with the optical axis, this beam motion to the focal point will be viewed as a lateral motion along the focusing axis of the quadrupole. A sketch of this effect can be seen in Figure 3.6.

The goal for adjusting the steering elements before St. George is to have each quadrupole induce no steering on the beam. In practice, each change to the steering elements either increases or decreases the amount of steering in the direction of that element. The crossover point, where the beam switches from steering left to steering right for example, can be used to restrict the possible phase space of steerer values, as the beam must have a zero deflection position between those two extremes.

A single quadrupole may induce steering in both directions based on the beam conditions. For example, a beam that is misaligned in both the  $+x$  and  $+y$  direction entering into a quadrupole focusing in the  $y$  plane will be steered in both the  $+x$  and  $-y$  direction. When minimizing steering in a single direction, the other direction must be periodically checked to ensure that a minimal steering solution is reached for both directions at the same time. At the end of this process, the beam is not deflected

when the field strength for either  $Q_1$  or  $Q_2$  is increased or decreased independently of the other quadrupole. The beam may be said to be entering St. George along the optical magnetic axis. Due to the short distance between the first quadrupole doublet and the  $B_1$  quartz, it may be necessary to increase the sensitivity of the steering to ensure that we are as aligned as possible to the axis.

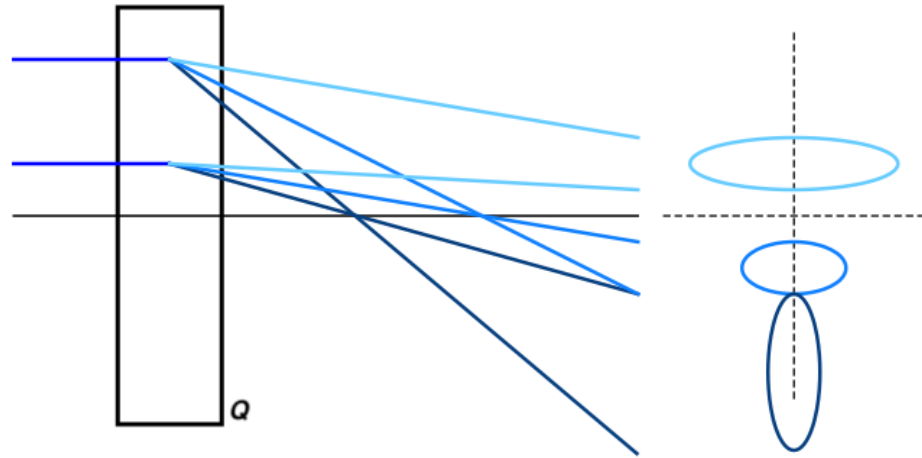


Figure 3.6. Sketch of the steering caused by a quadrupole magnet due to the beam being misaligned to the magnetic optical axis. Increasing darkness corresponds to increasing magnetic field strength. From the misalignment, the beam spot appears to move along the focusing axis at some distance. The scanning motion of the spot can be used as a diagnostic tool to determine the beam alignment. If the beam spot is not moving in the focus direction as the magnetic strength is changed, the beam is aligned to that quadrupole's magnetic axis.

**Increase sensitivity:** The beam is then sent further into St. George, first to the  $B_2$  quartz located within the beamline then the  $B_3$  quartz. The steering of  $Q_1Q_2$  is again checked in the same fashion as before. As these quartzes are located further from the quadrupoles, they give a higher sensitivity to steering effects from

misalignment than just using the  $B_1$  quartz at the trade-off that the the quadrupoles can only be set to lower field strengths. Since the quartz is further from the focusing elements, the same focusing strength will create a larger beam spot on the quartz viewer. This effect can be seen in Figure 3.6.

These additional checks require  $B_1B_2$  to have field. While these two dipoles must have an exact field strength when performing acceptance measurements or an experiment, at this point their fields only need to be coarsely set such that the beam strikes the desired quartz. While the higher order corrections from these magnets do play a role in the direction and focusing of the beam, that contribution has no effect on determining beam alignment within the quadrupoles.

The steering elements are adjusted in the same fashion to minimize steering in  $Q_1Q_2$ . Since this steering was minimized during the previous step, these adjustments should be minimal. It may be necessary to have a weak field in  $B_3$  in order to see the beam on the  $B_3$  quartz, due to possible machining misalignments of the port that the quartz is attached to and the residual magnetic field within the dipole.

**Include the quadrupole triplet:** As the last focusing element before St. George, the quadrupole triplet (henceforth simply the *triplet*) is the final adjustable element to determine the beam properties when entering the separator. The triplet is used to focus the beam to a small spot at the target location, a requirement for both experiments and acceptance measurements. As it and  $Q_1Q_2$  should lie on the same magnetic optical axis, its steering must also be checked and minimized if its use is desired for the present experiment. It was not used in all cases as the coarse target focus provided by the previous quadrupole doublets on the main transport line were deemed sufficient.

Before moving the beam off of the  $B_1$  quartz, the steering effects of the triplet must be characterized in the same fashion as  $Q_1Q_2$ . During the steering minimization steps, both the triplet and  $Q_1Q_2$  must both be minimally steering before moving

forward.

Due to minor misalignments between the triplet and  $Q_1Q_2$ , it is usually not possible to have all elements non-steering at the same time. In these cases, the steering of  $Q_1Q_2$  should take precedence while having the triplet minimally steering. While the steering of the beam prior to the target location is important, experimentally the steering of the individual elements within the triplet cancel or nearly cancel each other out when the triplet is minimally steering, reducing that problem.

At this point, the main transport line has been tuned to prepare a well-focused and well-aligned beam entering into St. George. These elements are not to be touched during the rest of the tuning process. The triplet, due to the possibility of it having minor steering effects, must also have zero field for the remainder of the steering checks, and will be turned on for the actual measurement.

### 3.3.1.2 Within St. George

Once the test beam has been aligned to enter the separator along the magnetic optical axis, it must also be aligned to the magnetic optical axes of all of the quadrupoles within the separator. This alignment is done using only the dipoles  $B_{1-6}$  and the WF. Any minor misalignment in the vertical direction should have been corrected during the previous steps, but there is the possibility that there will be vertical steering within the separator, both from that misalignment and effects from the dipoles and quadrupoles. The procedure for this second alignment is straightforward, as the only elements used to adjust the steering of the quadrupoles are the two dipoles immediately prior.

**Tuning to the Wien Filter:** With the beam striking the  $B_3$  quartz, quadrupoles  $Q_{3-5}$  are checked for steering. The primary focus of these steering checks will be on  $Q_3$  and  $Q_5$  which focus in the horizontal plane. The magnetic fields within  $B_1B_2$  are adjusted to make these quadrupoles non-steering or minimally steering. The field

precision is on the order of 0.1 G, read back by the Hall probes.

Due to potentially small misalignments in the St. George quadrupoles in relation to each other, it is commonly not possible to have  $Q_{1-5}$  non-steering simultaneously (see [31]). In these cases, minimal steering can be achieved through  $Q_{3-5}$  by adjusting  $B_1B_2$  when  $Q_1Q_2$  are non-steering. At this point, dipoles  $B_1B_2$  are set to the value corresponding to the magnetic rigidity of the particle and to maintain the test beam alignment to the optical axis.

Dipoles  $B_3B_4$  are brought up to their rough field value to send the beam through the WF and onto either the WF quartz or the  $B_5$  quartz. The quadrupoles  $Q_{6-9}$  are checked for steering, adjusting  $B_3B_4$  to minimize the steering. The focus at this point is on getting a non-steering solution for  $Q_6Q_7$ , as  $Q_8Q_9$  can also be corrected by the Wien filter. Since there is some residual magnetic field within the Wien filter, the electric field is brought up to compensate for this bending to keep the test beam along the optical axis through  $Q_8Q_9$ . The field required is calculated by determining the bending radius caused by the residual magnetic field and creating the equivalent bending radius in the opposite direction for the particle's  $E\rho$ .

As the beam envelope has expanded, it will be necessary to bring  $Q_{1-5}$  to their desired values in order to check the steering of the remaining quadrupoles. Since these quadrupoles have been shown to be minimally steering, their effect on the beam trajectory through the remainder of St. George should be negligible. It may be necessary to have a weak field in  $B_5$  in order to see the beam on the  $B_5$  quartz for the same reasons as explained previously for  $B_3$ .

**Setting the Wien Filter:** For the incident test beam's rigidity, the properties of the beam, such as the energy and charge state, are well known or exactly known. Thus, the electric rigidity  $E\rho$  is also well known when tuning for a set bending radius. For St. George, the Wien filter (WF) bending radius is  $\rho_{\text{WF}} = 4.348$  m. The electric dipole within the WF is set for this rigidity and held constant for the remainder of

the tuning process.

The magnetic field is set similarly to the other dipoles: to minimize the steering induced by the next set of quadrupoles ( $Q_8Q_9$ ). Since the test beam was aligned to the optical magnetic axes of this quadrupole doublet in the previous step, the WF magnetic dipole must return the beam to this orientation. The preceding magnetic quadrupoles  $Q_{1-7}$  must also be set to their required values. These values are found by scaling the calculated tune based on the rigidity of the test beam; in cases where an optimal solution was found experimentally that differs from the COSY calculated values, those *in situ* optimized values are used as the baseline. The quadrupoles are required to be set since the elements within St. George up to and including the Wien filter work to separate the beam particles by mass, so setting them mimics the situation during an experiment.

The magnetic field for the WF is read back using a Hall probe located on the pole face. The field can be set precisely and related to the fields in the other dipoles. Once the magnetic field is set such that  $Q_8Q_9$  do not steer the beam, the full WF is set.

**Tuning through the detector chamber:** Dipoles  $B_5B_6$  are set to their rough values based on the  $B\rho$  of the test beam, sending the beam through the detector chamber and onto the last quartz, called the *detector quartz*. As before, due to the size and shape of the beam envelope,  $Q_8Q_9$  must be set to the required values. The final two quadrupoles  $Q_{10}Q_{11}$  are checked for steering, and  $B_5B_6$  are adjusted to minimize that steering.

Since the test beam is traveling through the detector chamber, the entire detection system must be pulled out of the way of the beam. Magnetic shields have been placed below the MCP constructs to remove the effect of the magnetic fringe fields on the beam deflection [32]. Once  $Q_{10}Q_{11}$  are non-steering, the test beam is fully aligned to the optical magnetic axis of St. George.

### 3.3.1.3 Collimator and Target Position

The 2 mm diameter collimator at the target location (see Section 2.4) is used for setting the triplet to the proper values. A narrow waist beam at the target location is a requirement to achieve the maximum angular and energy acceptance for St. George. With the collimator in place, the triplet is adjusted such that the beam transmission, defined as the ratio between the beam currents before and after the collimator as read by two separate Faraday cups, is maximized and ideally close to 100 %.

Since the target chamber may rotate around its central axis, it is possible for the location of the collimator to become slightly misaligned between runs. Additionally, the triplet may induce some minor steering at the target location, potentially moving the focal point radially from the optical magnetic axis. The target collimator position is then not a fixed value but must also be tuned to maximize transmission. Once the collimator position is found, the target position is immediately known. Empirically, a small range of possible values for the rotation and extension of the target ladder have been found to be optimal, restricting the search space when tuning.

For acceptance measurements, the collimator is used to create an object point at the target location. Once the beam preparation is complete, it is retracted from the beamline. In situations where a target foil is used as a “degrader” to provide an angular and energy spread, the relative distance between the collimator and the foil is used to properly align the foil to the beam.

### 3.3.1.4 Additional Considerations

The steering minimization routine can never fully eliminate the beam steering because of possible misalignments of the magnetic elements and the properties of the beam. Especially of concern would be the vertical steering of the  $y$ -focusing quadrupoles ( $Q_{1,4,7,8,11}$ ), as the alignment of the beam to their axis is primarily affected by the beam preparation steps before the beam enters St. George. These

quadrupoles may steer in the vertical direction despite the best efforts of the operator. As there are no elements within St. George that could correct for this, the steering effect of these quadrupoles may not be able to be eliminated.

As the process is repeated, the required field strengths for the magnetic dipoles within St. George will be better known, and additional global settings for St. George will be iteratively updated to provide a better starting point for minimization. Over time, the magnetic field strengths will be known with enough accuracy across a range of rigidity values that a simple scaling to the selected beam energy can provide the final set points for the magnets without much further tuning.

### 3.3.2 Energy Acceptance

The energy acceptance of St. George at  $\Delta\theta = 0$  mrad was measured to be  $\Delta E/E = \pm 8\%$  for ten different rigidities (see Fig. 3.4 and [31]). The measurements took place before angular acceptance target chamber was built and will be remeasured as part of a total acceptance measurement campaign. Test beam rigidities were chosen to cover an adequate region within the designed phase space near the rigidities expected for recoils of astrophysical interest and based on the restrictions imposed by the 5U and ion source.

For a given set of field settings for a test beam at  $\Delta E = 0$  that provide 100 % transmission between the target cup and a Faraday cup located within the detector chamber at focal plane  $F_3$ , the separator is said to accept an energy difference if the test beam is changed to that different energy and still have 100 % transmission between those two cups. To state that St. George has an energy acceptance of  $\Delta E/E = \pm 8\%$ , a single set of fields for the elements within the separator transmitted 100 % of the test beam between the two cups when its energy was changed within that energy change.

The procedure for measuring the energy acceptance of a single rigidity is outlined

below. The slits located at the post-WF focal plane  $F_2$  were used to define a beam center. As the tune for a given recoil is supposed to be achromatic at this location, these slits were used as both a diagnostic on the path of the beam and a check of this requirement during the measurements. Note that the tuning process for these measurements did not make use of the in-beam quartz viewers at  $F_1$  and  $F_2$  since they had not yet been installed.

**Initial setup:** After tuning a beam along the optical magnetic axis as described in 3.3.1, all elements within St. George are at a given field. The dipole elements, including the WF, are not touched. The transmission between the target cup and the  $F_3$  cup is measured. If the transmission is 100 %, the beam energy was changed. If not, then the quadrupoles were retuned to transmit 100 % of the test beam between the two cups.

Quadrupole retuning was done systematically to prevent over- or under-focusing the beam at any location within St. George. With the beam on the  $F_3$  cup, each quadrupole was adjusted individually to determine what field is required to transmit 100 % of the beam to the cup. After finding that field, the difference is recorded and the quadrupole is returned to its original value. This process is repeated for every quadrupole acting independently. If a single quadrupole could not achieve 100 % transmission on its own, it was not included in the next step. Assuming  $N$  quadrupoles adjusted by  $\Delta B_i$  to give 100 % transmission, the individual quadrupoles  $Q_i$  were changed by  $\Delta B_i/N$ . This approach usually resulted in achieving 100 % transmission for the  $\Delta E = 0$  case.

The quadrupole adjustment described was used at every step if the tune was shown to not transmit 100 % of the test beam. Previous settings of the quadrupoles were recorded to map regions of field strengths where 100 % transmission was achieved for different energy changes.

**Changing energy:** The beam energy was changed to  $E = 0.92 \cdot E_0$  ( $\Delta E/E =$

$-8\%$ ) by changing the accelerator. The transport beamline was scaled automatically to account for the change in rigidity. The beam was shown to enter into St. George along the optical magnetic axis by putting the fields within  $Q_1$ ,  $Q_2$ , and  $B_1$  to zero and checking the steering of the first two quadrupoles. Since this energy change is minor, in most cases only the switching magnet needed to be changed. The magnets  $Q_1 Q_2 B_1$  were brought back to their required values and transmission between the two cups was checked.

If the beam was fully transmitted to the  $F_3$  cup, the settings for St. George were said to have an energy acceptance of  $\Delta E/E = -8\%$ . The beam energy was then changed to  $E = 1.08 \cdot E_0$  ( $\Delta E/E = +8\%$ ), following the same procedure, and transmission was checked. If the beam also was fully transmitted, the separator tune was said to have an energy acceptance of  $\Delta E/E = \pm 8\%$  and the measurement was complete.

Where 100 % transmission was not achieved, the quadrupole scaling described previously was used. The new tune was recorded, and the beam energy was returned to  $\Delta E = 0$  to check transmission. This process was continued until all three energy points had 100 % transmission for a single setting of St. George. During this cycling, referring to previous values was used to prevent correcting the tune in one direction at one energy only to change back to the previous tune at another energy.

Since the  $F_2$  slits were placed around the beam center, achieving 100 % transmission was only possible if test beam had a nearly or completely achromatic focus following the WF, one of the requirements for normal operation of the separator.

**Additional measurements:** For subsequent energy acceptance measurements, instead of using the COSY predicted values, an energy acceptance tune scaled based on the magnetic rigidity  $B\rho$  of the new test beam was used for the initial quadrupole settings. If the difference in  $B\rho$  was sufficiently small, the required adjustments to the quadrupole fields were minimal, speeding up the measurement process. As

more individual energy acceptance measurements were made, the scaling based on  $B\rho$  became more robust to slight differences in beam preparation and species.

Once the ten rigidities within the astrophysically interesting phase space of the separator were measured, work moved to measuring the angular acceptance.

### 3.3.3 Angular Acceptance

As of this writing, the angular acceptance of St. George has been measured to be  $\Delta\theta = \pm 40$  mrad in the horizontal and vertical planes for a single rigidity. The acceptance was shown by ensuring 100 % transmission when deflecting the beam 40 mrad in each direction, and quadrupole adjustments followed the same procedure as during the energy acceptance measurements. The measurement was done without a corresponding energy acceptance, and without the requirement that the test beam be focused at the focal plane  $F_2$  following the WF and without the beam passing through the slit opening at that location for all deflection angles. The measurement was then a single “proof of concept” that an angular acceptance could be measured using the new diagnostic and control equipment installed.

There are multiple solutions to measuring the angular acceptance, both and without an accompanying energy acceptance measurement. Multiple procedures, each with their own tradeoffs and outcomes, were attempted. The final choice of each measurement option will depend on how the measurement will be integrated into the final acceptance measurements and commissioning work. For completeness, the procedures for the options explored are outlined below.

**Deflector plates only:** A test beam is tuned to provide a non-steering beam with 100 % transmission between the target and  $F_3$  cups. The deflector plates (see Section 2.4) are rotated so that they deflect the beam in a single plane. The horizontal plane was commonly chosen first. Since the entrance aperture for the target cup is larger than 40 mrad, it does not intercept any of the beam when it is deflected. Angles

between 0 and 40 mrad were used and the current on the  $F_3$  cup was monitored. The maximum angle that provided 100 % transmission was recorded.

If the maximum angle achieved was not 40 mrad, the quadrupoles were tuned in the same fashion as for the energy acceptance measurement but with the deflector plate set to an angle greater than was accepted such that the beam is still partially captured by the cup. The changes to the quadrupole fields were recorded, and all quadrupoles that could provide 100 % transmission were scaled to new values. The beam was returned to  $\Delta\theta = 0$  to ensure that the new tune still provided 100 % transmission in this case, and the deflection was changed.

A single plane was checked for  $\pm 40$  mrad first before switching to the other plane, and any retuning was done to also transmit 100 % of the beam to the final cup. The deflector was also rotated to check the other plane, and the quadrupoles retuned to provide 100 %. In general, this procedure did not provide 100 % transmission when deflecting a test beam up to 40 mrad in the four cardinal directions. This procedure was used for the single full angular acceptance measurement.

Additionally, since the angular and energy acceptance is dependent on the beam size and shape at focal plane  $F_2$ , the WF quartz was used to aide in tuning  $Q_{1-7}$  to their proper values. The beam should move minimally at this location when deflected up to the maximum 40 mrad in any direction. The beam profile is required to be horizontally narrow for the highest mass separation, requiring the vertical extent to be large. Using this intermediate quartz slightly improved the ability to tune the separator but did not allow for a full angular acceptance measurement to be performed.

**Degrader foil:** The limiting factor in using the deflector plates as the only angular change is that each direction must be looked at independently. Assuming the plates are aligned to deflect in the horizontal direction, only one direction (left or right from the beam's perspective) can be viewed at a time without some manual

adjustment to the deflector plate power supply. The cyclic problem of correcting the beam trajectory only to remove that correction becomes harder to avoid. Since the plates can only deflect along a single plane, the additional unknowns of removing a large angular acceptance along a difference by making changes on the current plane also decreased the possibility of success.

At the target location, Al foils of different thicknesses were placed to degrade the beam, creating a spread in angle and energy at the same time. Foil thicknesses were matched with beam properties to fall within the anticipated  $\Delta E/E = \pm 8\%$  and  $\Delta\theta = \pm 40$  mrad acceptances of St. George. Since the foils also induce an energy loss for the test beam, the separator dipoles needed to be properly scaled down to the correct values after the test beam (without foil in place) was aligned to the magnetic optical axis. The scaling required accurate and precise measurements of the foil thicknesses. Thicknesses ranged from  $100 - 250 \mu\text{g}/\text{cm}^2$ , and  ${}^1\text{H}$  and  ${}^4\text{He}$  test beams in the energy range of  $0.9 - 2.0 \text{ MeV}$  were used.

Using the WF quartz, the test beam was tuned to have the correct phase space properties at  $F_2$ . The degraded test beam is emitted into the separator within a phase space determined by its interaction with the foil, allowing the magnets to be tuned without relying on the slow change between deflection angles and directions and including the minor energy acceptance measurement. Currently, no full angular acceptance measurements have been made past  $F_2$ .

**Reaction Measurement:** Additional measurements have been made of the angular acceptance with an energy acceptance and a nearly achromatic focus at the  $F_2$  focal plane. These measurements were for the altered settings for transporting  $\alpha$  particles from  $(\text{p}, \alpha)$  reactions. The measurements are a different “proof of concept” for the angular acceptance measurements by verifying a  $\Delta\theta = \pm 40$  mrad acceptance with the deflector plates before using a foil to produce the full angular spread. In this case (see Ch. 4), the transported particles are the reaction product  $\alpha$  particles,

verified using a direct test beam of  ${}^4\text{He}^{2+}$ . The transported reactions products within the  $\approx 45$  mrad cone limited by the target Faraday cup were transported to  $F_2$  and detected with the Si detector.

### 3.4 Considerations

Full acceptance measurements require a fine detailed understanding of the operation of St. George. Previous work has provided the initial understanding on providing a large energy acceptance of at least  $\Delta E/E = \pm 8\%$  and angular acceptances near  $\Delta\theta = \pm 40$  mrad. Combined measurements have been limited to a large energy acceptance and small angular acceptance or vice versa. Current work is ongoing on providing an improved understanding of the operation of St. George, particularly in setting the quadrupole fields.

A full commissioning of the separator system requires the gas target, separator, and detection system to be operated in parallel and well-understood. The current status of each of these discrete systems is varied. The Hippo gas target has been tested in a prior configuration, and work has been started to redesign the upper chamber to improve the possibility for monitoring incident beam current and using a  $\gamma$  detector in coincidence with the final detector system. The combined  $E_{\text{TOTAL}}$  vs. TOF detection system has been shown to work for surface sources. Silicon detectors are known to be very robust, and the Si detector and acquisition system has been used for a successful measurement with St. George for  $(p, \alpha)$  measurements. The separator status has been explored earlier in this chapter. Final verification of the separator will be measuring the  ${}^{14}\text{N}(\alpha, \gamma){}^{18}\text{F}$  cross section in inverse kinematics at energies where the cross section is well known.

The target chamber used for the commissioning work and the experimental campaign is different than that which will be used during a fully featured St. George experimental campaign, namely the Hippo supersonic helium gas jet target. Hippo will

be used for  $(\alpha, \gamma)$  experiments following the completion of the commissioning work. The specifics of that gas target are discussed elsewhere (see [25] and [30]). Due to the differences between the commissioning chamber and the design of the gas target, some specifics of beam tuning and preparation (see Sec. 3.3.1) will inevitably change as experimental work transitions between commissioning and reaction research work.

Due to the ongoing nature of the commissioning work and the intricate link between the systems—accelerator, target, separator, and detector—involved, the primary *in situ* test of the complete system will be the cross section measurement of the  $^{27}\text{Al}(\text{p}, \alpha)^{24}\text{Mg}$  reaction near two low-energy resonances. This reaction study will provide an assessment of the angular acceptance of the separator with a small energy acceptance. This reaction was chosen since the properties of the reaction are well-known, allowing for the properties of the separator to be determined with minimal external uncertainty.

## CHAPTER 4

### EXPERIMENTAL PROCEDURE

To support the commissioning work of St. George through using reaction measurements, and to explore the possibility of extending the use cases of the separator beyond  $(\alpha, \gamma)$  reactions, the well-studied  $^{27}\text{Al}(\text{p}, \alpha)^{24}\text{Mg}$  reaction was chosen to be an initial test case. The properties of the reaction can be used to verify the desired properties of the separator under a reaction study, effectively emulating the conditions under which the initially proposed  $(\alpha, \gamma)$  reactions will be performed.

To this end, an experimental campaign to study the  $^{27}\text{Al}(\text{p}, \alpha)^{24}\text{Mg}$  reaction with the St. George recoil separator was undertaken at the NSL. Runs were completed in December 2016 and February 2017, with runs focusing on determining the correct magnetic fields within St. George completed in Fall 2016 and February 2017. The reaction was performed in forward kinematics using a stable H beam provided by the 5U. Two low energy resonances were studied with beam currents in the  $2 - 3 \mu\text{A}$  range in February 2017. The experiment was designed to transport and detect the produced  $\alpha$  particles from the reaction. Studying this reaction provides a test of the angular and energy acceptances of St. George in preparation for studying  $(\alpha, \gamma)$  reactions across a wide range of targets and energies.

The first portion of these runs fall under general St. George commissioning work as discussed in Chapter 3 and will not be repeated here. The second portion of the runs involved characterizing the target and the detector, finalizing the optimal settings for the separator, and performing the experiment. The reaction of interest produces  $\alpha$  particles in the energy range of  $2 - 3 \text{ MeV}$  for the desired proton energy

range.

#### 4.1 Altered Tune

The magnet settings for St. George were determined to transport  $\alpha$  particles from within a 40 mrad angular acceptance cone and with at least a 2 % energy acceptance. The choice of transporting the produced  $\alpha$  particles comes from both being able to verify the acceptance properties of St. George with a direct He beam and from performing the reaction in forward kinematics, leaving the heavy recoil  $^{24}\text{Mg}$  within the  $^{27}\text{Al}$  target. As the produced  $\alpha$  particles have a larger angular emittance than what can be transported by St. George, only those particles emitted within the desired 40 mrad acceptance cone for St. George were tuned to reach the detector focal plane  $F_2$  after the Wien filter and impinge the installed Si strip detector.

The restrictions on the beam spot for measuring  $(\text{p}, \alpha)$  reactions at this focal plane require an approximately symmetric spot size in both directions and one that is smaller than the physical face of the detector, whereas the standard tune for studying  $(\alpha, \gamma)$  reactions required that beam spot to be asymmetric with the beam spot being narrow in the dispersive  $x$ -plane and tall in the  $y$ -plane. The initial COSY code for St. George (see Section 3.1) was altered to model the shortened separator and provide information on the beam characteristics at the new detector focal plane. The magnetic field settings for the seven quadrupoles  $Q_{1-7}$  were adjusted to transport the recoil particles to the detector plane with a final beam spot no larger than the face of the Si detector of  $58 \times 58$  mm. Final pole tip fields are given in Table 4.1. For the  $(\text{p}, \alpha)$  experiment, the  $\alpha$  particles are transported to the Wien filter focal plane while the incident proton beam is rejected before the detector system.

TABLE 4.1

POLE TIP FIELDS FOR  $(\alpha, \gamma)$  AND  $(p, \alpha)$  STUDIES

<b>Quadrupole</b>	<b>Pole Tip Field [T]</b>	
	$(\alpha, \gamma)$	$(p, \alpha)$
1	-0.163 032 76	-0.157
2	0.188 823 63	0.187
3	0.093 841 48	0.094 11
4	-0.126 204 02	-0.04
5	0.100 324 05	0.092
6	0.046 936 54	0.0585
7	0.0	-0.015
8	-0.097 791 79	
9	0.174 396 27	
10	0.210 922 28	
11	-0.139 623 55	

#### 4.1.1 Separator Properties

The resolving power of a separator is defined as the minimum deviation of the rigidity that can be separated from the rigidity that the separator was tuned for. The deviation of the particle with a different rigidity along the dispersive axis is given by

$$x = (x|\Delta)\Delta,$$

where  $(x|\Delta)$  is the matrix element from the transport matrix. A single matrix element  $(a|b)$  can be understood to be the effect on the variable  $a$  at the focal plane given

the value of variable  $b$  at the target location with all the other variable at the target being zero. The resolving power takes into account the distance along the dispersive axis that the differing particles are from the central axis and the width of the image size  $2(x|x)x_0$ . The resolving power can be defined in terms of the particle property that should be separated at the dispersive plane, such as the rigidity or the energy.

The energy resolving power is the minimum energy difference required to resolve a peak from the central image peak assuming that the change in energy is the only difference between the two peaks. By definition this quantity is only a first-order value, so only those parameters with a linear relationship with the position need be considered. The energy resolving power of the separator in relation to the terms present in the COSY transport map is defined as

$$\delta_k(\text{RP}) \equiv \frac{2[(x|x)x_0 + (x|a)a_0]}{(x|\delta_k)}, \quad (4.1)$$

where  $x_0$  and  $a_0$  are the initial half-widths for position (in meters) and angle (in radians), respectively, and the remaining terms are the values from the transport map. The resolving power is only taken in the horizontal plane due to the vertical symmetry of the separator. The terms taken from the transport map are

$$(x|x) = 2.261610$$

$$(x|a) = -0.1368242$$

$$(x|\delta_k) = -0.2774295,$$

where signs are conserved for completeness. The maximal deviation caused by each terms is taken to be a positive value. The half-widths  $x_0$  and  $a_0$  are physically limited by the target chamber and taken to be  $x_0 = 1.5$  mm and  $a_0 = 42$  mrad, giving a resolving power of  $\delta_k(\text{RP}) = 0.286$ . Since the produced  $\alpha$  particles have an

inherent spread in energy due to the incoming beam and the particles themselves interacting with the target, the energy resolution should be viewed as the window within which the energies are indistinguishable. As this window covers the expected energy spread of the produced  $\alpha$  particles, there are no energy corrections required across the detector strips.

Beam currents at the target location were recorded before and after each run. For runs lasting longer than 15 minutes, the current was recorded every 15 minutes. The beam current was seen to fluctuate around the recorded value by up to 100 nA. For runs with multiple current readings, the average was taken as the nominal current. Time on target was recorded by the acquisition system.

#### 4.1.2 Beam Reduction

Incident proton beam intensity reduction on the order of  $10^{10} - 10^{14}$  is necessary in order to avoid damaging the Si detector and to allow for the desired alphas to be detected. This reduction factor becomes more important for those off-resonance runs where the count rate of the produced  $\alpha$  particles is much lower.

Due to the location of the Si detector at the post-Wien filter focal plane  $F_2$ , incident beam reduction can only be achieved through the tuning of the separator. In experiments that use the full length of St. George, beam rejection can be obtained through the use of the mass slits at  $F_2$  to stop the beam after the Wien filter. The location of these slits is the same location as the Si detector, eliminating their use in this experiment. Due to the larger  $\Delta m$  and  $\Delta E$  between the incident proton beam and the produced  $\alpha$  particles, the incident beam is adequately reduced at this point by the dipole magnets and Wien filter.

The Si detector provides the last stage of rejection for the incident beam. Due to the energy difference between the protons and  $\alpha$  particles, the particle peaks will be well separated in the energy spectra. Low energy tails of the  $\alpha$  peak observed

during the energy calibration runs do not have a large effect on the ability to reject the remainder of the incident beam.

## 4.2 Run Procedure

For each experimental run, the aim was to measure the experimental yield at the detector in order to compare it to the theoretical yield for a given angular and energy acceptance. The experimental yield is dependent on the beam current, the run time, and the target properties. For each run, the incident beam must be prepared, and the tuning of St. George must match the expected energy of the produced  $\alpha$  particles. Auxiliary runs are performed to ensure that the beam rejection is within an acceptable range, that the produced particle current is not too high, and that the beam spot on the detector is centered. Once all of the preparations are complete, a run at the desired energy can be performed. All data was collected by the DAQ and stored as binary files for later processing.

The process below describes the steps taken for each individual energy point. For each energy point, multiple runs are performed, with the final run taking place with the final separator settings. The magnetic settings for St. George are based on an altered tune to transport the  $\alpha$  particles to the Wien filter focal plane  $F_2$  such that the beam spot of the produced  $\alpha$  particles is contained within the physical extent of the Si detector. The desired rays through St. George are shown in Fig. 4.1

### 4.2.1 Beam Preparation

The incident proton beam must be tuned for the desired energy. The beam energy is set by adjusting the 5U and the analyzing magnet, with the remainder of the transport beam line adjusted for the new energy. In situations where the previous energy is close (within a few keV) to the desired energy, this energy change is relatively straightforward as it requires smaller changes to the beam line settings.

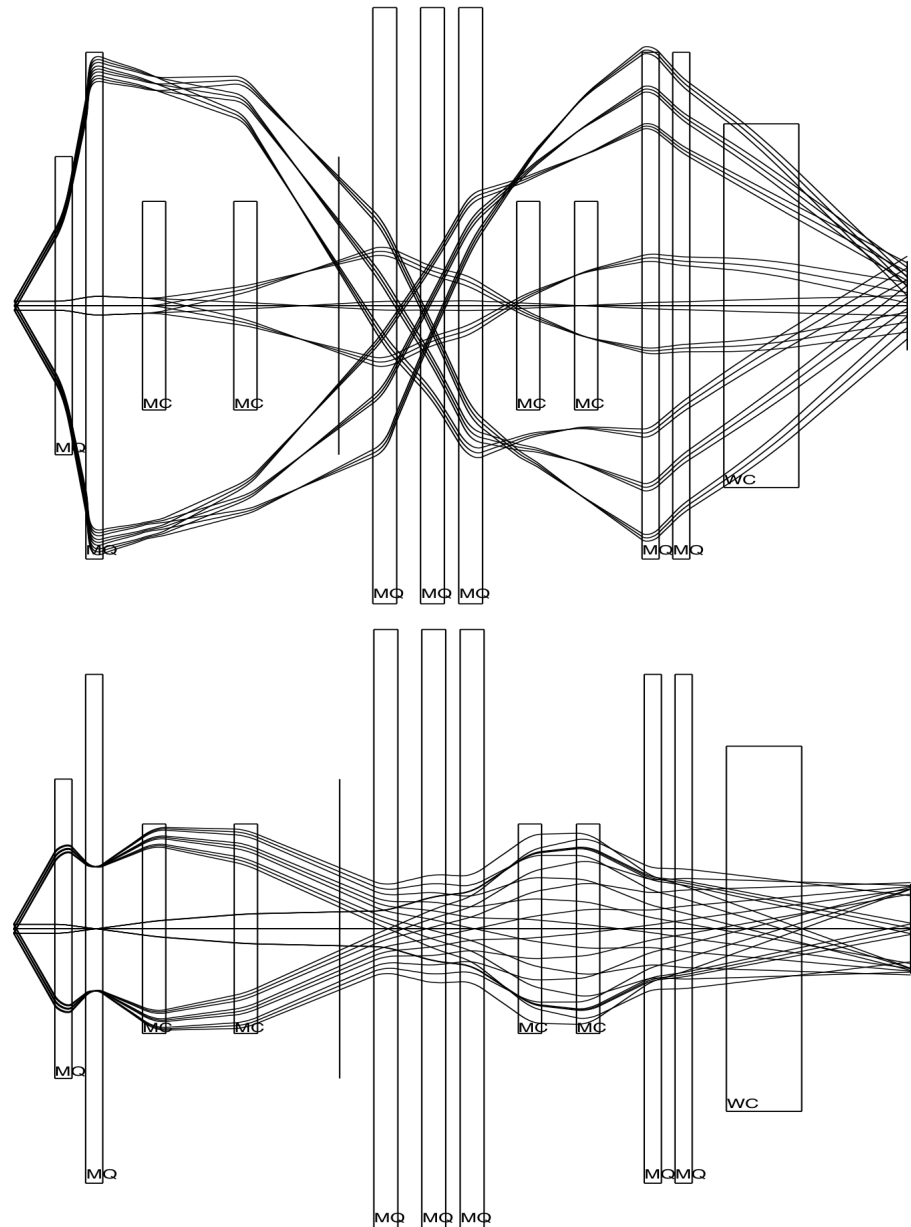


Figure 4.1. Horizontal (upper plot) and vertical (lower plot) rays through St. George for the altered tune transporting  $\alpha$  particles to the post-Wien filter focal plane  $F_2$ . Only the  $\alpha$  particles are shown for simplicity. The pole tip fields are given in Table 4.1.

The incident beam must also be aligned with the magnetic optical axis of St. George in the same manner as described in Sec. 3.3.1. The magnets at the entrance of St. George, namely  $Q_1 Q_2 B_1$  must be brought down to zero in order to align the incident beam. The collimator position is also determined in the same manner as the commissioning work in order to determine the position of the Al target.

Once the beam is aligned, the target is put in place and  $Q_1 Q_2 B_1$  are recycled and brought to their scaled values for the  $\alpha$  particle energy in question. The recycling procedure ensures that the magnetic field produced by the magnet is not affected by self-magnetization.

#### 4.2.2 Measuring Beam Suppression

Once the incident beam is prepared, the next step is to see how much of the beam reaches the detector plane without the target in place. This step is a direct measurement of the suppression of the separator and is essential to ensuring that the count rate at the detector due to the beam is minimal. If the beam current at the detector due to the beam is too high, it is possible that the detector could be damaged or the signal of the produced  $\alpha$  particles could be lost due to dead time considerations.

The detector at the focal plane is located behind a thin Al shield when fully retracted. This shield protects the exposed detector in situations where the direct beam is incident through St. George. To determine if the residual beam current at the detector plane is too high, the detector is slowly moved up while the data acquisition system is running. If the count rate is negligible, the detector is slowly moved up in steps until it reaches its final position centered on the magnetic optical axis.

Using the beam current at the target location, the suppression can be calculated from the yield of the incident proton beam at the detector plane. This suppression does not include the target effects, so it can be considered as an initial estimate of

the rejection of the separator. Initial measurements of the suppression of St. George for the altered tune are approximately  $10^{13}$ . Once the suppression is determined to be adequate for the experiment, the detector is again retracted to behind the shield. The beam at this point is stopped before the target location to allow for the moving of the detector and target.

#### 4.2.3 Target Effects

The initial beam suppression does not include the effects of the target on the incident beam. Once the initial suppression has been shown to be acceptable for the detector, the target is placed into the beam line. Its position is based on the found collimator position from the initial beam tuning and alignment.

Once the target is in place, the detector will see  $\alpha$  particles produced in the reaction and any residual beam protons that are transported to the focal plane. When the beam energy is on resonance, there is a possibility that the produced  $\alpha$  particle count rate is high enough that there could be damage to the detector when combined with the potential residual beam. With the detector still behind the shield, the beam is sent into the target chamber.

As before, the detector is slowly moved up while monitoring the total count rate at the detector. This count rate will primarily be due to the produced  $\alpha$  particles. Once the detector is fully extended, the initial production runs to fine tune the settings of St. George can be completed.

#### 4.2.4 Final Optimization

When scaling the elements of St. George to the expected  $\alpha$  particle energy, both the magnetic elements and the electrostatic plates of the Wien filter need to be

adjusted. The Wien filter voltage is set according to

$$V_{WF} = \frac{dE_\alpha}{2\rho_{WF}},$$

where  $d$  is the distance between the Wien filter plates in meters and  $\rho_{WF}$  is the desired bending radius of the Wien filter. When the  $\alpha$  energy is given in keV, the final voltage will be in kV and is the set point for each of the two electrodes.

The final Wien filter voltage may differ from this value. The central energy of the  $\alpha$  particles may be slightly different than that used, the physical electrodes may have slight imperfections which change the resulting electric field, or the voltage supplied to the electrostatic plates may be slightly different than the set point. For these reasons, the final tuning of the Wien filter is to center the  $\alpha$  particle count distribution horizontally on the Si detector. Adjusting the Wien filter voltage to higher (lower) values for a set magnetic field strength will move the  $\alpha$  distribution right (left) in the horizontal plane. An example showing the horizontal distribution of the  $\alpha$  particles is given in Fig. 4.2.

The  $\alpha$  particle distribution potentially extends past the physical limits of the Si detector in the horizontal and vertical direction. Centering the distribution horizontally may still miss a small proportion of counts. For runs that are near the resonance energy, the counts missed horizontally is a minuscule fraction of the total counts detected and can be effectively ignored. For runs at energies further from the resonance energy, the fraction of counts that are missed by the detector may become a larger fraction of the total counts, requiring further studies to fully quantify the lost counts. The maximum expected lost counts is around 1 % for our runs furthest from the resonance energy. Since the acceptance of St. George is based on counts reaching the detector, these lost counts are based on the tune of the separator and provide an additional metric to measure the capabilities of the separator.

An additional source of lost counts are those from the  $\alpha$  distribution that reach the detector plane above and below the detector. Due to the limitations of the detector system, only those counts below the final detector position can be directly measured. As St. George is vertically symmetric, we assume that the count rate above the detector position is equal to that below the detector system. To measure these counts below the detector position, the detector is moved down to the position where the top of the Si detector is at the same vertical position as the bottom of the detector when it is in its final position. A figure displaying these positions is shown in Fig. 4.3

Once these final checks are performed, the detector is returned to its final position in the center of the beam line. At this point, the actual measurement of the reaction yield can be measured.

#### 4.2.5 Experimental Run

At each energy, the yield of the produced  $\alpha$  particles at the detector is measured until a given threshold is met. For runs at or near the resonance energy, data was collected for 15 minutes. The minimum run time used reduces the possibility that minor fluctuations in the beam current during the run have a significant effect on the final yield. For runs away from the resonance energy, the run was ended once approximately 20k counts were detected within the expected energy range of the produced  $\alpha$  particles summed across all 16 Si strips. This minimum count threshold ensures that the statistical uncertainty is less than 1%.

For the final run, the incident beam current and the detector yield are monitored throughout the run. A beam current measurement is taken before and after the run to provide an estimate on the beam current during the entire run. If the run continues for longer than 15 minutes, the current is also measured every 15 minutes. Due to the design of the target chamber without an offset Si detector, these periodic beam

current measurements are the only way to infer the changing beam current during the run that is independent of the counts at the detector. As the beam is not reacting with the target during these measurements, the time taken is reduced from the total run time.

Once the run is completed, the beam is stopped and the system—the 5U accelerator, the transport beam line, and St. George—are adjusted for the energy for the next run and the process is repeated.

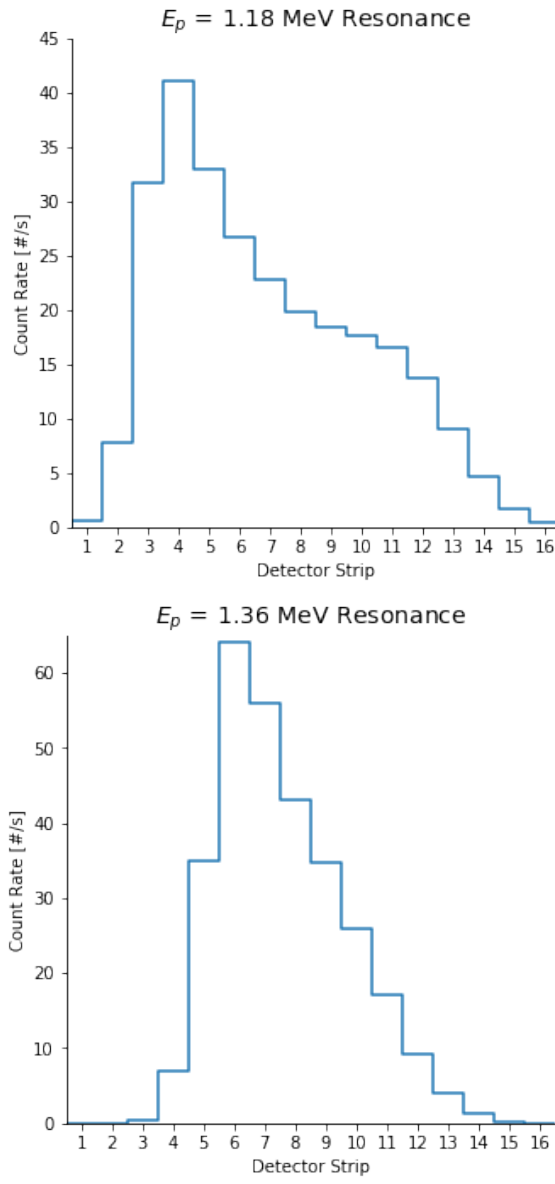


Figure 4.2. Horizontal  $\alpha$  particle distribution at the detector plane after the Wien filter settings are optimized. The optimization centers the count distribution on the detector by adjusting the voltage to swing the beam distribution left or right. The runs near each of the resonance peaks are shown. Strip 1 is on the “beam right” side of the detector. The distributions shown are in the horizontal direction, and are asymmetric due to the horizontal asymmetry of St. George. The count rate at the low position is not shown for simplicity.

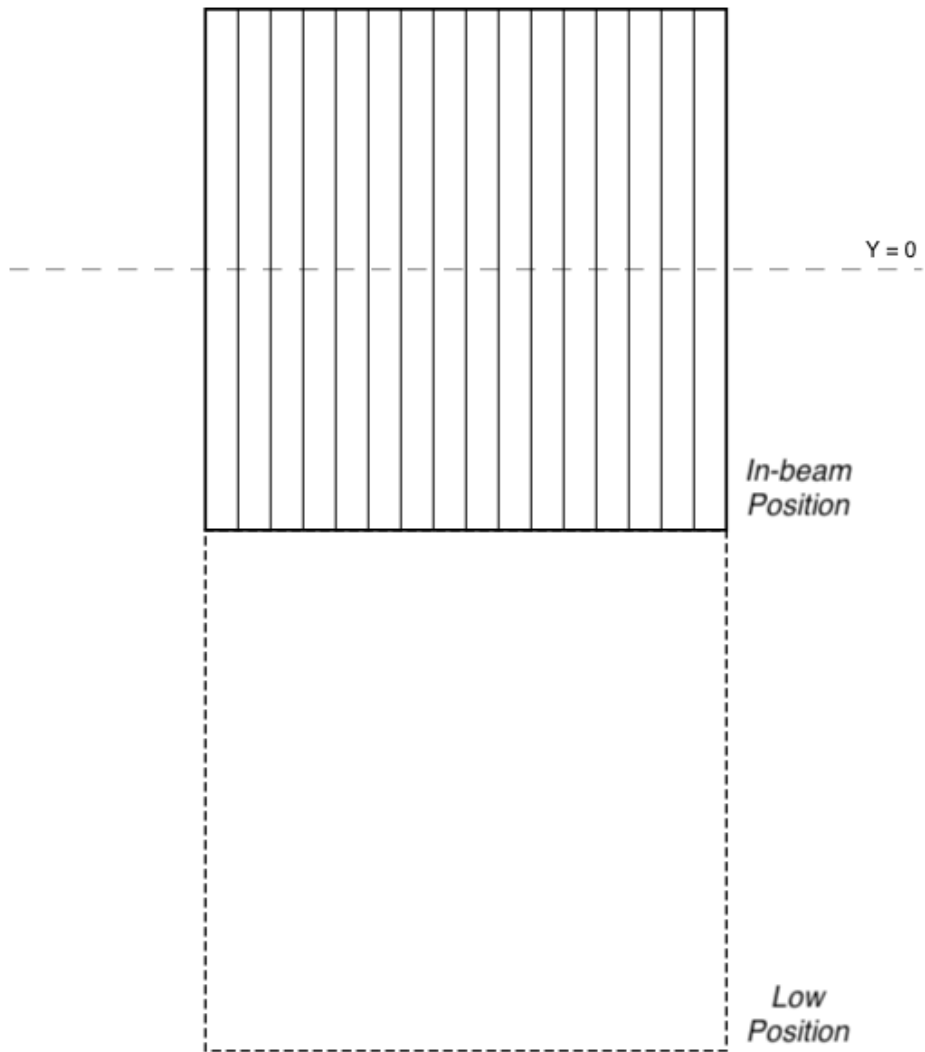


Figure 4.3. Detector positions used to measure the produced  $\alpha$  particles that miss the detector. The horizontal missed particles are determined through adjusting the Wien filter electrostatic field, since the horizontal position of the detector cannot be changed. The individual Si strips are vertical, so the actual vertical extent of the beam cannot be directly determined. The solid detector is the running position, which is centered vertically on the beam line. The dashed position is the low detector position used to estimate the vertical extent of the beam.

## CHAPTER 5

### ANALYSIS

The angular acceptance of St. George can be determined for a given energy by comparing the expected yield based on the known reaction properties to the actual counts measured at the detector plane. Here, we use “energy” as the central energy of the recoil distribution, which is based on the incident beam energy and the measured target properties. The acceptance of St. George is based on the tune of the separator for a given recoil energy, meaning that each run that occurs at a different beam energy, and thus a different tune for St. George, has an associated angular acceptance. The goal is to verify the angular acceptance for particle rigidities within the possible phase space anticipated for the produced recoils of astrophysical interest (see Fig. 3.4). From the experimental data, the properties of the resonance can be determined if the angular and energy acceptances are known, allowing St. George to be used for nuclear astrophysics research.

The experimental work to determine the angular acceptance is one aspect of commissioning the separator and has been one of the most challenging aspects of the work. The  $^{27}\text{Al}(\text{p},\alpha)^{24}\text{Mg}$  reaction runs performed provided an *in situ* test of the angular acceptance by focusing on well-understood resonances within the cross section. The analysis of the experimental results was performed using libraries within the Python scientific stack: NumPy [35], SciPy [24], Matplotlib [21], Pandas [29], and PyMC3 [38]. The routines have been packaged within an analysis framework, `pyne`, to improve the processing and reproducibility of experimental results. See Appendix E for details.

## 5.1 Target Properties

A self-supporting  $^{27}\text{Al}$  target was used for the entirety of the experiment. The target thickness was measured using an offline detector station and a mixed  $^{241}\text{Am}/^{148}\text{Gd}$  alpha-particle source. The target thickness was measured by observing the energy loss of the two alpha peaks and using a Monte Carlo method to determine the value and uncertainty. The measured target thickness is  $63.8_{-1.7}^{+2.0} \mu\text{g/cm}^2$  (95 % confidence interval), which does not include the uncertainty due to SRIM [42], which is used to determine the relationship between energy loss and target thickness for our target material, and can be used to determine the energy loss for other particles at any energy.

In our energy range of interest for both protons and  $\alpha$  particles, the uncertainty in the stopping power in the SRIM results is approximately 3-5 %, based on the spread in experimental values from different data sources [36]. To be conservative, an uncertainty of 5 % is adopted for all calculations. When taking the SRIM uncertainty into account, our measured thickness is  $63.8_{-6.6}^{+6.7} \mu\text{g/cm}^2$  (95 % confidence interval). For subsequent calculations, the thickness used was sampled from this distribution.

The uncertainties present in each step of the procedure laid out above are automatically propagated forward due to the methods chosen. The stochastic nature of the process allows the influence of the base assumptions of the underlying data (e.g. the counts in each bin are drawn from a Poisson distribution) to be seamlessly brought forward without the need of cumbersome mathematics that can potentially hide incorrect assumptions about the values in question, such as that all of the data is normally distributed.

For most of the following calculations, the number of target nuclei per square centimeter is used instead of the thickness in  $\mu\text{g/cm}^2$ . Our target thickness is then  $1.42_{-0.15}^{+0.15} \times 10^{18} \text{nuclei/cm}^2$  (95 % confidence interval), including our SRIM uncertainty. This value is useful for calculating the energy loss of the proton through the target,

as that relies on the number density of the target and the stopping power of the material. The energy loss of the beam will be discussed in the next section.

## 5.2 Beam Properties

The incident proton beam was produced by the 5U and delivered to the St. George target area. The beam energy and resolution were determined through a series of accelerator and beamline commissioning experiments performed before this experiment was performed.

The beam energy was determined from the calibration of the 5U analyzing magnet performed during a different experiment. During the experiment, the magnetic changes were performed slowly such that the magnetic field did not appreciably drift during the runs. The energy resolution can also be determined from the calibration runs, where the resolution is given by the energy width of the leading edge of the resonance scan. Values of approximately 300 eV were commonly observed, with a conservative value of 500 eV adopted for this experiment since no direct energy calibration was performed with our specific experimental setup. The uncertainty in the analyzing magnet field is accounted for within this uncertainty and is not considered separately.

The beam current was relatively stable during the experiment. During the longer runs, the beam current was measured every 15 minutes in order to monitor its change during the run. For each run, the current uncertainty was determined by the measured values for cases where multiple current measurements were performed, or 5 %. For all runs, the final current uncertainty was between 5 and 12 %. Ideally, an offset Si detector at the target location would be used to monitor the beam current during the entirety of the run by measuring the current of the scattered beam particles at a fixed angle. As this setup was not available for the target chamber, periodic direct measurements of the current using the Faraday cup at the target location were

required to measure the beam intensity.

### 5.3 Detector Properties

A 16-strip Si detector was used to detect the produced alpha particles during the experiment. A calibration run was performed following the experiment using the same detector and data acquisition settings as used during the experiment. A  $^{241}\text{Am}/^{148}\text{Gd}$  mixed alpha source was used for calibrating the energy conversion and energy resolution of each strip separately. All of the strips were similar with approximately 2 keV/bin for the calibration and approximately 2.75 % (90 keV) for the energy resolution. The poor energy resolution of the detector resulted from the lower-than-optimal bias voltage setting used during the experiment.

In the calibration runs, only the two highest intensity peaks could be resolved above the background. The alpha peaks also exhibit long low-energy tails such that the particles produced in the  $^{27}\text{Al}(\text{p}, \alpha)^{24}\text{Mg}$  reaction are smeared out in energy. For the experimental run, an energy threshold was set to exclude incident proton counts, where counts appearing above the threshold are considered to be from alpha particles. That threshold was set by the following:

$$E_{\text{proton}} + 3\sigma_{\text{beam}} + 3\sigma_{\text{resolution}} \quad (5.1)$$

The detector efficiency was not directly measured and assumed to be 100 %. Efficiency measurements performed during the commissioning work supporting the St. George detector system resulted in efficiencies above 99 % for all strips.

#### 5.3.1 Simulating the Energy Spectrum

A simulation of the expected energy spectrum at the target location was performed using a combination of SRIM Monte Carlo results and Python. The simulation

looked at the known energy loss within the target of the incident beam, the expected cross section within the energy limits of the target, the energy loss of the produced alpha particles through the remainder of the target, and the energy resolution of the detector to generate an expected energy spectrum. The procedure for this simulation is as follows:

**Step 1:** An energy deviation  $\Delta_{E,p}$  drawn from the  $\text{Normal}(0, \sigma)$  distribution (where  $\sigma$  is the beam energy resolution) for 2000 particles. This energy deviation is the difference in energy from the central energy  $E_{p,0}$ .

**Step 2:** SRIM files for the central energy were generated for fractional depths within the target, where the output is the beam energy profile at that target depth.

**Step 3:** For each simulated particle, a depth within the target is randomly generated based on the underlying reaction cross section covered by the energy range of the incident particles. This depth generation will favor depths that energetically match portions of the cross section with larger values. The underlying cross section was generated using the AZURE2 *R*-matrix code [4, 17].

**Step 4:** For each particle, an energy  $E_d$  is randomly generated from the energy distribution obtained from the SRIM Monte Carlo run to that depth within the target. The final beam energy  $E_{p,f} = E_d + \Delta_{E,0}$  is saved for each particle.

**Step 5:** The beam energy is converted to the produced alpha particle energy through the kinematic equation

$$E_{\alpha,0} = Q + E_p \left( 1 - \frac{m_p}{m_p + m_{^{27}\text{Al}}} \right),$$

where  $Q$  is the  $Q$ -value of the reaction (see Sec. 1.2).

**Step 6:** The difference between the produced alpha energy  $E_{\alpha,0}$  and the alpha energy used to generate the SRIM files is recorded as  $\Delta_{E,\alpha}$ .

**Step 7:** For each particle, an exit energy  $E_{\alpha,f}$  is generated based on the SRIM

Monte Carlo files. The exit energy is drawn from the distribution of exit energies for a target thickness equal to the remainder of the target thickness from the depth generated in Step 5.

**Step 8:** The energy of the alpha particle entering St. George is determined from  $E_\alpha = E_{\alpha,f} + \Delta_{E,\alpha}$ , or adding the energy deviation back to the generated energy.

This procedure generates an  $\alpha$ -particle energy spectrum for the particles entering St. George based on the known properties of the target, cross section, and beam. Using the known energy resolution of the detector, this spectrum can be converted into the detected spectrum

$$E_{\alpha,\text{detector},i} \sim \text{Normal}(E_{\alpha,i}, \sigma_{\text{detector}}),$$

where  $i$  is for each individual particle within the final distribution. An example of the output of this procedure is given in Fig. 5.1

#### 5.4 Additional Parameters

Additional inputs into the final calculation of the acceptance of St. George are the cross section determined from an R-matrix fit on several low-lying resonances, the stopping power of protons in aluminum from SRIM, the run time, and the counts at the detector. For those parameters that are derived from external programs (AZURE2 and SRIM), the uncertainty is assumed to be negligible. The uncertainty in the time was assumed to be 10 seconds for those runs that only lasted for a single 15-minute span, and higher for those runs that required the periodic measurement of the beam current which resulted in stopping the incident beam for an unspecified duration of time.

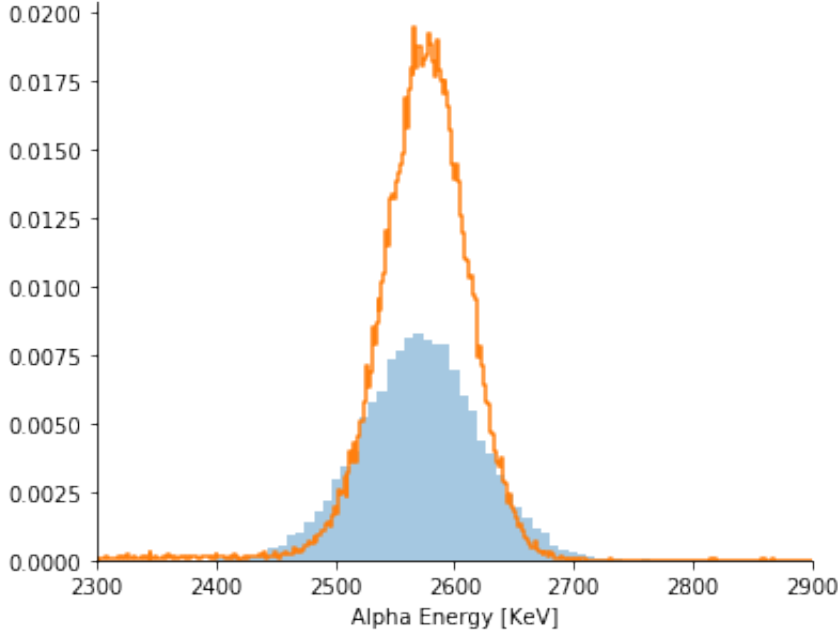


Figure 5.1. Simulated detector  $\alpha$  energy spectrum, following the procedure outlined in Sec. 5.3.1. The blue filled distribution is generated by the procedure, and the orange line is the counts detected at one of the central strips. Each distribution is independently normalized to unit area. There is a qualitative match between the two descriptions, with the simulated spectrum showing fatter tails but a symmetric distribution. The rough re-creation of the distribution from an “uncertainty first” perspective is indicative of the potential future use of the procedure.

The counts at each detector were the sum of all events above the threshold defined by the beam energy and detector resolution. The counts are Poisson distributed, with the length of time for the run was such that the uncertainty from the counts at the detector was not above 5 %, with most runs having a count uncertainty of a much lower value. The direct uncertainty of the counts at the detector is partially convolved with the run time; a lower counting uncertainty requires a longer run time and potentially a larger time uncertainty.

The direct beam reduction by St. George must be on the order of  $10^{10} - 10^{14}$  in order to avoid damaging the Si detector and to measure lower value regions of the

cross section. This requirement is within the designed capabilities of St. George when tuned for heavy recoil transmission to the final detector plane, but must be verified experimentally due to the altered tune and different detector plane required for this experiment. During the experiment, count rates at the detector were monitored, and potential counts from the direct proton beam were excluded from the final counts with the energy discriminator previously described.

## 5.5 Final Acceptance Measurements

The acceptance of St. George can be found for each energy value by comparing the detected counts to the expected yield for that incident beam energy. The yield is found from:

$$Y(E) = \frac{N_r}{N_b}, \quad (5.2)$$

where  $N_r$  is the number of reaction products produced and  $N_b$  is the number of incident beam particles. We can determine  $N_b$  from the beam current and the total run time. The value for  $N_r$  is determined by the total counts at the detector (for the experimental yield) or the integration of target and cross section properties following

$$Y(E_0) = \int_{E_0 - \Delta E_t}^{E_0} \frac{\sigma(E)}{\epsilon(E)} dE, \quad (5.3)$$

where  $E_0$  is the incident beam energy and  $\Delta E_t$  is the target thickness in energy for the incident beam. In both cases, the detector efficiency and St. George transport efficiency are 100 %, as previously discussed.

If we assume that the angular acceptance is symmetric, then we can relate the yield at our detector to the total experimental yield. The area subtended by a symmetric angular acceptance is given by the integral

$$A = \int_0^{2\pi} \int_0^{\theta'} \sin \theta d\theta d\phi = 2\pi (1 - \cos \theta'),$$

where  $\theta'$  is our acceptance angle. This area is a fraction of the total area of the unit sphere. Since our two resonances has an isotropic angular distribution, the areas are proportional to the yield of the cross section. The ratio between the area subtended by our angular acceptance and the total unit sphere area can then be written as the ratio between the yields in each situation, or

$$\begin{aligned}\frac{Y_{\text{experiment}}}{Y_{\text{theory}}} &= \frac{A_{\text{experiment}}}{A_{\text{theory}}} \\ &= \frac{2\pi(1 - \cos\theta')}{4\pi} \\ &= \frac{1}{2}(1 - \cos\theta').\end{aligned}$$

Solving above for our acceptance angle  $\theta'$ , given in mrad, we can relate our experimental yield to the acceptance with

$$\theta' = \arccos\left(1 - 2\frac{Y_{\text{experiment}}}{Y_{\text{theory}}}\right). \quad (5.4)$$

The angular acceptance can be calculated in this way for each run individually. The process for calculating the uncertainty bounds is given by the following, repeated 2000 times to have enough confidence in the final values:

**Step 1:** The beam energy, beam current, and time are sampled from a normal distribution  $\text{Normal}(\mu, \sigma)$ , where  $\mu$  and  $\sigma$  are for the value (energy, current, or time) in question.

**Step 2:** The incident number of particles is calculated from the current and time.

**Step 3:** The target thickness in energy is calculated from finding the stopping power at the incident beam energy from the SRIM tables, and sampling from the distribution of target thicknesses in terms of atoms/cm<sup>2</sup>.

**Step 4:** The yield is determined by integrating Eq. 5.3 between the entrance energy and the lower energy given by that entrance energy minus the target thickness.

**Step 5:** The experimental yield is drawn from a poisson distribution  $\text{Poisson}(c)$ , where  $c$  is the number of counts detected.

**Step 6:** The acceptance for the iteration is calculated by Eq. 5.4.

The distribution of values generated by the process above can be used to find the acceptance and confidence intervals for the run in question. Each run has an acceptance described by its distribution, which is the run for that particular setting of St. George.

## CHAPTER 6

### DISCUSSION

The experiment to measure the  $^{27}\text{Al}(\text{p}, \alpha)^{24}\text{Mg}$  cross section at zero degrees was designed to experimentally confirm the angular acceptance at small energy deviations of St. George. Additionally, the experiment aimed to allow for an additional set of reactions to be studied using St. George to extend its usage beyond  $(\alpha, \gamma)$  reactions of astrophysical interest. The technical capabilities of the separator system were shown to be adequate even with sub-optimal characteristics in the experimental setup, opening up the possibilities of studying low energy  $(\text{p}, \alpha)$  reactions in the future. The angular acceptance at the peak of the resonances was shown to be consistent with the desired design characteristics of the separator.

#### 6.1 Acceptance

The designed angular acceptance of St. George is  $\Delta\theta = 40$  mrad, which is assumed to be cylindrically symmetric around the beam axis. The acceptance was determined for each run independently, based on the properties of the beam, target, and cross section for the  $^{27}\text{Al}(\text{p}, \alpha)^{24}\text{Mg}$  reaction. The acceptances are shown in Fig. 6.1 and tabulated in Table 6.1.

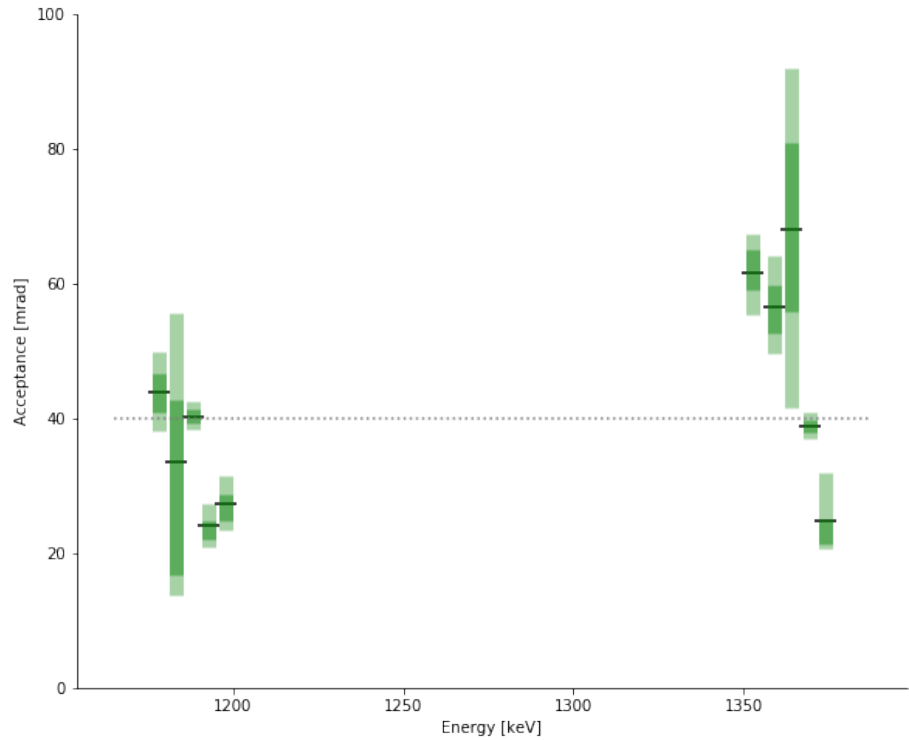


Figure 6.1. Final acceptances for St. George determined by measuring the  $^{27}\text{Al}(\text{p}, \alpha)^{24}\text{Mg}$  yield and comparing to the expected value from the beam, target, and cross section properties. The *maximum a posteriori* acceptance values are shown as the black tick marks. The displayed uncertainty bounds are the 67 % band (dark green) and the 95 % band (light green). The dotted horizontal line is the 40 mrad designed acceptance for St. George.

TABLE 6.1  
ACCEPTANCE WITH UNCERTAINTY

Run Number	$E_p$ [MeV]	Acceptance [mrad]	67 % <sub>L</sub>	67 % <sub>H</sub>	67 % <sub>W</sub>	95 % <sub>L</sub>	95 % <sub>H</sub>	95 % <sub>W</sub>
264	1.374	24.8	-3.5	+0.2	3.7	-4.1	+7.2	11.3
270 <sup>†</sup>	1.369	38.9	-1.0	+0.9	1.9	-1.9	+2.0	3.9
277	1.364	68.1	-12.4	+12.8	25.2	-26.6	+23.9	50.6
282	1.359	56.6	-4.1	+3.2	7.3	-6.9	+7.6	14.5
288	1.353	61.6	-2.6	+3.5	6.1	-6.2	+5.8	12.0
248	1.198	27.3	-2.5	+1.4	3.8	-3.9	+4.2	8.2
255	1.193	24.0	-2.1	+0.7	2.8	-3.0	+3.4	6.4
260 <sup>†</sup>	1.188	40.3	-1.1	+1.0	2.1	-2.0	+2.1	4.1
234	1.183	33.4	-16.7	+9.3	26.0	-19.6	+22.2	41.8
241	1.178	43.8	-2.9	+2.9	5.8	-5.6	+6.1	11.7

<sup>†</sup>: Denotes runs at resonance energy

The acceptance values have different uncertainties based on the specifics of the run, such as the beam energy used and the underlying cross section. The uncertainty around the on-resonance runs are the smallest due to the higher count rate, shorter run times, and the underlying cross section. The cross section for the on-resonance runs peaks near the center of the energy range covered by the target, resulting in a slight shift in beam energy having a smaller effect on the final yield and thus a lower final uncertainty due to the uncertainty in the beam energy (see Fig. 6.2).

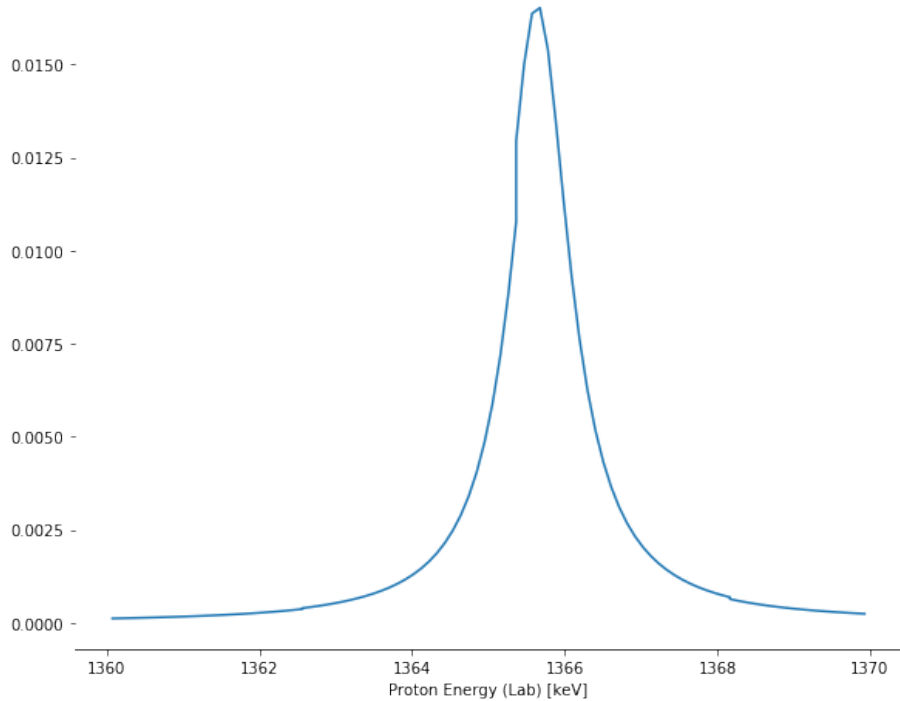


Figure 6.2. Example cross section from the *R*-matrix fit [17] for a run near the resonance energy. Note that the scale is linear. As the cross section peak is near the center of the energy range that the beam has within the target, the final yield is not drastically affected by the uncertainty in the beam energy.

From our analysis, we can also decompose the uncertainty for each run into the contributions from individual uncertainties through our Monte Carlo method. By focusing on the four uncertainties that are primarily under the control of the experimenter—the beam energy uncertainty  $\delta E$ , the run time uncertainty  $\delta t$ , the beam current uncertainty  $\delta i$ , and the target thickness uncertainty  $\delta \Delta$ —the focus of subsequent experiments can be on minimizing the largest uncertainty where necessary. The contributions of the uncertainties are shown in Tables 6.2 and 6.3, where the values are the percentage of the 67 % and the 95 % (respectively) confidence intervals that remains when holding the given variable or variables constant.

Since the final contributions to the uncertainty are not known, and the correlations between different variables not explicitly taken into account, these values should be used as a guide for future improvements instead of relying on the absolute values directly. From the above tables, we can make generalizations about which uncertainties may have the largest impact on further studies. The on-resonance runs are extremely dependent on the beam current uncertainty, as the beam current directly affects what the final yield at the detector will be, and if a smaller uncertainty band is required, controlling the beam current and reducing its uncertainty should be the most important aspect of the experiment. Conversely, the point just below the resonance in energy has an extremely large final uncertainty, mainly due to the beam energy uncertainty. Due to the nature of the cross section, a small shift in beam energy can result in drastically different final yields due to the rapidly changing cross section below the resonance. Subsequent below-resonance runs should focus on reducing the uncertainty from the beam energy, which requires spending more time fine-tuning the accelerator to provide a more energy-stable beam to the experimental area.

TABLE 6.2

ACCEPTANCE BOUNDS WITH HELD VARIABLES, 67%

Held	<b>241</b>	<b>234</b>	<b>260<sup>†</sup></b>	<b>255</b>	<b>248</b>	<b>288</b>	<b>282</b>	<b>277</b>	<b>270<sup>†</sup></b>	<b>264</b>
$E_p$ [MeV]	1.178	1.183	1.188	1.193	1.198	1.353	1.359	1.364	1.369	1.374
$\delta E$	49.0	5.8	96.0	92.1	95.7	64.2	37.8	13.8	106.2	68.8
$\delta t$	101.4	93.5	98.3	103.3	101.8	97.4	101.4	100.2	105.0	99.2
$\delta i$	90.7	96.1	24.7	29.3	61.1	78.1	90.8	101.9	27.0	87.4
$\delta \Delta$	102.1	96.1	99.6	95.9	82.2	99.3	99.9	99.5	105.9	85.6
$\delta E, \delta t$	51.0	5.9	97.8	89.5	92.5	62.9	38.3	13.3	101.3	66.7
$\delta E, \delta i$	12.8	1.3	23.5	20.2	56.1	19.5	12.3	3.2	24.3	57.8
$\delta E, \delta \Delta$	49.0	5.8	97.8	88.9	76.7	59.0	37.5	13.6	101.3	31.1
$\delta t, \delta i$	92.3	99.7	11.4	23.3	63.0	75.9	92.0	100.0	12.5	87.2
$\delta t, \delta \Delta$	101.8	94.7	98.1	98.4	80.3	91.9	98.2	98.6	102.7	83.2
$\delta i, \delta \Delta$	88.9	98.8	25.2	22.4	24.1	76.1	92.6	98.9	26.1	77.1
$\delta E, \delta t, \delta i$	11.2	0.8	7.8	17.4	56.0	18.9	11.4	1.3	5.4	58.2
$\delta E, \delta t, \delta \Delta$	49.8	5.8	95.7	88.4	76.5	58.8	37.7	13.3	98.8	29.0
$\delta E, \delta i, \delta \Delta$	7.8	1.3	21.3	10.1	5.0	8.5	7.1	2.8	22.8	6.6
$\delta t, \delta i, \delta \Delta$	89.4	99.6	10.9	17.9	21.5	78.6	93.4	102.3	10.9	76.2
All	5.6	0.7	3.9	3.6	3.8	6.4	5.0	0.9	3.9	2.0

<sup>†</sup>: Denotes runs at resonance energy

TABLE 6.3

## ACCEPTANCE BOUNDS WITH HELD VARIABLES, 95 %

Held	<b>241</b>	<b>234</b>	<b>260<sup>†</sup></b>	<b>255</b>	<b>248</b>	<b>288</b>	<b>282</b>	<b>277</b>	<b>270<sup>†</sup></b>	<b>264</b>
$E_p$ [MeV]	1.178	1.183	1.188	1.193	1.198	1.353	1.359	1.364	1.369	1.374
$\delta E$	49.4	7.5	101.1	75.8	93.0	64.1	39.6	13.2	102.4	50.9
$\delta t$	101.8	95.3	101.3	99.8	99.6	102.7	101.0	97.9	99.0	107.6
$\delta i$	86.6	97.3	26.8	51.1	66.3	77.7	93.9	93.6	26.5	102.0
$\delta \Delta$	95.4	98.2	101.4	80.4	82.9	98.7	104.2	95.8	103.5	75.8
$\delta E, \delta t$	47.4	7.2	96.7	73.4	93.4	63.8	39.6	13.2	101.4	50.2
$\delta E, \delta i$	12.0	1.7	23.0	18.1	55.5	20.1	12.5	3.0	24.0	42.7
$\delta E, \delta \Delta$	46.8	7.6	100.3	72.0	73.8	60.4	38.0	12.9	103.5	20.6
$\delta t, \delta i$	88.0	97.2	13.4	50.1	64.6	78.2	96.8	96.9	15.2	94.7
$\delta t, \delta \Delta$	98.5	98.3	98.2	86.7	83.5	99.4	102.0	98.8	99.8	75.9
$\delta i, \delta \Delta$	87.7	95.9	26.6	29.7	29.1	76.9	93.4	93.5	25.6	72.9
$\delta E, \delta t, \delta i$	11.1	1.0	8.1	18.6	54.0	17.8	11.5	1.5	8.3	43.5
$\delta E, \delta t, \delta \Delta$	47.4	7.2	96.8	70.1	76.0	59.9	39.0	12.9	99.4	20.4
$\delta E, \delta i, \delta \Delta$	7.9	1.6	21.4	8.4	5.0	8.4	7.4	2.7	22.4	4.6
$\delta t, \delta i, \delta \Delta$	86.2	98.6	13.1	29.6	27.0	78.2	94.2	96.5	14.5	68.0
All	5.4	1.0	4.0	2.8	3.8	6.6	5.2	0.9	3.7	1.3

<sup>†</sup>: Denotes runs at resonance energy

Additionally, the complete uncertainty for our acceptance values cannot be reduced to zero. The irreducible uncertainty present (in the last row of Tables 6.2 and 6.3) for each run is from the uncertainties due to SRIM, the detector statistics, and other sources as described in Section 6.3.

## 6.2 Advantages and Disadvantages

The choice of measuring  $(p, \alpha)$  reactions using a recoil separator such as St. George has a number of advantages and disadvantages over other methods. As the general differences for using recoil separators for reaction studies was discussed in Ch. 1 and will not be repeated here.

The primary advantage of using a recoil separator is that the reaction can be studied at zero degrees. As more common experimental setups have no way to stop the incident high-intensity beam and not the produced particles along zero degrees, any detector placed at zero degrees would either be destroyed due to the high particle rate or the signal completely obscured by the noise from the high proton peak. By using a recoil separator to reject that incident beam, the particles produced at zero degrees can be directly studied in a relatively safe way (in reference to the detector). The tradeoff is that the recoil separator can *only* measure those particles produced at zero degrees, and thus cannot measure the full angular distribution.

Even when using a standard setup to measure the angular distribution, the elastically scattered protons can still be seen at the detectors. There is still a possibility that the count rate from these particles is prohibitive for measuring the produced  $\alpha$  particles. In this case, some energy ranges might be inaccessible for study.

## 6.3 Uncertainties

The final uncertainties on the acceptances at each run energy are skewed distributions. Since basic error propagation relies on the errors being gaussian distributed, the

fact that our uncertainties are not partially justifies the Bayesian approach described previously. Part of the reason for the skewed distributions is that the acceptance is bounded by zero and  $\pi/2$ , and since our distributions sit closer to the zero end instead of near the middle of the range somewhat requires that the distribution be skewed. Our process avoids propagating errors from arbitrary or non-Gaussian distributions and allows for a richer discussion of the contributions of each uncertainty.

### 6.3.1 Statistical

The uncertainties on most of the inputs can be considered to be gaussian distributed, as that represents the statistical nature of the process that creates that input value. Individual collections of these values still exhibit a normal distribution. For values that may be extremely skewed on are known to have other properties, a gaussian distribution may not be the correct underlying uncertainty for the value.

Our final acceptance measurement has a skewed distribution, which can be evidenced from the fact that the angular acceptance cannot be a negative value. In this case, if we were to directly model the final uncertainty of our acceptance, a log-normal distribution would be more apt. For each uncertainty, a brief description of the underlying assumptions will be presented.

#### 6.3.1.1 Target Thickness

No specific underlying distribution was assumed for the target thickness, although a Gaussian distribution could be used for simplicity. The target thickness measurements performed before the experiment were used to determine the particle density within the target. The counts at the detector for the runs were assumed to be Poisson distributed since they are discrete counts. From the peak shifts due to energy loss when the  $\alpha$  particles passed through the target, the number of target nuclei could be determined. The original spectra were used as the base properties to generate

new count distributions, each of which when combined with the energy loss would lead to a unique number of target nuclei. The SRIM tabulated values that were used to relate the energy loss through the target to the target thickness were assumed to have a gaussian distribution, where the standard deviation was taken as 3% of the nominal value. For subsequent uses of the target thickness, a number was drawn from the generated distribution. The model thickness is approximately Gaussian with thickness  $1.42 \pm 0.03 \times 10^{18}$  nuclei/cm<sup>2</sup>.

### 6.3.1.2 Beam Energy

The beam energy was modeled with a Gaussian distribution. The underlying statistical fluctuation of the multiple additive and multiplicative values that determine the beam energy—the power supplies for the ion source, accelerator, and analyzing magnet—result in a gaussian distribution for the beam energy. While the beam energy can never be negative and thus may be better modeled by a log-normal distribution, the values of the beam energy are sufficiently far from zero such that the assumption of a normal distribution can be used. The mean of the distribution is based on the set point for the run, which the standard deviation is constant for all runs. A value of 500 eV was taken as a conservative value from previous energy calibration runs. Since no explicit energy calibration was performed using the exact setup for this experiment, this conservative value represents that additional uncertainty.

### 6.3.1.3 Beam Current

The beam current was modeled with a Gaussian distribution. For similar reasons as the beam energy uncertainty, a gaussian distribution for the beam current was chosen. Observations on the beam current roughly showed a normal distribution around a central value, and the values and fluctuation were such that a log-normal distribution did not need to be assumed. During experimental runs, samples of the

beam current were taken. Without a direct measurement of the beam current during the run, which could be obtained using an offset Faraday cup or Si detector, no more information about the beam current could be obtained. A Cauchy distribution may be considered as an alternative, especially when the accelerator system is producing extremely variable currents, due to the heavier tails of the distribution. For our purposes, conservative estimates of the beam current were obtained from a gaussian distribution based on the current observations performed during the experiment and shown in Table 6.4.

TABLE 6.4  
BEAM CURRENT UNCERTAINTY

Run	$E_p$ [MeV]	$i_p$ [ $\mu\text{A}$ ]	$\delta i_p$ [ $\mu\text{A}$ ]
264	1.374	2.75	0.14
270 <sup>†</sup>	1.369	2.60	0.13
277	1.364	2.70	0.14
282	1.359	2.50	0.13
288	1.353	2.34	0.15
248	1.198	2.18	0.24
255	1.193	1.85	0.19
260 <sup>†</sup>	1.188	2.50	0.13
234	1.183	2.00	0.10
241	1.178	2.47	0.16

<sup>†</sup>: Denotes runs at resonance energy

#### 6.3.1.4 Time

The time was modeled with a Gaussian distribution. Our run times were recorded both as a coarse clock time for the start and end of the run and with the DAQ. For those runs lasting longer than 15 minutes, additional stoppages in the measurement were made in the middle of the run without stopping the DAQ. Values recorded by the DAQ also differed from the set values for the total run time. As each of these factors has a role in the total run time of the experiment and are approximately additive in nature, a gaussian distribution makes sense here. The longer runs had both the stoppage time estimated and subtracted from the total run time, and the uncertainty was also taken to be larger. The uncertainties for the run time are given in Table 6.5.

#### 6.3.1.5 Detector Counts

The total counts at the detector was modeled as a Poisson distribution. As each bin within the Si detector spectra counts the particles that fall within that energy bucket, a Poisson distribution was adopted for the detector counts. This choice is common for counting experiments.

#### 6.3.1.6 SRIM Tabulated Values

The uncertainty of the values obtained from SRIM were taken to be Gaussian distributed. The target stopping power and those values related to finding the target thickness were taken from SRIM. Due to the fact that the  $^{27}\text{Al}(\text{p},\alpha)^{24}\text{Mg}$  reaction is relatively well studied, a conservative estimate of 3% was adopted for all values arising from SRIM results.

TABLE 6.5

## RUN TIME UNCERTAINTY

Run	$E_p$ [MeV]	$t$ [s]	$\delta t$ [s]
264	1.374	910	10
270 <sup>†</sup>	1.369	906	10
277	1.364	989	10
282	1.359	3182	22
288	1.353	9436	53
248	1.198	5455	26
255	1.193	907	10
260 <sup>†</sup>	1.188	907	10
234	1.183	1078	10
241	1.178	6503	51

<sup>†</sup>: Denotes runs at resonance energy

## 6.3.1.7 Final Bands

The final uncertainty bands for each of the acceptance measurements can be analyzed by what values affect the range for the uncertainty. We can limit this discussion to inputs that are controllable by the experimenter. The final uncertainty will be made up of the uncertainty from inputs and the uncertainty from those statistical and irreducible processes. The four inputs that the experimenter can control are the energy, time, current, and thickness uncertainties. The energy uncertainty is related to the stability of the accelerator and the calibration of the analyzing magnet, both of which can be measured and regulated to the point where the uncertainty can be minimized. The time uncertainty is based on the total runtime and the interruptions

caused by requiring the stoppage of the beam in order to measure the current and can be reduced through synchronization of the DAQ with the start of bombardment, and by minimizing interruptions during the data collection process. The current uncertainty can be minimized by measuring the current continuously during the experiment, as there will then be fewer unknown changes in the beam current and a single value for the beam current does not need to be applied to the entirety of the experimental run. Finally, the thickness uncertainty can be minimized by performing target thickness measurements at multiple energies and with potentially multiple particles, and by running those measurements for longer such that the energy loss by the particles can be more accurately determined.

Each of these inputs affects a different part of the final acceptance, based on how it relates to the experimental and theoretical yield, or both. We can determine the impact of reducing the uncertainty on each of these inputs by setting the uncertainty to zero within the analysis pipeline, which would return a different uncertainty band for the run in question. Since these uncertainties are not necessarily independent of each other, we should also look at all combinations of these four inputs being controlled for to get a full picture of the importances. Additionally, the irreducible uncertainty can be determined by keeping all of the inputs constant. The contribution to the final uncertainty is expressed as a percent of the total uncertainty band for both the 67 % and 95 % confidence interval, so the amount of the band that is accounted for by the inputs that are not held constant.

### 6.3.2 Systematic

Potential sources of systematic uncertainty must also be considered when discussing the acceptance results. As low yield future experiments would not have the relatively high count rates at the detector seen during this experiment, the potential for lost counts due to the systematics could drastically affect the final yield and thus

the cross section measurements. Potential sources of systematic uncertainty can be divided into experimental sources and analytical sources.

### 6.3.2.1 Analytical Sources

The analytical sources are much less complex and numerous due to the relatively straightforward analysis required. The assumption of the symmetry of the acceptance cone is discussed in Sec. 6.4 and will not be repeated here.

The energy threshold used to discriminate against the possible protons that reached the detector also discriminates against some of the produced  $\alpha$  particles. Adjusting this threshold opens up the possibility of some proton particles being interpreted as  $\alpha$  particles or reduce the number of detected  $\alpha$  particles. The choice of the value was to ideally eliminate any false positives (protons interpreted as  $\alpha$  particles). As the number of counts below this threshold was small, the effect on the final yield is minimal ( $\ll 1\%$ ).

### 6.3.2.2 Experimental Sources

The experimental sources of systematic uncertainty are those sources that affect the assumptions behind how many  $\alpha$  particles reach the detector. The first assumption is the 100 % transmission of the beam and the simulated recoil particles to the detector plane. The particle transmission was measured before the experiment, for a variety of particle rigidities, between the target Faraday cup and the Wien filter detector cup and shown to be consistent with 100 % transmission. Additionally,  $\alpha$  particles at similar energies to those found in the experiment were shown to reach the actual detector for the full 40 mrad acceptance cone, as shown by the Wien filter quartz viewer. In both of these tests, the possibility for a transmission value that is not 100 %, either due to unforeseen energy losses or a shift or offset in the Faraday cup measurements, opens up the possibility of the detector system not measuring the

full yield produced in the reaction. This produced yield would be the yield within the measurable acceptance cone for St. George. If the tune that was shown to have 100 % transmission for the particles we'd like to detect, but instead the transmission is lower, fewer counts would be seen at the detector and the measured acceptance would be lower.

Within the separator between the target chamber and the detector plane, there is a possibility that the produced  $\alpha$  particles do not reach the detector by interacting with something within the beamline. The particles could strike the interior walls, scattering and losing energy, or one of the removed pieces of diagnostic equipment, or scatter off of the residual vacuum within the beamline. In these cases, the particles produced within the acceptance cone do not reach the detector plane. Those that may reach the detector plane could either be outside of the physical extent of the detector or never reach the detector plane due to these interactions. In all of these cases, the yield measured at the detector will be lower than what was produced within the acceptance cone, leading to a lower acceptance value.

The settings of St. George were determined by previous runs and optimized to transport  $\alpha$  particles from within a 40 mrad cone and with a small energy spread to the active surface of the detector. Since not every possible  $\alpha$  energy could be checked, a single setting for the separator was determined then scaled to the settings that would match the expected  $\alpha$  energy. This choice has the possibility of under- and over-estimating the final acceptance. The systematic shift would be caused by the produced particle being under- or over-focused at different points along the separator, leading to a change in the final position of the particles at the detector plane. While the scaling of the elements in St. George are based on the rigidity of the particles and the fields required, there is still a possibility of a systematic shift in the magnetic field. This shift may come from magnetic hysteresis that was not fully corrected for or an offset or differential scaling in the power supplies for the magnets. This

possibility may especially affect the quadrupole magnets, since they are set only by the current setting for the power supply and not a magnetic field measurement.

## 6.4 Uniformity of Acceptances

When calculating the acceptance for St. George, it was assumed that the acceptance cone was described by a single opening angle. In practice, the horizontal and vertical opening angles may be distinct from each other. During preliminary experiments for the acceptance of St. George, it required much less fine tuning of magnetic fields to achieve the maximum vertical acceptance than it was to achieve the maximum horizontal acceptance. This observation may be due to the lack of dispersive elements in the vertical plane.

The strips of the Si detector were aligned such that an individual strip was oriented in the vertical direction, or a particle that is deflected horizontally would be detected on a different strip (see Fig. 4.3). This orientation allowed for improved tuning in the horizontal plane but with the tradeoff of the lack of sensitivity in the vertical plane. The auxiliary runs performed where the detector was placed in the “low” position (where the top of the detector is located where the bottom of the detector would be in the regular running position) inform the amount of particles that are not captured in the vertical plane due to minor mistuning of the separator, and the auxiliary runs used to center the produced alpha particle distribution on the detector horizontally inform the amount of particles that are not captured in the horizontal direction. Ideally, a detector segmented in both the horizontal and vertical plane would give a full description of the alpha-particle beam spot density at the detector plane and could be used to better relate the distribution of counts at the detector plane to the acceptance cone at the target location.

In the final configuration of the target system, a series of conical collimators will be located following the target location to define the 40 mrad acceptance cone. As

the desired configuration of St. George is to measure  $(\alpha, \gamma)$  reactions where the heavy recoil particles are emitted from the target within a cone with an opening angle less than 40 mrad, the potential effect of a non-symmetric acceptance is reduced. For experiments similar to this where the ejected particles are emitted within a cone larger than 40 mrad, these collimators would ensure that the particles reaching the final detector must have been emitted within that known acceptance cone. This restriction would improve the tuning of the separator for similar experiments, as the emitted particle beam spot at the detector plane can be more easily tuned to fit completely on the detector.

## 6.5 Charge State Distribution

From our reaction, the  ${}^4\text{He}$  can be produced with a charge state of either 1+ or 2+, where the relative amounts of each charge state define the charge state distribution. From the expected distribution, we saw that the 2+ charge state would have a much higher proportion of the produced  ${}^4\text{He}$  from our reaction. Due to the higher production rate, the separator was tuned to transport the  ${}^4\text{He}^{2+}$  from the reaction to the detector plane, rejecting the  ${}^4\text{He}^{1+}$  that is also produced.

The empirical charge state distribution for the interaction between the target material and the produced  $\alpha$  particles can be modeled using a phenomenological model, such as [39]. Under this formulation, our lower resonance energy runs would have 80 % of the particles in the 2+ charge state, and our higher resonance energy runs would have 89 % of the particles in the 2+ charge state. This model assumes an equilibrium for the charge exchange. One limitation of this approach is that the model is based on particles with an energy of  $\sim 1$  MeV/u and above, whereas the alphas produced are at energies of  $\sim 0.75$  MeV/u and below.

A more appropriate approach is to use the *ab initio* code ETACHA to determine the charge state distribution out of equilibrium and at lower energies [26]. Using this

code for our  $^{27}\text{Al}$  target gives a better than 97% proportion of the  $\alpha$  particles within the  $2+$  charge state after  $2 \mu\text{g}/\text{cm}^2$ . For our target thickness of  $63.8_{-1.7}^{+2.0} \mu\text{g}/\text{cm}^2$ , this expected distribution should hold for all but a small proportion of  $\alpha$  particles produced near the exit of the target. For our runs at energies higher than our resonance energy, where a larger proportion of the particles are produced near the exit, this may be a larger uncertainty for those runs, but should still be a negligible fraction for those cross section measurements.

Treating the charge state distribution in the same way as the rest of the inputs should be done to fully capture the entire experimental situation and adds additional complexity to the analysis. Restricting the analysis to only have the  $1+$  and  $2+$  charge states possible does reduce this complexity somewhat.

## 6.6 The $(\text{p}, \alpha_1)$ Channel

At the resonances probed, the  $(\text{p}, \alpha_1)$  reaction channel is also open. Measuring the cross section for this reaction at the two desired resonances is a more difficult experiment due to the lower rigidity of the produced alpha particles due to the lower energy. The kinematics for this reaction are given in Table 6.6.

TABLE 6.6

KINEMATICS FOR  $(\text{p}, \alpha_1)$

Field [G]	$E_{\text{p}}$ [MeV]	$i_{\text{target}}$ [ $\mu\text{A}$ ]	$E_{\alpha}$ [MeV]	$B\rho$ [Tm]	$E\rho$ [MV]
1690.37	1.359	2.6	1.397	0.1702	1.397

The lower rigidity is still within the design parameters of St. George, but due to the altered tune required to direct the produced alpha particles to the detector plane has different rejection properties than the standard tune. As such, the incident proton beam is close enough in rigidity that the beam may strike the detector. The beam reduction levels would not be high enough to avoid damaging the Si detector, preventing the measurement of the cross section without either additional rejection capabilities or an improvement in the tune.

There is still the possibility that, for different energies, the beam rejection properties of St. George would be adequate for measuring particles from excited states of the compound nucleus. An additional possibility is utilizing the remaining third of St. George for its final rejection capabilities. This solution has the added benefit of not requiring an altered tune to transport the produced particles to the detector. With the addition of the post-target collimators, the detected recoils will only come from within 40 mrad, allowing for a more accurate measurement of the yield for the reaction. Since the measured resonances in this experiment are isotropic, it becomes much simpler to extrapolate from the detector yield to the full, angle-integrated yield.

## CHAPTER 7

### CONCLUSIONS

The work supporting the commissioning of the St. George recoil separator can be divided into two distinct sections: direct beam studies and reaction studies. Direct beam studies were used to verify the  $\Delta E/E = 7.5\%$  energy acceptance across a range of electric and magnetic rigidities and provide the first studies of the angular acceptance properties of the separator. The use of multiple beams at different magnetic and electric rigidities allowed the parameter space that St. George is designed to transport to be probed with direct beams, even though those beams are not the exact recoil particles that will be transported during a cross section measurement. The use of reaction studies to support the commissioning work allows for the determination of the angular *and* energy acceptances jointly for the rigidity of the produced particle, replicating the situation when measuring the proposed  $(\alpha, \gamma)$  reactions of astrophysical interest.

The use of the  $^{27}\text{Al}(\text{p}, \alpha)^{24}\text{Mg}$  reaction as this first such case was to verify the  $\Delta\theta = 40$  mrad angular acceptance under experimental conditions and the explore the possibility of using St. George to study additional reactions at zero degrees. The use of the separator under these conditions can support multiple experimental areas within the Nuclear Science Laboratory and opens up the possibility of the separator to be used for a wider range of astrophysically important reactions. These reaction studies may be performed under a similar experimental setup, where the detector system is positioned just beyond the Wien filter, or where the entirety of St. George is used for the incident beam rejection.

## 7.1 Next Steps

As a further test of the angular acceptance capabilities of St. George, the experiment discussed herein can be repeated by sending the produced  $\alpha$  particles to the final detector plane. The transmission of these particles through the entirety of the separator would be able to use the standard ion transport tune for the separator, avoiding the requirement of determining an additional set of magnetic field strengths. A test under these conditions would be a verification of the angular acceptance under similar conditions as will be seen for  $(\alpha, \gamma)$  experiments during the regular operation of the separator. The required work to determine the correct field settings for the final third of St. George was beyond the scope of this work, but will be required for any future study using the detection system at the end of St. George.

In cases where the detection system is placed just beyond the Wien filter at focal plane  $F_2$ , care must be taken to properly ground and shield the cables connecting the detector to the DAQ. This experiment used a suboptimal bias voltage, resulting in additional noise at low energy and a drastic decrease in detector resolution. These facts combined prevented the direct identification of the produced  $\alpha$  particles and the final rejection of the remaining incident protons such that an energy threshold was used to discriminate between the two particles.

For each of the sources of uncertainty, a solution can be implemented to reduce those uncertainties in future experiments. These solutions can be both procedural, where the process to measure a reaction is altered, and physical, where diagnostic equipment could be utilized to provide a better understanding of the underlying assumptions. Some of the uncertainty will be irreducible, but the reducible portion of the uncertainty can be minimized in future experiments.

The first such change is to include an offset Si detector at the target location. This offset detector would be used to monitor the live beam current by measuring the elastically-scattered incident beam and relating that to the incident beam current.

The scattered particles would be detected at a small, fixed angle where the count rate at that detector can be expressed in terms of the incident beam current. The scattered particles can also be used as a measure of the energy of the incident beam beyond what the accelerator is calibrated to deliver. By using this detector, the beam current and energy do not have to be estimated based on periodic measurements or settings of the accelerator, which allows for the contribution of these factors to be more precisely known. The live monitoring will also reduce the timing uncertainty, as interruptions during the data collection process would be eliminated in the best-case scenario, which adjusts the procedure through which a cross section is measured. Finally, a full acceptance check, where the energy and angle are adjusted within the entire range of values, can provide a limit to the systematic uncertainty caused by the potential for an asymmetric angular acceptance.

For follow-up experiments, there are multiple options that can provide an improved outcome for the experiment, based on the limitations and findings presented within. The possibilities of utilizing St. George for experiments past the planned and designed  $(\alpha, \gamma)$  reactions allows for a wider set of potential astrophysical studies to be performed. When combined with a future supersonic jet gas target, the full TOF-vs.- $\Delta E$  detector, and the full separator system, St. George will quickly become a premier facility for nuclear astrophysics.

## 7.2 Closing Thoughts

Fully commissioning a recoil separator requires a vast amount of coordinated resources and time, and is something that would not be possible without a large and motivated team behind it. The attention to detail required for each individual magnet setting and the process through which that magnet is set can only be accomplished through extreme rigor on the experimental side as well as on the logging and information dissemination side. By being explicit about the choices taken and the results,

the progress of the team and the experimental work can be ensured in situations where that problem arises again in the future. Lacking in any of these areas can lead to an increase in the time required to commission a single section of the separator.

Once sections are commissioned, experimental work building off of the sections that are now experimentally accessible and understood should be done to ensure that the understanding of that section is accurate and to provide an avenue for data analysis for the experimenters involved, both to maintain morale and to provide for the possibility of publishing incremental improvements. This experimental work is the outcome of including these experimental “checkpoints” into the grander commissioning work required for St. George, and should be included as the additional components of the St. George system, especially the addition of the gas target, moving forward.

The next reactions that will be probed by St. George are  ${}^3\text{He}(\alpha, \gamma){}^7\text{Be}$ ,  ${}^{14}\text{N}(\alpha, \gamma){}^{18}\text{F}$ ,  ${}^{15}\text{N}(\alpha, \gamma){}^{19}\text{F}$ ,  ${}^{12}\text{C}(\alpha, \gamma){}^{16}\text{O}$ , and  ${}^{18}\text{O}(\alpha, \gamma){}^{22}\text{Ne}$  among others. These reactions require that St. George and its gas target and detector systems be fully commissioned. Due to the necessity of separating out the heavy reaction products from the incident beam, where the two particles have rigidities closer to each other, the final segment of St. George must be utilized. Final particle identification augmented by the full detector system will improve the beam suppression up to and potentially above the  $10^{15}$  level, which will be required for some of the reactions. Each of these additional reactions will be used both for their astrophysical importance as well as testing the properties of St. George. For instance, the reaction  ${}^{18}\text{O}(\alpha, \gamma){}^{22}\text{Ne}$  has an angular and energy spread near the maximums (39.2 mrad and 7.8%, respectively), when measured at  $E_{\text{beam}} = 1.94$  MeV (lab energy). Additional reactions that test the limits of the separator are outlined in [15].

The work described sets the initial footing for these following tests. The cumulative usage and understanding of the separator iteratively improves the operation of the system for all subsequent runs. Eventually, the improved magnetic field settings

will minimize the long tuning process, allowing for future experiments to spend less time tuning between runs and more time measuring the low count rate, off-resonance regions of the cross section. These regions can be extremely informative for the  $R$ -matrix formulation of the cross section, and using St. George provides the unique ability to probe these regions.

The design of St. George has also been adopted for SECAR (SEparator for CApture Reactions), a new recoil mass separator being installed at the Facility for Rare Isotope Beams (FRIB) at Michigan State University [7]. SECAR is designed to measure  $(p, \gamma)$  and  $(\alpha, \gamma)$  reactions in inverse kinematics. Of particular interest are the design of the Wien filters, the use of similar beam optics codes during the design process, and the utilization of a recirculating gas target to provide a pure target. The continuing commissioning of St. George will have the added benefit of improving procedures at SECAR, including the use of the camera systems developed to help tune the test beams. Both systems will benefit from the continued collaboration between the two teams.

As commissioning a recoil separator relies on more than just the separator itself, the work requires a flexible and multi-faceted approach to readying the system for experimental work. The results presented within on the initial commissioning work and the use of St. George for additional reaction studies is promising for the future of the facility.

## APPENDIX A

### RUN INFORMATION

Additional information about the  $^{27}\text{Al}(\text{p}, \alpha)^{24}\text{Mg}$  production runs.

TABLE A.1  
RUN ENERGY DETAILS

Run Numbers	Field [G]	$E_p$ [MeV]	$E_\alpha$ [MeV]	Suppression
261—264	1693.3	1.363 18	2.7700	$4.9 \times 10^{12}$
265—270 <sup>†</sup>	1690.4	1.358 52	2.7655	$1.5 \times 10^{12}$
271—277	1687.1	1.353 22	2.7604	$5.5 \times 10^{12}$
278—282	1683.9	1.348 09	2.7554	$5.8 \times 10^{13}$
283—288	1680.1	1.342 01	2.7495	$1.2 \times 10^{14}$
242—248	1580.8	1.188 07	2.5996	$9.5 \times 10^{12}$
251—255	1577.5	1.183 11	2.5948	$3.4 \times 10^{12}$
256—260 <sup>†</sup>	1574.6	1.178 76	2.5905	$1.4 \times 10^{12}$
229—234	1571.4	1.173 98	2.5859	$5.8 \times 10^{12}$
235—241	1567.9	1.168 75	2.5808	$1.1 \times 10^{13}$

<sup>†</sup>: Denotes runs at resonance energy

## APPENDIX B

### ALPHA CALIBRATION ENERGIES

A mixed  $^{241}\text{Am}/^{148}\text{Gd}$  alpha-particle source was used to calibrate the Si strip detector and determine the  $^{27}\text{Al}$  target thickness. For the produced alphas during the experiment, they are closer in energy to those from the decay of  $^{148}\text{Gd}$ .

TABLE B.1  
 ALPHA PARTICLE ENERGIES FOR THE  $^{241}\text{Am}/^{148}\text{Gd}$  MIXED  
 SOURCE

<b>Isotope</b>	<b>Energy [keV]</b>	<b>Relative Intensity [%]</b>
$^{148}\text{Gd}$	3182.69	100
$^{241}\text{Am}$	5388	1.6
	5442.8	13.1
	5485.56	84.8

## APPENDIX C

### DEFLECTOR SETTINGS

Deflector settings used for commissioning work. Voltages are based on the physical characteristics of the deflector system and the beam properties to provide the necessary deflection. Set points are based on the version of the control program in place at the time of the experiments.

TABLE C.1  
 DEFLECTOR SETTINGS FOR TEST BEAMS

	$^1\text{H}^+$ at 1 MeV		$^4\text{He}^+$ at 2.3 MeV	
Angle [mrad]	Voltage [kV]	Set point	Voltage [kV]	Set point
5	0.363	9	0.834	24
10	0.725	20	1.668	49
15	1.087	31	2.501	74
20	1.450	42	3.335	100
25	1.813	53	4.170	125
30	2.176	64	5.004	150
35	2.539	75	5.839	175
40	2.902	86	6.674	201
45	3.265	97	7.509	226

## APPENDIX D

### FRINGE FIELD PARAMETERS

Values used for the fringe field parameters for magnetic elements within COSY. The default values used are presented alongside the refit parameters for  $Q_{10}$  as an example. The refitting procedure based on the provided field maps was essential to making the COSY code as similar as possible to the physical separator to aide in tuning.

TABLE D.1

ENGE COEFFICIENTS FOR  $Q_{10}$  COMPARED TO COSY DEFAULTS

Coefficient	$Q_{10}$ Values	COSY Defaults
$k_0$	0.997 314 89	
$a_0$	0.372 552 61	0.296 471
$a_1$	6.186 997 78	4.533 219
$a_2$	-5.555 141 15	-2.270 982
$a_3$	6.962 108 51	1.068 627
$a_4$	-4.825 813 28	-0.036 391
$a_5$	1.313 578 7	0.022 261

## APPENDIX E

### ANALYSIS PACKAGE

The analysis and plots contained within this dissertation were completed using Python and a small set of standard scientific python packages:

**Matplotlib** a 2D plotting package that supports multiple backends and output formats

**NumPy** a standard numeric package for array (vector and matrix) computing

**Pandas** a tabular data interface that organizes heterogeneous data into simple to use and manipulate data structures

**PyMC3** a probabilistic programming language in python useful for Bayesian inference

**SciPy** a scientific utilities package built on top of NumPy that includes general-purpose routines such as curve fitting, root finding, signal processing and more

These packages are standard components of the Python Scientific Stack, and their usage and internals are well-documented and trusted by many scientists in multiple fields. The usage of Python in the scientific community has increased steadily over the years, with multiple special purpose packages built on top of the foundation of these three packages, particularly NumPy.

For the actual analysis, a two-part analysis framework was developed in tandem with the analysis work: Python for Nuclear Experiments (PyNE) and the St. George

Analysis Package (SAP). These packages are designed to be extensible by other research groups, guided by the requirements of the St. George group, while providing an easy-to-use and understand object-oriented interface to performing nuclear astrophysics research. Development work was chronicled on the packages' GitHub page<sup>1</sup>, and may be installed from there.

These packages would not be possible without two other important packages: the ROOT<sup>2</sup> Data Analysis Framework[9] and `evt2root`<sup>3</sup>.

## E.1 Python for Nuclear Experiments

The PyNE package provides base functionality for interacting with experimental data generated through the standard data acquisition systems in use at the Nuclear Science Laboratory at the University of Notre Dame. The package was designed to provide a base pythonic interface to the data files, including converting them into data files that work easily with standard python scientific packages. The underlying purpose for PyNE is not to be an end-to-end analysis package, but provide the necessary structure to such an end-to-end analysis package with a common and simple API.

The primary functionality is the organizing of experimental data. From binary files in either (currently) `.Chn` or `.evt` format, the data is converted into `numpy.ndarray` format. A logical directory structure is set up, with run metadata extracted from the binary files stored in a local JSON file.

Within the API, the data can be easily queried and worked with. The provided `pyne.Data` objects (subclassed for channel and event data) implement the iterator

---

<sup>1</sup><https://github.com/mmoran0032/pyne>

<sup>2</sup><http://root.cern.ch/>

<sup>3</sup><https://github.com/ksmith0/evt2root>

protocol over the ADCs. In this way, concise and clear analysis on the entire 16-strip detector can be accomplished through code as simple as the following:

---

```
import pyne
from local_analysis import determine_counts

data_obj = pyne.EVTData('data/run0808')
data_obj.load_data()

total_counts = sum(
    determine_counts(d) for d in data_obj.adc
)
```

---

By creating objects that encapsulate the data and meta-data, the end-to-end analysis becomes much easier, as details about a run and exploratory work are vastly simplified.

## E.2 St. George Analysis Package

For most analysis, there is a need for more work than just finding the total number of counts. For the experiment conducted within this dissertation, a few routines were standardized within an add-on package to PyNE called SAP. Since PyNE just provides the primitive classes for analysis, any number of extension packages may be produced building upon that core functionality.

## E.3 Justification

Python has become a leading programming language across a range of uses and industry, led primarily by its data analysis, data science, and machine learning ap-

plications<sup>4</sup>. The three main data analysis packages for python—numpy, pandas, and matplotlib—have become essential tools in a variety of cases, especially within the sciences. Packages built upon this base, such as SunPy<sup>5</sup> (Python for Solar Physics), AstroPy<sup>6</sup>, Biopython<sup>7</sup>, and many others have been written, tested, and used by researchers all around the globe. Ground-breaking scientific discoveries, such as the detection of gravitational waves by LIGO, have been made using Python as one of the primary analysis languages<sup>8</sup>. Python has become a *de facto* language for data analysis in many circles (outside of statistics where R<sup>9</sup> is still the primary language), an adopting it for nuclear astrophysics should not be far behind.

There is a current package `becquerel`<sup>10</sup> that has been under development since October 2016 by users at LBNL. As this package was not known about at the start of my analysis, it was not used, but it could be possible to use it as a replacement for SAP with a transformation layer between PyNE and the routines within Becquerel. There are some very interesting examples of using Becquerel for nuclear physics analysis that can be viewed in the examples folder in the GitHub repo. If I were completing this analysis now, I would have stopped at the data translation layer in PyNE and moved into writing routines that use Becquerel for the heavy analysis work.

For those thinking that the “slow” speed of python will hold them back from performing large-scale analysis, or that python might not fit with the use cases that

---

<sup>4</sup>Why is Python Growing So Quickly? <https://stackoverflow.blog/2017/09/14/python-growing-quickly/>

<sup>5</sup><https://github.com/sunpy/sunpy>

<sup>6</sup><https://github.com/astropy/astropy>

<sup>7</sup><https://github.com/biopython/biopython>

<sup>8</sup>[https://losc.ligo.org/s/events/GW150914/GW150914\\_tutorial.html](https://losc.ligo.org/s/events/GW150914/GW150914_tutorial.html)

<sup>9</sup><https://www.r-project.org/>

<sup>10</sup><https://github.com/lbl-anp/becquerel>

the researcher has, I implore you to watch Jake VanderPlas’s keynote<sup>11</sup> from PyCon 2017. One additional point is that the speed of execution is most likely not the limiting factor in the analysis, but the speed of the researcher to write, debug, and understand the code may very well be that bottleneck. Additionally, the use of Jupyter Notebooks<sup>12</sup> for code alongside documentation allows for a lower barrier to entry for rerunning and understanding experimental analyses years later.

As a user of python since 2007, I have seen large changes in the python ecosystem and have gradually included python more and more into my own work. Right now, I owe my career to python and the open source data analysis packages, and I don’t expect that fact to change any time soon. While my work has shifted from curve fitting to gradient boosted trees and neural networks, it is still in python, and in many cases the final understanding of my complex models comes down to dot products in `numpy` and plotting with `matplotlib`.

This dissertation would not have been possible without the countless hours of work and thousands of open source contributions to these core data analysis libraries and python itself.

---

<sup>11</sup><https://www.youtube.com/watch?v=ZyjCqQEUA8o>

<sup>12</sup><https://jupyter.org/>

## BIBLIOGRAPHY

1. M. Aliotta, M. Junker, P. Prati, O. Straniero, and F. Strieder. *The European Physical Journal A*, 52(4):76, Apr 2016. ISSN 1434-601X. doi: 10.1140/epja/i2016-16076-3. URL <https://doi.org/10.1140/epja/i2016-16076-3>.
2. S. Andersen, A. Haug, T. Holtebekk, O. Loensjoe, and R. Nordhagen. *Phys. Norvegica*, 1(1), 1961.
3. C. Angulo, M. Couder, S. Cherubini, W. Galster, J.-S. Graulich, P. Leleux, F. Vanderbist, and A. Shotter. *Nuclear Physics A*, 688(1):462 – 464, 2001. ISSN 0375-9474. doi: [http://dx.doi.org/10.1016/S0375-9474\(01\)00756-4](http://dx.doi.org/10.1016/S0375-9474(01)00756-4). URL <http://www.sciencedirect.com/science/article/pii/S0375947401007564>. Nuclei in the Cosmos.
4. R. E. Azuma, E. Uberseder, E. C. Simpson, C. R. Brune, H. Costantini, R. J. de Boer, J. Görres, M. Heil, P. J. LeBlanc, C. Ugalde, and M. Wiescher. *Phys. Rev. C*, 81:045805, Apr 2010. doi: 10.1103/PhysRevC.81.045805. URL <https://link.aps.org/doi/10.1103/PhysRevC.81.045805>.
5. R. Baartman and D. Kaltchev. *Proceedings of PAC2007*, pages 3229 – 3231, 2007. doi: 10.1109/PAC.2007.4440381.
6. D. W. Bardayan, K. A. Chipps, R. P. Fitzgerald, J. C. Blackmon, K. Y. Chae, A. E. Champagne, U. Greife, R. Hatarik, R. L. Kozub, C. Matei, B. H. Moazen, C. D. Nesaraja, S. D. Pain, W. A. Peters, S. T. Pittman, J. F. Shriner, and M. S. Smith. *The European Physical Journal A*, 42(3):457, 2009. ISSN 1434-601X. doi: 10.1140/epja/i2008-10737-8. URL <https://doi.org/10.1140/epja/i2008-10737-8>.
7. G. Berg, M. Couder, M. Moran, K. Smith, M. Wiescher, H. Schatz, U. Hager, C. Wrede, F. Montes, G. Perdikakis, X. Wu, A. Zeller, M. Smith, D. Bardayan, K. Chipps, S. Pain, J. Blackmon, U. Greife, K. Rehm, and R. Janssens. *Nuclear Instruments and Methods in Physics Research Section A: Accelerators, Spectrometers, Detectors and Associated Equipment*, 877:87 – 103, 2018. ISSN 0168-9002. doi: <https://doi.org/10.1016/j.nima.2017.08.048>. URL <http://www.sciencedirect.com/science/article/pii/S0168900217309488>.
8. A. Boeltzig, C. G. Bruno, F. Cavanna, S. Cristallo, T. Davinson, R. Depalo, R. J. deBoer, A. Di Leva, F. Ferraro, G. Imbriani, P. Marigo, F. Terrasi, and

- M. Wiescher. *The European Physical Journal A*, 52(4):75, Apr 2016. ISSN 1434-601X. doi: 10.1140/epja/i2016-16075-4. URL <https://doi.org/10.1140/epja/i2016-16075-4>.
9. R. Brun and F. Rademakers. Root - an object oriented data analysis framework, 1997. URL <http://root.cern.ch/>.
  10. E. M. Burbidge, G. R. Burbidge, W. A. Fowler, and F. Hoyle. *Rev. Mod. Phys.*, 29:547–650, Oct 1957. doi: 10.1103/RevModPhys.29.547. URL <https://link.aps.org/doi/10.1103/RevModPhys.29.547>.
  11. A. G. W. Cameron. *Publications of the Astronomical Society of the Pacific*, 69(408):201, 1957. URL <http://stacks.iop.org/1538-3873/69/i=408/a=201>.
  12. B. W. Carroll and D. A. Ostlie. *An Introduction to Modern Astrophysics*. Addison-Wesley, San Francisco: Pearson, 2nd (international) edition, 2007.
  13. K. A. Chipps, D. W. Bardayan, J. C. Blackmon, K. Y. Chae, U. Greife, R. Hatarik, R. L. Kozub, C. Matei, B. H. Moazen, C. D. Nesaraja, S. D. Pain, W. A. Peters, S. T. Pittman, J. F. Shriner, and M. S. Smith. *Phys. Rev. Lett.*, 102:152502, Apr 2009. doi: 10.1103/PhysRevLett.102.152502. URL <https://link.aps.org/doi/10.1103/PhysRevLett.102.152502>.
  14. M. Couder, C. Angulo, W. Galster, J.-S. Graulich, P. Leleux, P. Lipnik, G. Tabacaru, and F. Vanderbist. *Nuclear Instruments and Methods in Physics Research Section A: Accelerators, Spectrometers, Detectors and Associated Equipment*, 506(1):26 – 34, 2003. ISSN 0168-9002. doi: [https://doi.org/10.1016/S0168-9002\(03\)01381-0](https://doi.org/10.1016/S0168-9002(03)01381-0). URL <http://www.sciencedirect.com/science/article/pii/S0168900203013810>.
  15. M. Couder, G. P. A. Berg, J. Görres, P. J. LeBlanc, L. O. Lamm, E. Stech, M. Wiescher, and J. Hinnefeld. *Nuclear Instruments and Methods in Physics Research, Section A: Accelerators, Spectrometers, Detectors and Associated Equipment*, 587:35–45, Mar. 2008. doi: 10.1016/j.nima.2007.11.069.
  16. C. N. Davids. *Nuclear Instruments and Methods in Physics Research Section B: Beam Interactions with Materials and Atoms*, 204:124–128, 2003.
  17. R. J. deBoer. Private communication, 2017.
  18. R. J. deBoer, D. W. Bardayan, J. Görres, P. J. LeBlanc, K. V. Manukyan, M. T. Moran, K. Smith, W. Tan, E. Uberseder, M. Wiescher, P. F. Bertone, A. E. Champagne, and M. S. Islam. *Phys. Rev. C*, 91:045804, Apr 2015. doi: 10.1103/PhysRevC.91.045804. URL <https://link.aps.org/doi/10.1103/PhysRevC.91.045804>.
  19. S. Engel, D. Hutcheon, S. Bishop, L. Buchmann, J. Caggiano, M. Chatterjee, A. Chen, J. DAuria, D. Gigliotti, U. Greife, et al. *Nuclear Instruments and*

*Methods in Physics Research Section A: Accelerators, Spectrometers, Detectors and Associated Equipment*, 553(3):491–500, 2005.

20. G. Gilardy. Private communication, 2017.
21. J. D. Hunter. *Computing in Science & Engineering*, 9(3):90–95, 2007. doi: 10.1109/MCSE.2007.55. URL <https://aip.scitation.org/doi/abs/10.1109/MCSE.2007.55>.
22. C. Iliadis. *Nuclear Physics of Stars*. Wiley-VCH, 1 2008. ISBN 9783527406029. doi: 10.1002/9783527618750.
23. A. James, T. Morrison, K. Ying, K. Connell, H. Price, and J. Simpson. *Nuclear Instruments and Methods in Physics Research Section A: Accelerators, Spectrometers, Detectors and Associated Equipment*, 267(1):144 – 152, 1988. ISSN 0168-9002. doi: [https://doi.org/10.1016/0168-9002\(88\)90638-9](https://doi.org/10.1016/0168-9002(88)90638-9). URL <http://www.sciencedirect.com/science/article/pii/0168900288906389>.
24. E. Jones, T. Oliphant, P. Peterson, et al. SciPy: Open source scientific tools for Python, 2001–. URL <http://www.scipy.org/>. [Online; accessed 2017-03-29].
25. A. Kontos, D. Schrmann, C. Akers, M. Couder, J. Grres, D. Robertson, E. Stech, R. Talwar, and M. Wiescher. *Nuclear Instruments and Methods in Physics Research Section A: Accelerators, Spectrometers, Detectors and Associated Equipment*, 664(1):272 – 281, 2012. doi: <https://doi.org/10.1016/j.nima.2011.10.039>.
26. E. Lamour, P. D. Fainstein, M. Galassi, C. Prigent, C. A. Ramirez, R. D. Rivarola, J.-P. Rozet, M. Trassinielli, and D. Vernhet. *Phys. Rev. A*, 92:042703, Oct 2015. doi: 10.1103/PhysRevA.92.042703. URL <https://link.aps.org/doi/10.1103/PhysRevA.92.042703>.
27. A. D. Leva, M. D. Cesare, D. Schrmann, N. D. Cesare, A. DOnofrio, L. Giolanella, R. Kunz, G. Imbriani, A. Ordine, V. Roca, D. Rogalla, C. Rolfs, M. Romano, E. Somorjai, F. Strieder, and F. Terrasi. *Nuclear Instruments and Methods in Physics Research Section A: Accelerators, Spectrometers, Detectors and Associated Equipment*, 595(2):381 – 390, 2008. ISSN 0168-9002. doi: <https://doi.org/10.1016/j.nima.2008.07.082>. URL <http://www.sciencedirect.com/science/article/pii/S0168900208009236>.
28. K. Makino and M. Berz. *Nuclear Instruments and Methods in Physics Research, Section A: Accelerators, Spectrometers, Detectors and Associated Equipment*, 558(1):346–350, 3 2006. ISSN 0168-9002. doi: 10.1016/j.nima.2005.11.109.
29. W. McKinney. Data structures for statistical computing in python. In S. van der Walt and J. Millman, editors, *Proceedings of the 9th Python in Science Conference*, pages 51–56, 2010.

30. Z. Meisel, K. Shi, A. Jemcov, and M. Couder. *Nuclear Instruments and Methods in Physics Research, Section A: Accelerators, Spectrometers, Detectors and Associated Equipment*, 828:8–14, 2016. doi: 10.1016/j.nima.2016.04.115.
31. Z. Meisel, M. T. Moran, G. Gilardy, J. Schmitt, C. Seymour, and M. Couder. *Nuclear Instruments and Methods in Physics Research Section A: Accelerators, Spectrometers, Detectors and Associated Equipment*, 850:48 – 53, 2017. doi: <http://dx.doi.org/10.1016/j.nima.2017.01.035>.
32. L. Morales, S. Kalkal, H. S. Jung, C. Seymour, G. Gilardy, M. Moran, Z. Meisel, J. Hinnefeld, and M. Couder. Performance of the st. george detector system. In *APS Division of Nuclear Physics Meeting Abstracts*, 2016. URL <http://meetings.aps.org/link/BAPS.2016.DNP.PC.7>.
33. J. A. Nelder and R. Mead. *The Computer Journal*, 7(4):308–313, 1965.
34. R. O. Nelson, E. G. Bilpuch, C. R. Westerfeldt, and G. E. Michell. *Phys. Rev.*, C30:755–764, 1984. doi: 10.1103/PhysRevC.30.755.
35. T. E. Oliphant. *A guide to NumPy*, volume 1. Trelgol Publishing USA, 2006.
36. H. Paul and A. Schinner. *Nuclear Instruments and Methods in Physics Research Section B: Beam Interactions with Materials and Atoms*, 179(3):299 – 315, 2001. ISSN 0168-583X. doi: [https://doi.org/10.1016/S0168-583X\(01\)00576-6](https://doi.org/10.1016/S0168-583X(01)00576-6). URL <http://www.sciencedirect.com/science/article/pii/S0168583X01005766>.
37. D. Rogalla, D. Schrann, F. Strieder, M. Aliotta, N. DeCesare, A. DiLleva, C. Lubritto, A. DOnofrio, L. Gialanella, G. Imbriani, J. Kluge, A. Ordine, V. Roca, H. Rcken, C. Rolfs, M. Romano, F. Schmann, F. Terrasi, and H. Trautvetter. *Nuclear Instruments and Methods in Physics Research Section A: Accelerators, Spectrometers, Detectors and Associated Equipment*, 513(3):573–578, 2003.
38. J. Salvatier, T. V. Wiecki, and C. Fonnesbeck. *PeerJ Computer Science*, 2:e55, Apr. 2016. ISSN 2376-5992. doi: 10.7717/peerj-cs.55. URL <https://doi.org/10.7717/peerj-cs.55>.
39. R. Sayer. *Revue de Physique Appliquée*, 12(10):1543–1546, 1977. doi: 10.1051/rphysap:0197700120100154300. URL <https://hal.archives-ouvertes.fr/jpa-00244364>.
40. M. Shamsuzzoha Basunia. *Nuclear Data Sheets*, 114(1189), 2013. Data extracted from the ENSDF database, version October 2013, [13NDS].
41. M. Smith, C. Rolfs, and C. Barnes. *Nuclear Instruments and Methods in Physics Research Section A: Accelerators, Spectrometers, Detectors and Associated Equipment*, 306(1-2):233–239, 1991.

42. J. F. Ziegler, J. P. Biersack, and M. D. Ziegler. Srim-2008.04, 2008. URL <http://www.srim.org/>.

This document was prepared & typeset with pdfL<sup>A</sup>T<sub>E</sub>X, and formatted with NDdiss2<sub>ε</sub> classfile (v3.2013[2013/04/16]) provided by Sameer Vijay and updated by Megan Patnott.